

**PROCESS DEVELOPMENT AND CHARACTERIZATION OF
PIEZOELECTRIC TRANSDUCERS ON FLEXIBLE SUBSTRATES FOR
HIGH FREQUENCY ULTRASOUND APPLICATIONS**

A Thesis
Presented to
The Academic Faculty

by

Batin Mert Karahasanoglu

In Partial Fulfillment
of the Requirements for the Degree
Master of Science in the
School of Electrical and Computer Engineering

Georgia Institute of Technology
MAY 2023

COPYRIGHT © 2023 BY BATIN MERT KARAHASANOGLU

**PROCESS DEVELOPMENT AND CHARACTERIZATION OF
PIEZOELECTRIC TRANSDUCERS ON FLEXIBLE SUBSTRATES FOR
HIGH FREQUENCY ULTRASOUND APPLICATIONS**

Approved by:

Dr. F. Levent Degertekin, Advisor
School of Electrical and Computer Engineering
Georgia Institute of Technology

Dr. Farrokh Ayazi
School of Electrical and Computer Engineering
Georgia Institute of Technology

Dr. A. Fatih Sarioglu
School of Electrical and Computer Engineering
Georgia Institute of Technology

Date Approved: April 21, 2023

To my parents, brother, and partner

ACKNOWLEDGEMENTS

I express my sincere gratitude to my advisor, Dr. F. Levent Degertekin for his invaluable guidance throughout my thesis. His expertise, insights, and advice have been instrumental in shaping my research, and I am indebted to him for his mentorship. Special thanks to Dr. Farrokh Ayazi and Dr. A. Fatih Sarioglu for their valuable feedback and guidance as my committee members.

I also extend my appreciation to all members of the Degertekin group for their supportive and enthusiastic presence. I would like to thank Dr. Yusuf S. Yaras for his excellent mentorship, guidance and brotherly friendship, both academically and personally. I am also grateful to Lee Bradley for helping me get up to speed with the project and experiments, and to Sait Kilinc for valuable technical discussions and moments of laughter.

My deepest gratitude goes to my dad, Okan, my mom, Sibel, and my brother, Berk for their unwavering support and encouragement throughout my academic journey. Their support, understanding, and motivation were invaluable to me. I will always be grateful for their sacrifices and devotion to my success.

Finally, I want to express my heartfelt thanks to my partner, Serra, for bearing with me from nearly the first day of my academic journey. Her encouragement and belief in me have been an endless source of motivation, and I could not have achieved this accomplishment without her by my side. I look forward to the next chapter of our lives together, hopefully not another academic one.

TABLE OF CONTENTS

ACKNOWLEDGEMENTS	v
LIST OF TABLES	viii
LIST OF FIGURES	ix
LIST OF SYMBOLS AND ABBREVIATIONS	xiii
SUMMARY	xv
CHAPTER 1. INTRODUCTION	1
1.1 Background of Piezoelectricity	2
1.2 Classification of Piezoelectric Materials	2
1.3 Material Properties	4
1.3.1 Ferroelectricity and Hysteresis Loop	4
1.3.2 Performance Parameters	5
1.3.3 Constitutive Equations	8
1.4 Equivalent Circuit Modelling	9
1.5 Piezoelectric Ultrasonic Transducer Applications	11
1.6 Objectives of This Work	12
1.7 Structure of Thesis	13
CHAPTER 2. FABRICATION PROCESS FOR PIEZOELECTRIC TRANSDUCERS	14
2.1 Material Selections	15
2.1.1 Transducer Material	15
2.1.2 Electrode & Electrical Interconnect Material	16
2.2 Fabrication Techniques	17
2.2.1 Screen Printing	17
2.2.2 Stencil Printing	19
2.2.3 Electron Beam Evaporation	21
2.3 Poling Process Requirement	21
2.4 Transducer Fabrication Process	24
2.4.1 Preparation	24
2.4.2 Electrode & Electrical Interconnect Layer Printing	26
2.4.3 Transducer Layer Printing	28
2.4.4 SMA Connection Wiring	30
2.4.5 Transducer Poling	32
CHAPTER 3. CHARACTERIZATION AND TESTING OF PIEZOELECTRIC TRANSDUCERS	36
3.1 Electrical Input Impedance Measurements	36
3.2 Electromechanical Coupling Coefficient Measurement	37

3.3	Poling Process Optimization	39
3.3.1	Electric Field	39
3.3.2	Duration	42
3.4	Hysteresis Loop Measurements	44
3.5	Piezoelectric Charge Constant Measurements	49
3.5.1	Berlincourt Method	50
3.5.2	Laser Interferometry Method	51
3.5.3	Resonance and Anti-resonance Method	52
3.5.4	Conducted Measurements	53
3.6	XRD Measurements	55
3.7	Acoustic Measurements	56
3.7.1	Hydrophone	56
3.7.2	Pulse-Echo	59
3.8	Transducer Simulations by KLM Model	61
3.9	Surface Roughness Measurements	67
3.10	Feature Dimension Limit Measurements	76
3.11	Flexibility Measurements	80
CHAPTER 4. ULTRASOUND APPLICATIONS OF PIEZOELECTRIC TRANSDUCERS		82
4.1	Single Element Phantom Study	82
4.2	Multiple Elements Phantom Study	86
4.2.1	Wrapping Effect	88
4.2.2	Outer Layer Implementation Effect	90
CHAPTER 5. CONCLUSION AND FUTURE WORK		92
5.1	Conclusion	92
5.2	Recommendations for Future Work	94
APPENDIX A		96
APPENDIX B		97
APPENDIX C		99
APPENDIX D		100
REFERENCES		101

LIST OF TABLES

Table 1 – Piezoelectric performance parameter comparison of piezo-ceramics, piezo-polymer and piezo-composites.	16
Table 2 - Electrical breakdown experiment result comparison between transducers with different thickness levels and their corresponding breakdown voltage levels.....	40
Table 3 - Repetitive transducer fabrication results with plastic and metal squeegee and their results comparison.	74
Table 4 Comparison of different transducer fabrication methods and their effects on surface roughness.....	75

LIST OF FIGURES

Figure 1 Domain wall distributions of piezoelectric materials under virgin state, poling state, and remanent state [19].....	5
Figure 2 Schematic illustration of Mason equivalent circuit [25].	10
Figure 3 Illustration of screen printing: Squeegee and ink application [49].....	18
Figure 4 Transparent patterning masks and 200 mesh count screens: Key elements of the screen printing process.....	19
Figure 5 Illustration of stencil printing: Squeegee and ink application [51].	19
Figure 6 Stencil preparation: Key steps including alignment, cutting, and redundant area removal.	20
Figure 7 Piezoelectric crystal structure schematic: Illustration of a) virgin state and b) dipole formation [53].	22
Figure 8 Dielectric breakdown in poling process: Microscopic surface image of affected device.	23
Figure 9 Positioning of evaporation mask in the e-beam evaporator.	27
Figure 10 Transducer fabrication process: Illustration of each required step.....	31
Figure 11 The effect on bubble formation on surface roughness due to high temperature processing.	34
Figure 12 The resonance and anti-resonance frequencies of transducer under two different poling conditions.....	38
Figure 13 Electrical input impedance comparison under varied external electric fields..	41

Figure 14 Visual demonstration of surface damages from dielectric breakdown: a) short device and b) functional device.	42
Figure 15 Comparison of electrical input impedance under varied poling times (1-10 minutes).....	43
Figure 16 Comparison of electrical input impedance under varied poling times (10-60 minutes).....	44
Figure 17 Hysteresis curve of ferroelectric material demonstrating P_r , E_c and P_s [62]. ..	46
Figure 18 Sawyer Tower's electrical circuit schematic [64].	48
Figure 19 Hysteresis measurement of piezoelectric transducer with P_r and E_c points.	49
Figure 20 Direction index of performance constants for piezoelectric transducers [67]..	50
Figure 21 Berlincourt method: Schematic demonstration of components [71].	51
Figure 22 Laser interferometry measurement setup for piezoelectric charge constant measurement [66].....	52
Figure 23 Piezoelectric charge constant measurement setup with d_{33} meter.....	54
Figure 24 Prepared d_{33} measurement setup with impact hammer	55
Figure 25 XRD measurement result of transducer between 10-90°	56
Figure 26 Acoustic measurement setup using a hydrophone.....	57
Figure 27 Electrical input impedance and hydrophone measurement comparison under different applied voltages for same transducer.	58
Figure 28 Comparison of hydrophone measurement results between two devices a) on glass substrate and b) on polyimide substrate.	59
Figure 29 Measurement setup for pulse-echo measurement with steel reflector.....	60
Figure 30 Acoustic echo measurement result from a steel reflector.....	61

Figure 31 Schematic illustration of circuit model employed in KLM-based simulation tool.	62
Figure 32 On-glass device: actual vs. simulated electrical input impedance measurement comparison.	64
Figure 33 On-polyimide device: comparison between actual and simulated electrical input impedance measurement.	65
Figure 34 Simulation results of the effect of different thickness outer layer implementation.	67
Figure 35 Standard fabrication method: Surface roughness measurement.	69
Figure 36 Surface roughness analysis: printing direction effect.	70
Figure 37 Surface roughness analysis: printing speed effect.	71
Figure 38 Surface roughness analysis: angle of attack effect.	72
Figure 39 Surface roughness analysis: substrate material effect.	73
Figure 40 Surface roughness measurement comparison of screen and stencil printed surfaces.	76
Figure 41 Microscopic images of prepared characterization stencils.	77
Figure 42 Microscopic images of prepared characterization elements.	77
Figure 43 Surface roughness measurements of characterization elements.	78
Figure 44 Microscopic surface roughness images a) without any surface defect and b) with surface defect.	79
Figure 45 Transducer Wrapping on Rods with Diameters of a) $4 \times 4 \text{ mm}^2$ transducer on 3.9 mm and b) $2 \times 2 \text{ mm}^2$ transducer on 2.4 mm.	81
Figure 46 Illustration of 1) perpendicular and 2) parallel wrapping orientations.	81

Figure 47 Setup for single element pulse-echo measurement	83
Figure 48 Single element human tissue mimicking gel pulse-echo measurement result.	84
Figure 49 Frequency response measurement of single element transducer.....	85
Figure 50 Multiple element transducer formation wrapped around catheter.....	86
Figure 51 a) Photo of the acoustic gel phantom with a PP target and b) Pulse-echo measurement setup.....	87
Figure 52 Echo signal measurement from different targets.....	88
Figure 53 Hydrophone measurement of the transducer before wrapping (planer) and after wrapping (curved).....	89
Figure 54 Echo measurement of element a) before and b) after implementation of outer layer.....	90

LIST OF SYMBOLS AND ABBREVIATIONS

CMUT	Capacitive Micromachined Ultrasonic Transducer
d	Piezoelectric Charge Constant
D	Piezoelectric Charge Density Displacement
E_c	Coercive Field
FEM	Finite Element Model
FFT	Fast Fourier Transform
f_p	Parallel Resonance Frequency
f_s	Series Resonance Frequency
g	Piezoelectric Voltage Constant
IVUS	Intravascular Ultrasound
k	Electromechanical Coupling Factor
N_t	Piezoelectric Frequency Constant
P	Polarization
PMUT	Piezoelectric Micromachined Ultrasonic Transducer
P_r	Remanent Polarization

P_s Saturation Polarization

PVDF Polyvinylidene Fluoride

PZT Lead Zirconate Titanate

S Piezoelectric Strain

Sa Arithmetical Mean Height

Spc Arithmetic Mean Peak Curvature

Sq Root Mean Square

Ssk Skewness

Sz Maximum Height Difference

t_d Domain Wall Motion Time

t_n Nucleation Time

t_s Domain Switching Duration

XRD X-ray Diffraction

SUMMARY

This master's thesis focuses on the development and characterization of a 0-3 composite piezoelectric material (PiezoPaint™), which can be used to fabricate transducers and transducer arrays on flexible substrates for high frequency ultrasound imaging and sensing applications. The aim is to overcome the limitations of ceramic piezoelectric materials such as their high sintering temperature and rigidity, which restrict their use in applications that require conformal structures on non-planar surfaces such as catheters. To achieve this, the several fabrication methods utilized, including screen printing and stencil printing, to form transducers on flexible substrates like polyimide with thickness and lateral dimensions ranging from 15-100 μm at low temperatures ($<140^\circ\text{C}$). The poling process was optimized for time and voltage levels, and performance parameters were characterized to understand the effect of each process parameter. The ultrasound performance of transducers was characterized through pulse-echo and hydrophone measurements. Bending tests were conducted to evaluate the curvature limits of different dimension transducers without any detrimental effects. Furthermore, a compact packaging method was demonstrated where the transducer array and electrical interconnects were packed to achieve a sleeve-like structure suitable for integration with different devices, such as microcatheters. This sleeve like packed transducers tested in tissue mimicking phantom study. The results indicate that the developed transducers are suitable for intravascular ultrasound applications such as ranging and lumen sizing in the 5-15 MHz range with broad bandwidth. Overall, this study presents a promising flexible, low-cost approach for the advancement of high-performance ultrasonic transducers and transducer arrays.

CHAPTER 1. INTRODUCTION

The use of ultrasound imaging has become widespread in clinical practice for over 60 years, and it currently accounts for one-fourth of all imaging procedures globally [1, 2]. In recent years, there has been a growing demand for ultrasound transducers in various medical applications beyond traditional external probe-based imaging. Wearable ultrasound devices and intravascular and intracardiac ultrasound imaging for instance, have gained increasing attention [3-5]. However, this demand has brought about a significant challenge for conventional piezoelectric materials and fabrication methods, which are typically limited by factors such as brittleness, high costs, and the inability to be processed on flexible polymer substrates due to their high processing temperatures [6].

Piezoelectric polymers have been extensively studied to address these challenges because of their mechanical flexibility and low processing complexity [7, 8]. However, their low piezoelectric coefficients compared to ceramics limit their performance [9]. Thus, piezoelectric ceramic-polymer composites have been explored as a possible solution to combine the advantages of both materials. These composites aim to maintain the mechanical flexibility of polymers while taking advantage of the higher piezoelectric performance parameters of ceramics [10, 11]. By doing so, they offer an alternative approach to the development of fully flexible piezoelectric transducer arrays for catheter-based imaging applications.

The focus of this work is on the development and characterization of piezocomposite transducers on flexible substrates for high-frequency ultrasound applications.

1.1 Background of Piezoelectricity

The discovery of the direct piezoelectric effect, which was made by the Curie brothers in 1880, revolutionized the field of materials science [12]. The term "piezo" originates from the Greek word for pressure, and as the name implies, direct piezoelectric materials can generate an electrical potential when subjected to pressure [13]. Shortly after this discovery, Lipmann demonstrated the converse effect from a thermodynamic perspective. This converse piezoelectric effect involves the deformation or strain of a material under an applied electric field.

Initially, single crystalline materials such as quartz and Rochelle salt were the first materials to exhibit piezoelectric behavior. The first practical application of this phenomenon was in the form of sonar, developed by Langevin during World War I [12]. From that point on, piezoelectric materials found use in various applications such as underwater devices, ultrasonic transducers, microphones, and accelerometers. However, the limited performance of single crystal materials hindered their commercialization.

The discovery of lead zirconate titanate (PZT) in the 1950s offered the possibility of tailoring the behavior of piezoelectric materials. As a result, PZT became one of the most widely used piezoelectric materials due to its superior performance characteristics [14].

1.2 Classification of Piezoelectric Materials

Piezoelectric materials are a class of electrically insulating materials that can develop an electrical dipole structure under an applied electric field. This occurs due to the shift in the positions of positively and negatively charged particles at the atomic level, resulting in

the polarization of the material. There are three types of polarization: electrical, ionic, and dipolar or orientation [15].

Electrical polarization occurs when an external electric field causes the displacement of negatively charged particles with respect to positively charged particles. This type of polarization can be observed in all dielectric materials and exists only under an external electric field. Ionic polarization occurs in materials that are ionically bonded. The external applied field moves cations to one side and anions to the other, leading to a net dipole within the material. The last type, orientation polarization, is observed in materials that possess permanent dipole moments. Polarization results from the rotation of permanent moments of the material. This work focuses on optimizing the orientation polarization, and the following chapters will detail the methods and results of this optimization.

Dielectric materials are classified based on their crystal symmetry structures, and piezoelectric materials are a subcategory of dielectric materials [16]. There are 32 crystal classes within the dielectric materials category, and 11 of them have a center of symmetry and are called paraelectric, as they do not exhibit piezoelectric effects. The remaining 20 classes without a center of symmetry exhibit piezoelectric effects and are called piezoelectric materials. Among these, 10 piezoelectric crystal classes have spontaneous polarization and can remain polarized without external physical effects; these are known as pyroelectrics. If the orientation of pyroelectrics can be changed by an external electric field, they are called ferroelectrics. Orientation dependence on the electric field is important in ultrasonic applications where the transmit and receive signals are expected to be in a specific direction. Therefore, ferroelectrics are widely used as transducer materials

in ultrasonic transducers, including the material optimization regarding orientation polarization that is discussed in this work's subsequent chapters.

1.3 Material Properties

1.3.1 Ferroelectricity and Hysteresis Loop

As previously mentioned, the orientation of spontaneous polarization in ferroelectric materials can be altered by an external electric field. However, the asymmetry of crystal structures disappears above the critical temperature, known as the Curie temperature. This temperature marks the loss of magnetic property and is present in materials with dipole moment structure [17]. The direction change of dipole moments can be observed through hysteresis loops. The existence of hysteresis loops is considered evidence of a material being ferroelectric [18].

Hysteresis loops also provide important characteristics of materials, such as the coercive field (E_c), remanent polarization (P_r), and saturation polarization (P_s). The saturation polarization value is the maximum possible polarization value, and applying a higher electric field does not alter the sample's polarization. The remanent polarization value is the polarization of the sample with no external field after the polarization process. Finally, the coercive field is the delay in polarization when changing direction. Even under an external electric field, the sample does not exhibit any polarization at this point. These materials require polarization to display a piezoelectric response.

Ferroelectric materials initially have a molecular structure that lacks orientation towards any specific direction, resulting in a randomly distributed crystal directionality.

This means that polarity cannot be observed under an external electric field or stress in any particular direction. To create a dipole structure, a high external electric field is required to align the orientation of the molecules towards a specific direction. This process is known as the saturation state, which involves the application of a high external field to both sides of the transducer. When the external poling voltage is removed, some molecules relax, but due to the pinning effect of microscopic defects on the crystalline lattice, the dipole structure is preserved even after the external electric field is removed. This state is called the remnant or spontaneous polarization. The overall process is referred to as the poling process, and the virgin, saturation, and after relaxation stages of poling are illustrated in Figure 1. This effect will be explored in detail in the upcoming chapters.

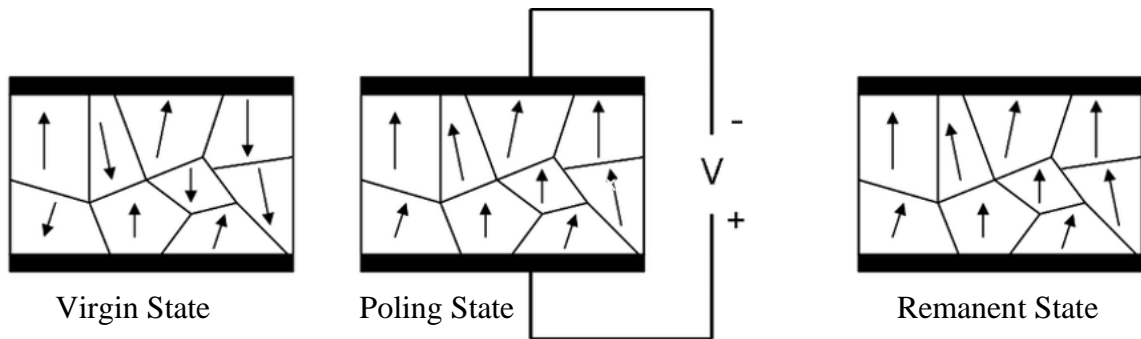


Figure 1 Domain wall distributions of piezoelectric materials under virgin state, poling state, and remanent state [19].

1.3.2 Performance Parameters

1.3.2.1 Charge Constant (d)

The constant described here establishes a relationship between the applied mechanical force and the generated charge per unit area and is typically measured in Coulombs per Newton (C/N). This parameter is particularly important for actuator

applications, as it provides a direct correlation between the applied force and the resulting charge, or vice versa.

$$d = \frac{\textit{Generated Charge}}{\textit{Applied Stress}} \quad (1)$$

Two primary direct measurement methods are available for the measurement of the charge constant: the quasi-static method (also known as the Berlincourt method) and the laser interferometry method. In addition to these direct methods, the charge constant can be calculated indirectly using resonance and anti-resonance frequencies. The following chapter will provide a detailed analysis of these methods.

1.3.2.2 Voltage Constant (g)

The relationship between applied mechanical stress and generated electric field is described by a constant. Expressed in units of voltage-meter per Newton (Vm/N), this constant is a crucial parameter for sensor applications as it establishes a connection between stress and electric field.

$$g = \frac{\textit{Electric Field Generated}}{\textit{Applied Stress}} \quad (2)$$

The g constants are calculated from the piezoelectric charge constants (d) where relation between them depends on relative permittivity of material ϵ .

$$g = \frac{d}{\epsilon} \quad (3)$$

1.3.2.3 Young Modulus (Y) and Elastic Compliance (s)

The Young's Modulus is defined as the stress-to-strain ratio, and materials with a high value of Young's Modulus, such as ceramics, are typically more rigid. On the other hand, elastic compliance is the strain-to-stress ratio, and materials with a high value of elastic compliance, such as rubber bands, are generally more flexible.

$$Y = \text{stress/strain} = \sigma/\epsilon \quad (4)$$

$$s = \text{strain/stress} = \epsilon/\sigma \quad (5)$$

1.3.2.4 Frequency Constant (N_t)

This constant establishes a connection between the thickness of a sample and its resonant frequency value. In other words, with a given frequency constant and thickness value, it is possible to calculate the resonant frequency.

$$N_t = f_r * t \quad (6)$$

1.3.2.5 Dielectric Constant (ε)

The dielectric constant refers to a material's capacity to store electrical energy per unit of applied electric field, which is equivalent to its ability to polarize when subjected

to an external electric field. This property is dimensionless and is often used to describe a material's response to an electric field.

1.3.2.6 Electromechanical Coupling Factor (k)

This constant is indicator of the effectiveness of energy conversion between generated electrical energy per applied mechanical energy or generated mechanical energy per applied electrical energy.

$$k = \frac{\text{Mechanical Energy Converted}}{\text{Electric Energy Input}} \quad (7)$$

1.3.2.7 Dielectric Dissipation Factor (tan δ)

The loss tangent, or dielectric dissipation factor, is a physical constant that quantifies the amount of energy that is converted to heat during the transfer of electrical energy in a dielectric material. Because energy cannot be completely converted from one form to another without some loss, the dissipation factor is used to express the amount of energy lost as heat during these conversions. It is typically expressed as a percentage and has no units.

1.3.3 *Constitutive Equations*

The parameters mentioned above are used to derive the constitutive equations for both the direct and reverse piezoelectric effects. The direct relation, in which applied force causes a charge displacement (represented by D), is employed in sensor applications. Conversely, the indirect relation, in which applied electricity causes strain (represented by

S), is used in actuator applications. Transducer applications involve both sensing and actuating, which will be elaborated upon. Since there is a directionality factor for piezoelectric performance parameters, these equations can be written in the matrix format where directionality of each constant is also included as shown in the Equation 8.

$$\begin{aligned}
 \begin{bmatrix} S_1 \\ S_2 \\ S_3 \\ S_4 \\ S_5 \\ S_6 \end{bmatrix} &= \begin{bmatrix} s_{11}^E & s_{12}^E & s_{13}^E & 0 & 0 & 0 \\ s_{21}^E & s_{22}^E & s_{23}^E & 0 & 0 & 0 \\ s_{31}^E & s_{32}^E & s_{33}^E & 0 & 0 & 0 \\ 0 & 0 & 0 & s_{44}^E & 0 & 0 \\ 0 & 0 & 0 & 0 & s_{55}^E & 0 \\ 0 & 0 & 0 & 0 & 0 & s_{66}^E = 2(s_{11}^E - s_{12}^E) \end{bmatrix} \begin{bmatrix} T_1 \\ T_2 \\ T_3 \\ T_4 \\ T_5 \\ T_6 \end{bmatrix} + \begin{bmatrix} 0 & 0 & d_{31} \\ 0 & 0 & d_{32} \\ 0 & 0 & d_{33} \\ 0 & d_{24} & 0 \\ d_{15} & 0 & 0 \\ 0 & 0 & 0 \end{bmatrix} \begin{bmatrix} E_1 \\ E_2 \\ E_3 \end{bmatrix} \\
 \begin{bmatrix} D_1 \\ D_2 \\ D_3 \end{bmatrix} &= \begin{bmatrix} 0 & 0 & 0 & 0 & d_{15} & 0 \\ 0 & 0 & 0 & d_{24} & 0 & 0 \\ d_{31} & d_{32} & d_{33} & 0 & 0 & 0 \end{bmatrix} \begin{bmatrix} T_1 \\ T_2 \\ T_3 \\ T_4 \\ T_5 \\ T_6 \end{bmatrix} + \begin{bmatrix} \varepsilon_{11} & 0 & 0 \\ 0 & \varepsilon_{22} & 0 \\ 0 & 0 & \varepsilon_{33} \end{bmatrix} \begin{bmatrix} E_1 \\ E_2 \\ E_3 \end{bmatrix}
 \end{aligned} \tag{8}$$

1.4 Equivalent Circuit Modelling

As stated in the literature [20], there exist three widely used circuits for modeling piezoelectric transducers: the Mason [21], Krimholtz-Leedom-Matthaei (KLM) [22], and Redwood models [23]. On top of these models more software-based models are also presented that employs finite element model (FEM) [24]. Each of these models has its own set of benefits depending on the transducer's intended use and mode of operation. It is crucial to have an equivalent circuit model tailored to the specific application in order to fine-tune the transducer's dimensions through simulation before fabrication and to facilitate the examination of various process parameters' effects.

The Mason model is demonstrated in the Figure 2, which represents piezoelectric materials using one electrical and two mechanical ports separated by an ideal

electromechanical transformer. This model is widely used for free and mass-loaded applications requiring transient response, and for determining material constants [25].

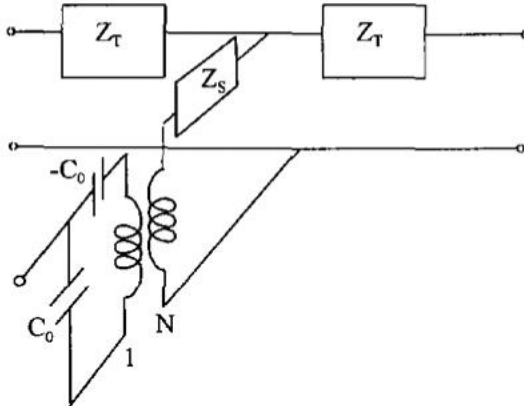


Figure 2 Schematic illustration of Mason equivalent circuit [25].

The Mason model has been noted to have a limitation where negative capacitance is required at the electrical port. However, this limitation is addressed by the Redwood model [23], which demonstrates that the negative capacitance requirement can be transferred to the acoustic side as a component of the acoustic line [25].

Another equivalent model, known as the KLM model, was proposed by Leedom et al [22]. Similar to Redwood model, this model is also improvement on the Mason model where they have introduced negative capacitance element. The KLM model has been extensively used for imaging applications, and it has been reported that some of the earlier commercially available modeling tools utilized this model [26]. Details of these models will not be discussed in the scope of this work. The reader is referred to [21-23, 27] for more details.

1.5 Piezoelectric Ultrasonic Transducer Applications

Two significant achievements in the field of medical ultrasound occurred in the 1950s, represented by the works of Edler et al. and Donald et al. Edler et al. successfully performed the first echocardiogram to diagnose mitral stenosis [28], while Donald et al. revolutionized the field of obstetrics and gynecology with their publication on using ultrasound to investigate abdominal masses [1]. These works drew attention to medical imaging for diagnosis, which has continued to evolve over the years.

However, these early works suffered from several limitations, such as poor image quality, bulky equipment requirements, and operator dependence. To address these challenges, efforts have been focused on various interdependent aspects, including transducer fabrication processes to develop smaller and better-performing devices, integrated circuit development to enhance transducer performance, and signal processing algorithms to improve image quality. This work focuses specifically on the process development aspect.

Transducer development aspect can be categorized into piezoelectric materials, capacitive micromachined ultrasonic transducers (CMUT), and piezoelectric micromachined transducers (PMUT). A comparison of these technologies is reported in [29]. Considering the flexibility, application tunability, and ease of fabrication requirements for this work, the focus is on the use of piezoelectric material-based transducers.

Piezoelectric transducers are increasingly being used in medical applications beyond the traditional external probe based medical imaging. These applications now include non-

invasive, wearable ultrasound devices as well as catheter-based intravascular and intracardiac ultrasound imaging. One example of a wearable application is the work by Hu et al. [3] who demonstrated a wearable cardiac ultrasound imager for dynamic cardiac monitoring. They utilized 1-3 piezoelectric composites as transducer material and built it on a stretchable substrate called styrene-ethylene-butylene-styrene (SEBS) to make it conformal to applicable surfaces such as human skin, reducing its bulkiness. Another example is the work by Wang et al. [4] who reported a wearable ultrasound imaging device with a rigid transducer probe and a bio-adhesive hydrogel-elastomer couplant to be applicable to non-planar surfaces. They reported ultrasound probes with three distinct center frequencies of 3, 7, and 10 MHz. In terms of catheter-based applications, Hong et al. [30] reported a dual-mode imaging catheter for intravascular ultrasound application. Their catheter design includes both forward and side-looking ultrasonic transducers at 20 MHz and 40 MHz respectively. They utilized PZT-5H material, which is a piezo-ceramic material, but their proposed work requires micro-machining on a specific catheter that can only be used for a specific application. Wildes et al. [31] described a catheter-based application for real-time 3-D intracardiac echocardiography, with a reported resonant frequency range between 3.4-9 MHz and a measured center frequency of 5.6 MHz. Additionally, our group [32] demonstrated a 12 MHz forward-looking catheter for real-time intravascular ultrasound (IVUS) imaging system. This work utilized CMUT on CMOS technology, which was placed on a 6 Fr catheter with a 12 MHz center frequency.

1.6 Objectives of This Work

The aim of this study is to fabricate flexible piezoelectric transducers for use in high frequency ultrasound applications, specifically intravascular ranging and lumen sizing,

using composite piezoelectric material at a low process temperature. To achieve this goal, the research is divided into three main parts. The first part focuses on the fabrication and process development of flexible piezoelectric transducer/transducer arrays for high frequency application. The second part involves characterizing the piezoelectric transducers, while the final part is dedicated to applying the transducers for ultrasound applications.

1.7 Structure of Thesis

This thesis is structured in the following manner. Chapter 1 presents an introduction to the background of piezoelectricity, its characteristics, recent applications, and the objectives of this study. Chapter 2 details the fabrication and process development of flexible piezoelectric transducers/transducer arrays. In Chapter 3, the characterization of the fabricated transducers is demonstrated through several means. Chapter 4 explores the application side of the fabricated transducers. Finally, Chapter 5 provides a conclusion and recommends future work to be completed for further improvement on the current transducers.

CHAPTER 2. FABRICATION PROCESS FOR PIEZOELECTRIC TRANSDUCERS

The focus of this thesis chapter is to investigate the manufacturing process involved in fabricating piezoelectric transducers. This process involves multiple stages, including the selection of appropriate materials, fabrication techniques for individual layers, mask preparation, fabrication, and poling steps.

Two main materials are used in this work. These are piezoelectric composite and silver ink. Commercially available composite piezoelectric material, PiezoPaint™ (CTS Ferroperm, Denmark) [33] is utilized as transducer material since it provides advantages of piezo polymers in terms of mechanical properties such as flexibility and piezo ceramics in terms of performance constants such as comparably higher piezoelectric constant. Silver ink AG-510 (Kayaku Advanced Material Inc., USA) is utilized as electrode material. The dry temperature, various process availability and mechanical properties of the ink makes it suitable for this work. Both materials will be analyzed in detail.

After the determination of materials, literature is reviewed to compare alternative fabrication methods. There are several fabrication methods are reported that can be used for fabrication of piezoelectric composites such as screen printing [34, 35], stencil printing [36], spray coating [37] in addition to these ceramic processing methods such as dice and fill [38], injection molding [39], laser cutting [40] and 3D printing [41]. Among these fabrication methods, the stencil printing fabrication method is the primary technique employed in the development of transducers for this study. Because this method offers

unique advantages such as tunability of thickness, adaptability to diverse geometries, and high-volume production capability, allowing for the development of a streamlined process flow to produce transducers of varying thicknesses and geometries. The piezo layer is mostly fabricated with this method however, screen printing and evaporation methods are also utilized for electrode printing. Screen and stencil printing methods are both requires prior preparation to achieve certain process parameters such as surface roughness and thickness. The preparation of screens including mesh size selection, pattern printing and stencils including the material selection and their effects on the fabrication parameters will be examined.

Transducer fabrication process consists of several stages such as electrode printing, piezo-layer printing, drying process of these materials. Each of these steps will be explained and demonstrated by images in this chapter.

Finally, poling process of transducer will be explained. It is required step for any ferroelectric materials to be functional. There are several parameters to consider for poling such as electric field, temperature, and duration. The effect and importance of these parameters as well as their effect on crystal structure will be explained.

2.1 Material Selections

2.1.1 Transducer Material

The composite materials maintain both mechanical flexibility of polymers and high piezoelectric coefficients of ceramics that offers alternative development approach for piezoelectric transducer arrays. The necessity of piezocomposites with good mechanical

and piezoelectric properties attract attention in the recent years, and development of different piezocomposites are reported in the literature [35, 42-44]. The material development is not focus of this work. We have chosen commercially available piezocomposite material called PiezoPaint™. The datasheet of this product can be found in the Appendix A. It is a 0-3 piezocomposite material with hard PZT ceramic Pz24 (CTS Ferroperm, Denmark) powder suspended in a flexible polymer. It is suitable for soft and flexible substrates, screen and stencil printing methods and has low curing temperature. Table 1 demonstrates material properties of PiezoPaint™ with comparison to commercially available piezoelectric polymers and ceramics. Mechanical flexibility of the material with comparably better piezoelectric performance parameters makes it suitable for challenges that we are targeting to solve in the scope of this work.

Table 1 – Piezoelectric performance parameter comparison of piezo-ceramics, piezo-polymer and piezo-composites.

Properties/Parameters	Unit	Piezo-ceramics (PZT) [45]	Piezo-polymers (PVDF) [45]	PiezoPaint™ [33]
Electromechanical Coupling Factor	%	30	12	8.2
Charge Constant	pC / N	225-590	24-34	40
Dielectric Constant	-	1180	10-15	80
Curie Temperature	°C	386	80	330
Acoustic Impedance	MRayl	30	2.7	13.9
Density	g/cm ³	7.5	1.78	5.0

2.1.2 Electrode & Electrical Interconnect Material

Silver based inks gained attention with increasing demand for flexible electronics [46]. In the scope of this work, AG-510 is utilized as electrical interconnect material. The datasheet of this material can be found in the Appendix B. It is a silver-filled electrically

conductive ink which is suitable for screen printing and stencil printing applications. In addition to these, it has excellent adhesion to polyester, polyimide substrates which is also important for our application. The required temperature of 130°C for drying process is in line with the low temperature expectations. Considering all these properties of material, it is selected and used in the scope of this work.

2.2 Fabrication Techniques

In the scope of this work, three different fabrication method is used to produce electrode & electrical interconnect layers and piezo layers. These methods are stencil printing, screen printing and evaporation. Process flows of these printing methods are giving below with their suitability to deposition of different layers.

2.2.1 Screen Printing

Screen printing method is one of the most used printing methods for printed electronics. It is simple and fast method which does not require any expensive dedicated tool or cleanroom processing [47, 48]. The screen printing setup requires mesh screen, squeegee, and substrate. The poured ink onto the patterned mash screen is squeegeed to move across through patterns which results in the transfer of ink through open pores on mesh to beneath substrate which is demonstrated in Figure 3. In our application both silver ink and piezo paint is suitable for screen printing method.

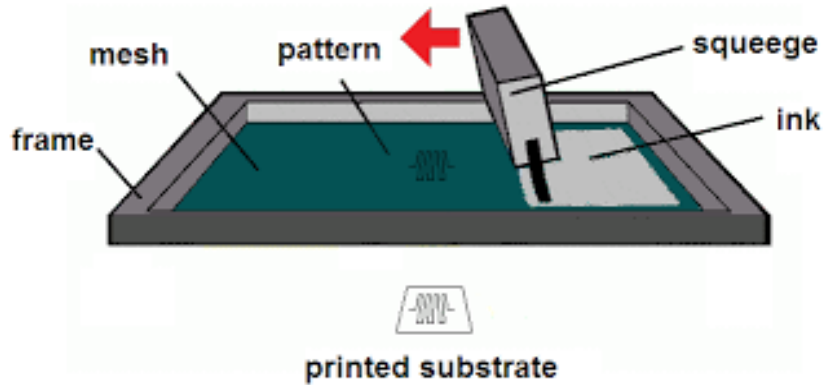


Figure 3 Illustration of screen printing: Squeegee and ink application [49].

Even it is a simple process, the characteristic and print quality depend on various factors such as ink viscosity, printing speed, mesh size, geometry of squeegee [48]. The preparation of mesh screens is required step prior to printing stage. There are couple of parameters to consider before selecting the right mesh screen size which effect print resolution. In our case, mesh size of 157 to 230 is suggest by the datasheet of silver ink. Since screen printing method is mainly utilized for electrode and electrical interconnect printing, polyester screen with 200 mesh is selected to be used in this work as shown in the Figure 4. To pattern this mesh screens, masks are designed in the AutoCAD, and they are printed on transparent sheets using printer. After, mesh screens are coated with emulsion to be patterned. Masks are aligned on the coated mesh screens, and they are exposed to high power light for 60 minutes. After the exposure of lights, un-cured parts are rinse with water and mesh screen is ready to use as shown in the Figure 4. In the scope of this work, this printing method is mainly used for electrode printing.



Figure 4 Transparent patterning masks and 200 mesh count screens: Key elements of the screen printing process.

2.2.2 Stencil Printing

Stencil printing is another contact printing method that utilizes stencils and printable inks. This method is simple, fast, and affordable [50]. In addition to these, it provides better surface profile for the use cases of high viscous materials since the used metal blade surface is main process effect on surface profile rather than mesh wires in comparison to screen printing. The surface roughness comparison of both methods will be

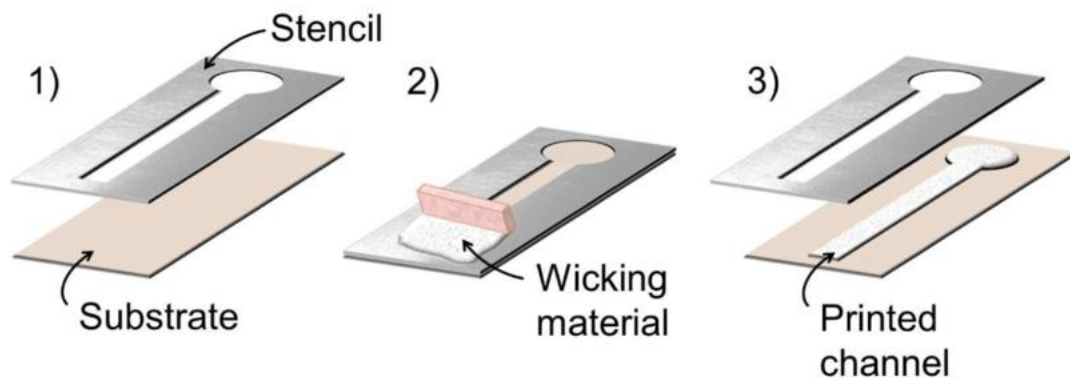


Figure 5 Illustration of stencil printing: Squeegee and ink application [51].

examined in the following section. Figure 5 demonstrate deposition of ink to substrate with stencil printing method. In our application both silver ink and piezo paint are suitable for screen printing method.

In the scope of this work, various thickness polyimide films are used as stencil material. Since thickness levels of deposited ink is directly correlated with stencil film thickness, it is chosen depending on specific application. Commonly used thickness for electrode layers is 12.5 μm and for piezo layer is 50 μm . Pieces of polyimide films are placed on glass slides and edges are taped to ensure most possible flatness of the surface as shown in the Figure 6. Pattern are drawn in the AutoCAD and to pattern polyimide films, laser cutter (WS FLEX, OPTEC Laser Group, USA) is utilized. To edge through all the thickness of polyimide films, different number of iterations are required for different level of polyimide thicknesses. After cutting the polyimide films, redundant area is cleaned, and final stencil formation is achieved as shown in the Figure 6.

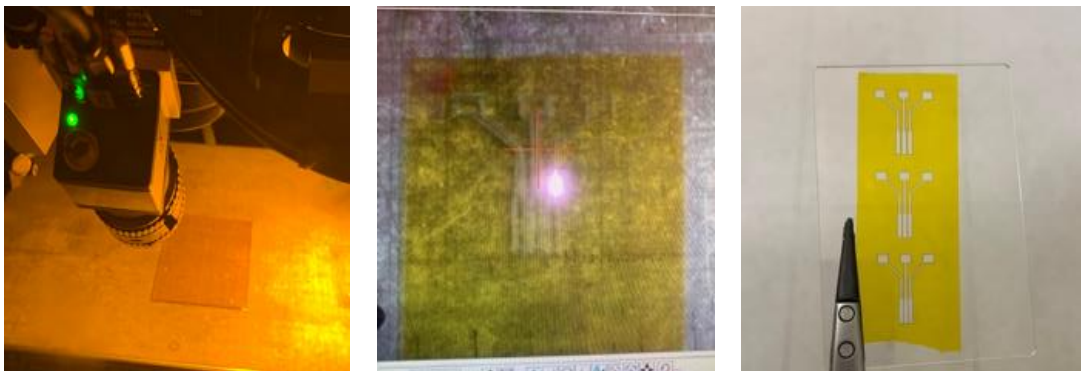


Figure 6 Stencil preparation: Key steps including alignment, cutting, and redundant area removal.

2.2.3 Electron Beam Evaporation

Compared to stencil and screen printing methods, sub-micron thickness profiles are achievable with electron-beam evaporation method. However, this method requires dedicated tool and cleanroom processing which is comparably expensive and relatively difficult process. The working principle of this methods depends on evaporation of material under highly energetic electron beam [52] which makes it physical deposition method. The evaporated materials cover the surface of target substrate. The utilization of shadow mask on surface can lead to patterning of desired shapes. In the scope of this work, evaporation is utilized to achieve sub-micron thick bottom electrodes. Final thickness level of 10 nm Cr and 300 nm Gold is deposited with 1Å per second and 1Å per second deposition rates respectively for Cr and Gold.

2.3 Poling Process Requirement

In their initial or "virgin" states, the molecular structures of ferroelectric materials lack directionality towards any specific orientation, resulting in randomly distributed crystal directionality as explained previously. Furthermore, polarity cannot be observed under an external electric field or stress in any direction. The application of high external electric field considerably under Curie temperature is required to align orientation of molecules towards specific direction where dipole structure will be created. Second state is saturation state where high external field is applied to two sides of transducer which utilizes asymmetrical crystal structure of piezoelectric molecules to align them in a way towards applied field. The asymmetrical crystal structure of PZT is shown in the Figure 7. It can be observed that ions do not have center of symmetry which means negatively

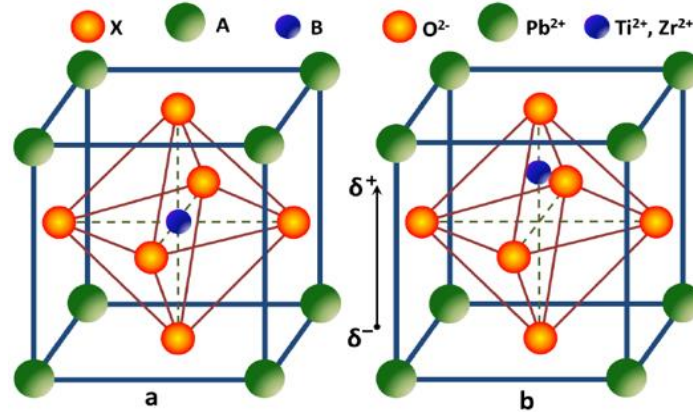


Figure 7 Piezoelectric crystal structure schematic: Illustration of a) virgin state and b) dipole formation [53].

charged ions are denser on one side and positively charged ions are on the other side. This situation leads to separation to these charges towards different directions under applied external field which leads to dipole structure within the molecule. This effect will be observed for each molecule because of this dipole structure as shown in Figure 7. will be obtained. The pinning effect can be observed due to external applied field where microscopic defects on crystalline lattice causes dipole structure to be preserved even after removing external electric field. This state is called remnant polarization or spontaneous polarization. Figure 1 demonstrates three states of molecular structure through the process of poling. The measurement methods to analyze remnant polarization will be examined in the next chapter.

The acoustic performance of transducers is dependent on the poling process. DC poling procedure is commonly used method in the literature [54, 55] where it is also utilized for in this work. This method is based on application of DC voltage to both sides of transducer for specific time duration at specific temperature value. For that, poling voltage level, poling temperature and poling duration is main parameters to be optimized. The main

goal of this process is achieving maximum domain alignment with minimum external electric field, close to room temperature process and shortest time duration. The optimization process of these parameters will be examined in the next chapter.

The limiting factor for DC voltage is potential dielectric breakdowns. Since piezoelectric materials are dielectric, voltage level exceeds breakdown voltage leads to conductive behavior of material for that electrical breakdown happens. This situation causes to dis-function of transducer. Figure 8. demonstrates a device which faced dielectric breakdown due to high external electric field. To have functional devices with maximum domain alignment, devices are poled at voltage level which is slightly lower than dielectric breakdown voltage. Since PiezoPaint™ is composite material, the dielectric breakdown voltage is found by experiment and results will be demonstrated in the next chapter.



Figure 8 Dielectric breakdown in poling process: Microscopic surface image of affected device.

Secondly, the duration of poling process is important parameter to be examined. It is stated that [56] minimum required polarization switching duration (t_s) can be approximated by the combination of nucleation time (t_n) where it is required time for all nuclei and the

domain wall motion time (t_d) where it is required duration for one domain to move through sample.

$$t_s \cong t_n + t_d \quad (9)$$

$$\frac{1}{t_n} = \frac{1}{t_0} * \exp\left(\frac{-a}{E}\right) \quad (10)$$

$$\frac{1}{t_d} = \frac{u * E}{d} = \frac{u * V}{d^2} \quad (11)$$

Equation 9 demonstrates the total switching time where t_0 and a are constants, E is electric field, u is mobility of domain wall and V is applied voltage. It is also demonstrated by Fatuzzo et al. [56] that the switching time is temperature dependent where higher temperature levels lead to faster motion times so required duration time decreasing. However, Curie temperature should not be exceeded where remnant polarization is lost, and domains will be randomly oriented. The duration of poling process and the temperature effect on device performance is examined and the optimum parameters are reported in the next section.

2.4 Transducer Fabrication Process

Printing process consists of electrode printing, transducer printing, wiring connectors and poling process. These steps are explained below with step-by-step images.

2.4.1 Preparation

Initial step is preparation of the required setup for device fabrication process. One full cycle of device fabrication requires following items to be completed. The name of each item is given with their purpose in the fabrication process.

Transducer Material: PiezoPaint™ is utilized to print piezoelectric layer.

Electrode & Electrical Interconnect Material: AG-510 silver ink is used to print electrodes.

Substrate Materials: Quartz glass slides and polyimide thin films are utilized with varying thickness including 1 mm for glass and 0.5,1,2 μm for polyimide.

Patterned Screen or Stencil: Patterned stencils and screens are used to print electrode and transducer layers.

Hot Plate: Utilized for drying purposes of silver ink and both drying and poling process of transducer.

DC Supply: Utilized for poling process. Depending on the thickness level, up to 600V can be required so DC supply is chosen accordingly.

Male SMA Connector: Utilized for electrical interconnections where they provide high frequency capabilities with small size and lightweight.

Adhesive Layer: Utilized to attach SMA connector onto substrate. Ultra-Light Weld Adhesive, 3095-Gel by (Dymax Corp., USA) is used as adhesive layer since it can be used up to 160°C which is lower than operation range of this work.

Light Welder: Utilized to cure adhesive layer.

SMA to Coaxial Converter: Utilized to connect transducers to poling and measurement devices.

Metal Squeegee or Plastic Card: Utilized to drag ink materials on screens or stencils.

Kapton Tape: Used to attach stencil mask on glass or polyimide substrate to prevent any motion during the printing process.

IPO (Isopropyl Alcohol): Used to clean substrates and piezo layer, silver-ink before the drying process of them.

Handling Tweezer: Utilized move substrate on and off hot plate.

Timer: Utilized to keep track of poling and drying process times.

Multimeter: Utilized for connectivity control between electrodes and connectors

Microscope (OPTIONAL): Used for visual inspections to see potential defects on surface.

2.4.2 Electrode & Electrical Interconnect Layer Printing

After the preparation of required items, the first step is bottom electrode printing. To print bottom electrode, polyimide as substrate material is taped on glass and the surface of polyimide is cleaned by IPO. The glass substrate is used as backing layer for easy handling purposes since polyimide by itself is too lightweight to carry SMA connectors.

For stencil printing, the stencil is placed and aligned on the substrate then taped to substrate in order to prevent potential movement of it during the fabrication process. After that drops of silver ink is placed near to stencil pattern and by dragging metal squeegee,

silver ink is printed on the substrate. Roughly 30° angle and mild pressure on metal squeegee provides best surface roughness and thickness performance compared to alternatives which will be examined in the next chapter.

For screen printing method, the screen is placed and aligned on the substrate. Silver ink drops are placed near to patterned screen opening and by dragging plastic squeegee, bottom electrode is printed. 45° angle and high pressure on plastic squeegee provides best surface roughness and thickness performance compared to alternatives.

For evaporation method, electron beam evaporator Explorer (Denton Vacuum, USA) is utilized which is located inside of the cleanroom. It requires placing shadow mask attached substrate material onto sample holder frame. Required thickness level and deposition rate needs to be entered to tool software. In the scope of this work, 10 nm Cr is deposited with 1Å per second deposition rate and 300 nm Ag is deposited with 3Å per second deposition rate. Figure 9. demonstrates placed shadow mask and glass substrate onto sample holder in electron beam evaporator tool.

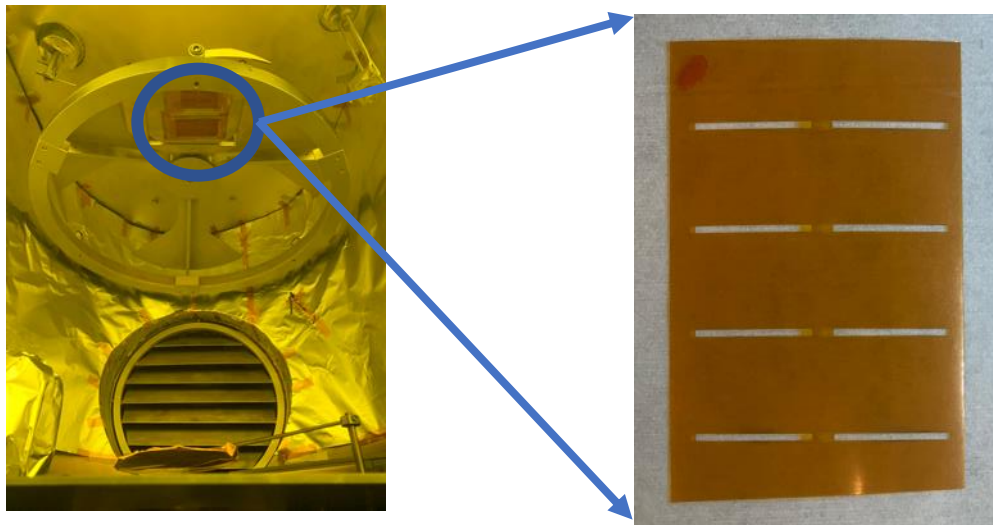


Figure 9 Positioning of evaporation mask in the e-beam evaporator.

After the completion of printing by screen or stencil printing, excluding evaporation, electrode on substrate is placed on hot plate at 130°C to be dried for 5 minutes as indicated in the datasheet of Silver Ink. It is good practice to measure connectivity of electrode on several points to detect potential disconnection after dry process. If any disconnection is detected, this step should be revisited.

2.4.3 Transducer Layer Printing

Transducer printing takes place after the printing of bottom electrode. Stencil is placed and aligned on bottom electrode and then it is taped to prevent any potential movement of it. Alternative to taping, water drops are sometimes utilized to provide cohesive force which provides strong enough attachment of substrate and stencil. After this alignment and placement, drop of piezo paste is placed near to stencil pattern as shown in the Figure 10 and it is squeegeed. It is observed that use of more piezo paint is better practice compared to use of less for each squeegeeing cycle. The main reason behind of this situation is throughout the movement of metal squeegee to print piezo material, a portion of it sticks to metal squeegee which leads to surface defects. Unlikely to electrode printing, metal squeegee needs to be held 30° and it needs to be moved at normal arm movement speed to fill the patterns on stencil since it is high viscous material. After the completion of printing process, it is good practice to visually examine surface of the transducer to see defects on the surface which can potentially cause short connection between top and bottom electrodes. It is also noted that visual inspection is not enough by itself since short circuit situation can also happen even without any visual anomalies. If there are no visual surface defects, the transducer can be placed on hot plate of 120°C for 15 minutes and DC voltage supply is connected to device. The calculation of poling voltage

levels and duration of poling is explained below. It is observed that step voltage increments are best practice to achieve desired poling electric field level because sudden voltage level changes cause more electric breakdown compared to step increments. The utilized method in the scope of this work is increasing electric field 5% or 0.25kV/mm at each step and waiting couple of seconds at this level until desired voltage level is obtained. After poling device on hot plate for 10 minutes, the transducer is removed from hot plate to cool down to room temperature while external electric field is still applied for 5 more minutes. The main reason behind starting the poling process on hot plate and completing it at room temperature is to achieve better alignment level at saturation with high temperature level and then cooling down it to room temperature in order to limit potential relaxation of domain walls. As explained in the poling process section, higher temperature leads to more energy where domain walls can move faster, high temperature poling part utilizes it to align better, and room temperature poling part again utilizes it to limit relaxation movements to end up higher remnant polarization. If visual surface defects are observed, the piezo paint layer can be cleaned prior to dry step with the help of IPO and transducer printing section can be revisited from the beginning.

After the completion of piezo layer printing, electrode printing section needs to be completed one more time to print top electrode on top of piezoelectric layer. Figure 10 demonstrates final transducer formation with bottom, top electrodes, and transducer layer on top of polyimide substrate with glass backing layer. At this stage it is good practice to check potential short connection between top and bottom electrode with the help of multimeter connectivity feature, if there is no short connection issue, can be moved to next step. Otherwise, electrode printing and transducer printing steps needs to be revisited.

2.4.4 SMA Connection Wiring

Male SMA connectors are placed on the edge of glass part of substrate. The location of SMA connectors can matter depending on the experiment type, for pulse-echo and hydrophone measurements, it is observed that placing SMA connector to short edge of glass substrate provide more lateral movement flexibility inside of the FC-70 tank where those experiments take place. After the determination of the location, the Gel 3095 epoxy is applied, SMA connector is placed and cured with UV light for roughly 15-20 seconds. After attaching SMA connector to substrate, bottom and top electrodes are connected to ports of SMA with the silver ink. Then, it is placed on hot plate to dry applied silver ink as explained in the electrode printing sub-section. Figure 10 demonstrates final version of transducer with SMA connections.

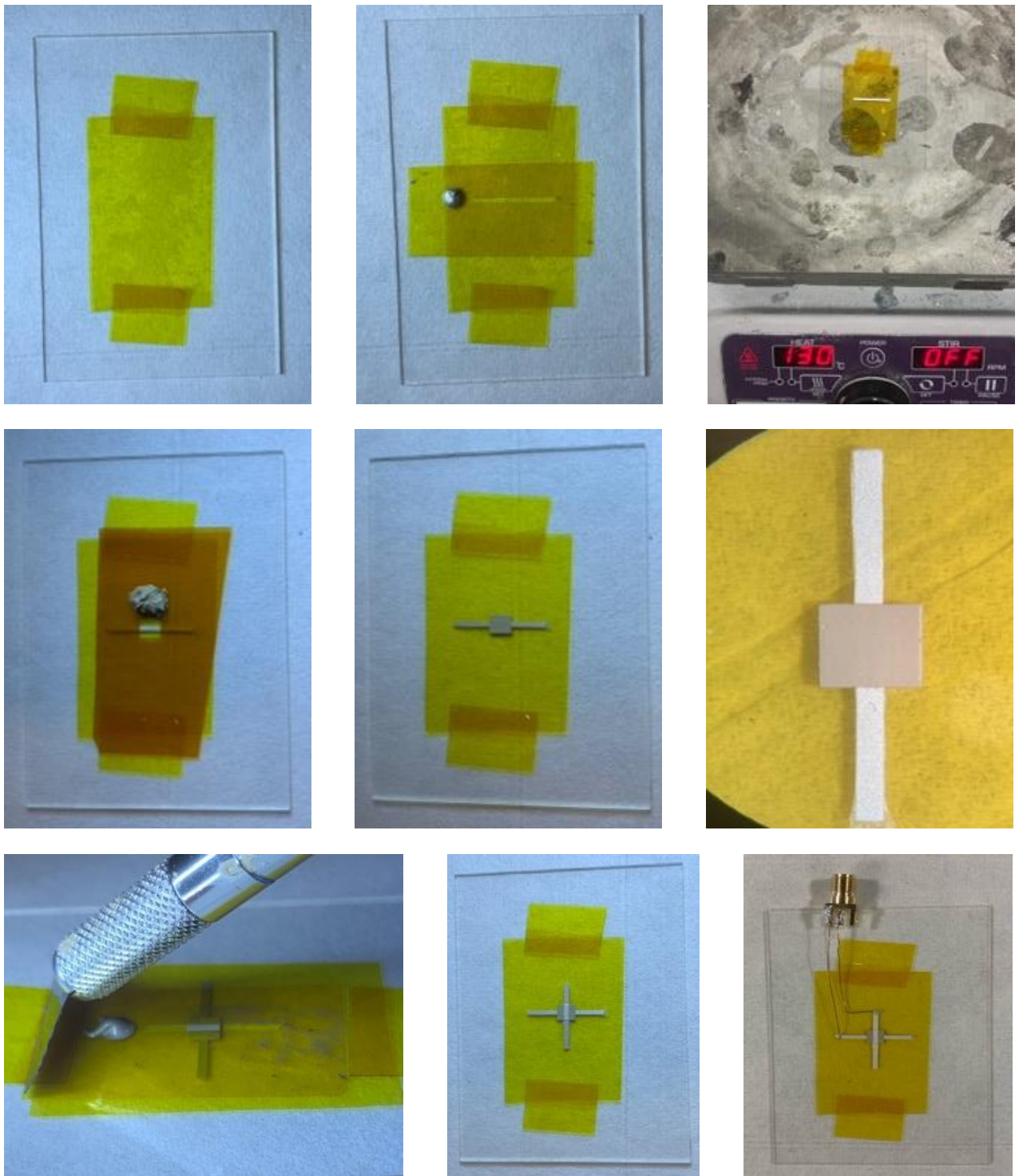


Figure 10 Transducer fabrication process: Illustration of each required step.

2.4.5 Transducer Poling

As explained in the poling process requirement section, three main parameters to consider for poling process are electric field, temperature and duration. In the literature it is shown that different electric field levels and durations at different temperature levels are utilized to pole devices. Kang reported that [57] 4 kV/mm electric field for 10 minutes is enough to pole PNN-PZT based piezoelectric paint at room temperature, Li et al. demonstrated that [58] 6.5 kV/mm for 60 minutes can pole PZT-5A based piezocomposite at 70°C, Egusa et al. reported [55] 29.2 kV/mm for 5 minutes at room temperature to pole PZT ceramic powder and epoxy resin combination of piezocomposite. It can be stated that there is no one stand all formulation of the determination of these parameters, the optimization step is necessary to find poling parameters specific to used transducer material. Furthermore, in the scope of this research, several experiments are taken place for determination of these parameters.

To determine optimum electric field level, the dielectric breakdown voltage needs to be considered as upper limit since higher applied voltage yields to better alignment of domains as explained previously. It is observed that dielectric breakdown is more commonly happens when electric field level starts exceeding 6 kV/mm. However, the limited control over surface roughness of the piezo layer causes to additional safety margin to achieve higher yield rates with good performance parameters. Optimum electric field level is chosen as 5 kV/mm considering both performance parameters and high yield rate expectations which will be examined in detail.

To determine the duration of poling process, it is important to examine minimum required time which is summation of nucleation time and domain wall time. In the characterization measurements, it is observed that minimum of 10 minutes of poling duration is required to have to observe good acoustic performance. After this point, the duration of poling has minimal effect on the device performance as demonstrated in the characterization chapter. For that, optimum level is chosen as 10 minutes for on hot plate and 5 more minutes at room temperature poling which yields to total of 15 minutes of poling process.

To determine poling temperature, it is important to consider the Curie temperature, other materials that are used to produce transducer and the effect of temperature on poling process. As explained previously, the Curie temperature is phase transition temperature level that where remnant polarization of piezoelectric materials is lost, and domains are randomly distributed due to temperature. The stated Curie temperature of PiezoPaint™ is 330°C where even at temperatures close to this level, high relaxation occurs so it is important to keep poling temperature level below Curie temperature. The poling temperature also effects substrate material and bottom electrode which is silver ink in this case. The bubble formation is observed in the silver ink when the temperature is raised to 160°C as shown in the Figure 11. The solvent evaporation of within the silver ink is main reason behind these formations. Due to uneven surface profiles after these formations, dielectric breakdowns more commonly happen even at slightly lower electric fields than found optimum electric field level. For that this temperature level is also considered for the determination of poling temperature. In addition to these, it is also explained that higher temperature leads to better alignment of domain walls so better remnant polarization. In

the light of these findings, the poling temperature is chosen as 120°C which is high enough to lead better alignment but not high enough to cause bubble formations.

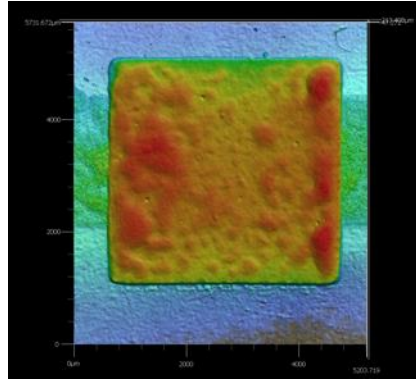


Figure 11 The effect on bubble formation on surface roughness due to high temperature processing.

The measurement of piezo layer thickness is necessary to calculate required DC voltage level to be applied given the optimum level for the electric field of poling process is known. For this step, three different methods are utilized including two direct and one indirect method. Direct methods are Keyence VK-X3000 3D (Keyence Corp., USA) surface profiler and height gauge, and indirect method is measurement of transducer capacitance and the calculation of thickness given all parameters are known other than thickness as the formula is given below where t is thickness level, ϵ is dielectric permittivity of piezoelectric material, A is active transducer area and C is measured capacitance.

$$t = \epsilon * A / C \quad (12)$$

Since it is important to examine surface profile at different points to determine poling voltage level accordingly, Keyence surface profilometer most commonly utilized method for thickness measurements. It can provide up to 0.01 nm resolution with ability

of scanning 50 x 50 mm² area which provides information regarding the highest and lowest peaks on the surface so that poling voltage can be determined accordingly to prevent potential dielectric breakdown. It is observed that thickness measurements with capacitance measurement method provides results that match with 95% accuracy to actual 3D surface measurements. Since it does not provide any information about surface roughness but only thickness, it is utilized for DC voltage calculation applications where only thickness measurement is required.

CHAPTER 3. CHARACTERIZATION AND TESTING OF PIEZOELECTRIC TRANSDUCERS

The characterization of materials is an essential aspect of any material science research, as it allows for a better understanding and quantification of the material's properties, which are critical for its optimal use and application. In this thesis, the focus is on the characterization of a commercially available piezocomposite material, PiezoPaint™ which is used as a transducer material. To develop a fabrication process and optimize the material's performance parameters for specific use cases, it is crucial to characterize its performance parameters, such as charge constant, dielectric constant, as well as its mechanical limits. This chapter presents an in-depth analysis of various measurements conducted under different external conditions with different transducers to characterize the PiezoPaint™ material's performance parameters. Specifically, this chapter examines impedance, hysteresis loop, acoustic, charge constant, XRD, surface roughness, and flexibility measurements to optimize the transducer performance of the PiezoPaint™ material for proposed use cases.

3.1 Electrical Input Impedance Measurements

In the literature one of the most extensively studied methods for determining the resonant frequency of piezoelectric transducers is through analyzing their impedance as a function of frequency [59, 60]. As discussed in previous chapters, piezoelectric materials in their natural state do not exhibit any piezoelectric characteristics due to the absence of a dipole structure in their crystal composition. Thus, a poling process is necessary to create

a dipole structure and enable the material's use as a transducer. To understand the effect of poling process parameters such as electric field, poling duration, and temperature, impedance measurements are compared, and depending on results, process parameters are optimized. Subsequently, the relationship between acoustic performance and transducer impedance measurements will be investigated in the following sections.

To conduct the measurements, transducers with active area of $2 \times 2 \text{ mm}^2$ and varying thicknesses are produced on glass substrates. A master Microsoft Excel spreadsheet is used to document the properties of each device, including its device number, fabrication date, transducer thickness, and the specific experiment performed on that device. Furthermore, the poling parameters for each device, such as poling voltage, temperature, and duration, are also recorded and included in the Excel spreadsheet, which can be found in the Appendix C. The labelled and fabricated devices are then subjected to different experimental conditions.

The Keysight P9370A (Keysight Inc., USA) network analyzer is used to obtain impedance measurements of the devices within a frequency range of 1-30 MHz. The real and imaginary components, as well as the phase of the impedance measurements, are recorded for each device for at each measurement point of different experiment and stored in a master Excel file. The data sets are then analyzed and compared using MATLAB.

3.2 Electromechanical Coupling Coefficient Measurement

The electromechanical coupling coefficient is a measure of the efficiency of converting mechanical energy into electrical energy. This is a crucial performance parameter since transducer applications rely on this conversion principle. The coupling

factor can be calculated by measuring the resonance and anti-resonance frequencies of piezoelectric materials, depending on the vibration mode. The most commonly reported coupling factors are k_p for radial mode and k_t for thickness mode vibration applications. In the literature, the effective coupling factor, k_{eff} , is frequently used to express the coupling factor of any arbitrary shape resonator at the resonance frequency or any overtone modes [61]. (13 expresses k_{eff} in terms of the resonance (f_r) and anti-resonance (f_a) frequencies.

$$k_{eff} = 1 - \left(\frac{f_r}{f_a}\right)^2 \quad (13)$$

In Figure 12, the resonance and anti-resonance frequencies of the same transducer are shown, with poled values of 2 kV/mm (red) and 5 kV/mm (black) external fields. It can be observed that the frequency difference between resonance and anti-resonance is less for the 2 kV/mm poling voltage compared to the 5 kV/mm voltage. By inserting the measured resonance and anti-resonance frequency values into Equation 13, the calculated electromechanical coupling coefficients were found to be 2.1% and 2.8% for the 2 kV/mm and 5 kV/mm poling voltages, respectively.

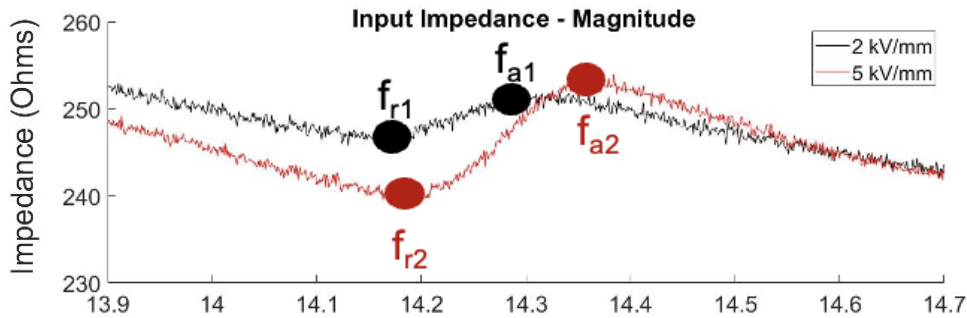


Figure 12 The resonance and anti-resonance frequencies of transducer under two different poling conditions.

3.3 Poling Process Optimization

3.3.1 Electric Field

To perform the poling electric field measurement, initial impedance measurements are taken prior to the poling process to establish a reference dataset. The devices are then subjected to incremental poling in steps of 1 kV/mm, and impedance measurements are taken using a network analyzer until the point of dielectric breakdown is reached. One of the primary objectives of the poling field experiments is to determine the dielectric breakdown voltage level of the devices to ensure that they can be safely poled without damaging the transducer. However, due to the manual fabrication process, the surface roughness of devices with similar thickness can vary, resulting in different dielectric breakdown voltage levels between them. In order to study this phenomenon, eight devices were exposed to progressively higher levels of voltage until they experienced breakdown. The thickness of each device and the corresponding voltage level at which it broke down are presented in Table 2. Electric field values were obtained by dividing the breakdown voltage by the thickness of the transducer. The average breakdown electric field was then calculated, which was found to be 6.2 kV/mm. These results suggest that dielectric breakdown is possible at an electric field level of 4.2 kV/mm, but it significantly increases at an electric field level of 6.2 kV/mm.

Table 2 - Electrical breakdown experiment result comparison between transducers with different thickness levels and their corresponding breakdown voltage levels.

Device #	Transducer Thickness (μm)	Breakdown Voltage Level (V)	Breakdown Electric Field (kV/mm)
D25	61	250	4.2
D26	79	450	5.6
D33	88	520	5.9
D35	75	550	7.3
D36	65	500	7.7
D40	83	550	6.9
D43-B	62	250	4.2
D43-M	75	510	6.8
Average			6.2

The standard deviation of the breakdown voltage was calculated using MATLAB, yielding a value of 1.2 kV/mm. This can be attributed to the manual fabrication process, which results in variations in surface roughness among the devices. As a result, some areas of the surface experience higher electric fields than others, leading to breakdown of the transducer. The surface roughness of the devices will be investigated further in subsequent sections. To ensure a high operational yield rate, the poling electric field was set at 5 kV/mm, which is one standard deviation below the average breakdown electric field of 6.2 kV/mm with a standard deviation of 1.2 kV/mm.

To investigate the poling electric field value of 5 kV/mm, a single device was subjected to increasing levels of electric field. The process began at 3.1 kV/mm and the electric field was increased by 0.6 kV/mm after each poling and measurement cycle. The results of these measurements are presented in Figure 13. As shown in the figure, the input impedance increases as the poling electric field increases, until breakdown occurs. Consistent with the predetermined value, the device experienced a slight pop shortly after

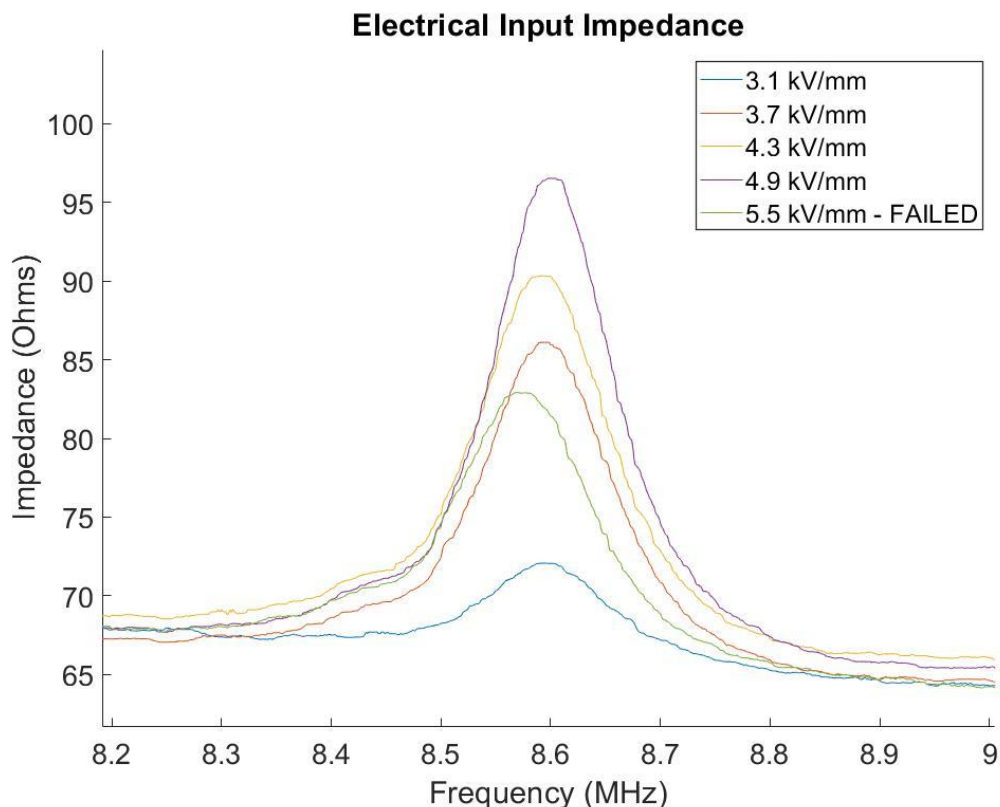


Figure 13 Electrical input impedance comparison under varied external electric fields.

exceeding the poling field limit of 5 kV/mm. This led to the conclusion that 5 kV/mm is a dependable limit for the poling electric field.

A breakdown event can lead to one of two possible outcomes. The first is a short circuit between the bottom and top electrodes, rendering the device inoperable. The second outcome is that the device remains functional, but the active area is significantly reduced due to the breakdown area. Figure 14 illustrates these two outcomes in two separate devices. In either scenario, both devices are deemed unreliable and cannot be utilized further.

In conclusion poling field examination, the experimental results have shown that an increasing poling electric field results in an increase in the electrical impedance value at resonance frequencies. However, it is crucial to establish a maximum poling voltage limit to avoid the possibility of transducer breakdown. For the PiezoPaint™ material with a 2x2 mm² active area, the experiments have indicated that the optimum poling electric field value is 5 kV/mm.

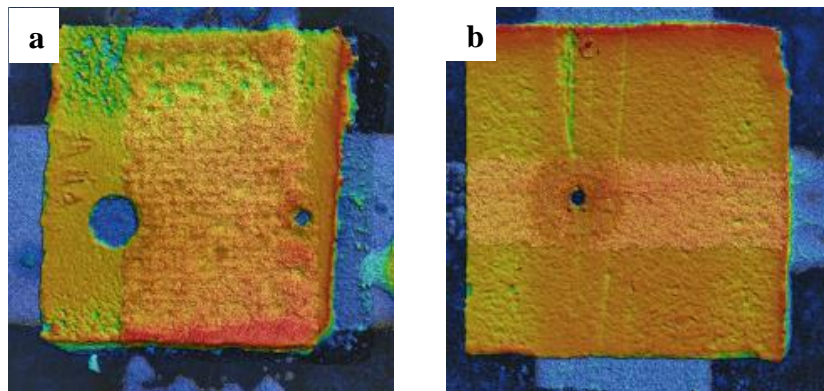


Figure 14 Visual demonstration of surface damages from dielectric breakdown: a) short device and b) functional device.

3.3.2 Duration

After determining the optimal poling electric field, a new set of experiments were conducted to examine the ideal duration for the poling process. The device was first subjected to an initial impedance measurement, after which it was exposed to an electric field of 5 kV/mm for a duration of 1 to 10 minutes, with increments of 1 minute. The results of these measurements are presented in Figure 15.

The measurement results indicate that the real part of the electrical input impedance does not vary significantly up to 5 minutes of poling duration. However, there is a notable increase observed at 6 minutes of poling duration compared to 5 minutes. Similarly, there

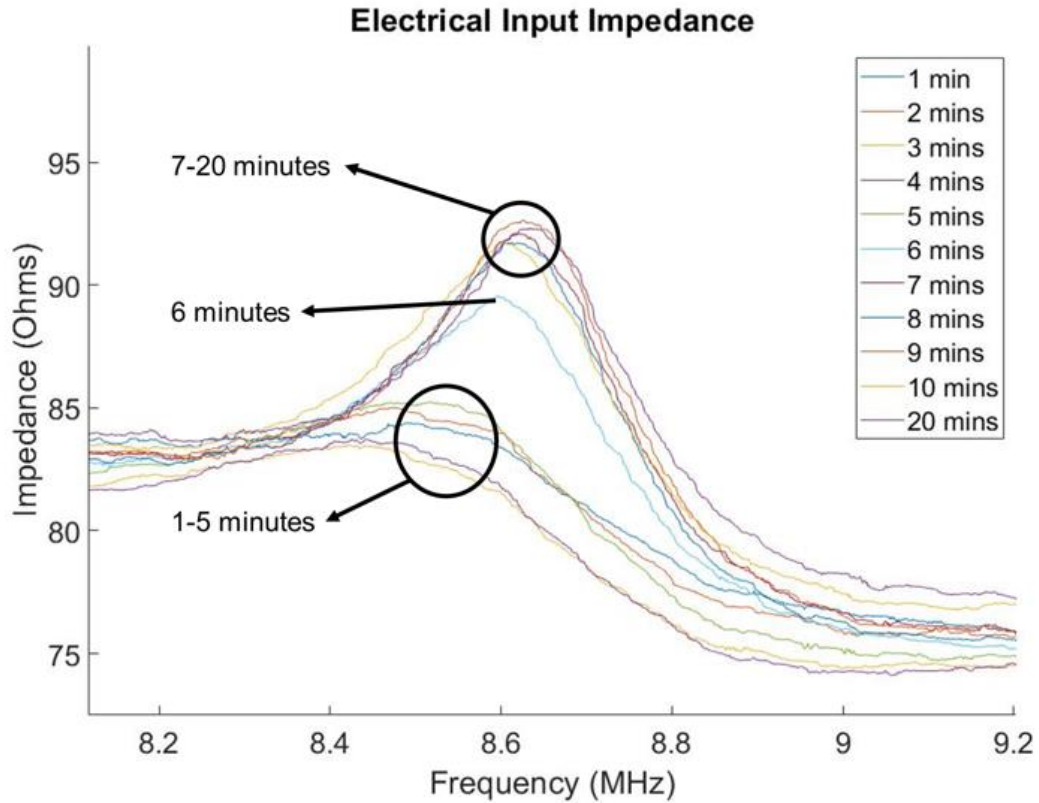


Figure 15 Comparison of electrical input impedance under varied poling times (1-10 minutes).

is also a significant increase in the impedance value observed between 6 and 7 minutes of poling. However, after 7 minutes of poling, there appears to be no significant change in the impedance value. This experiment is repeated with other device, and it is observed that at least 7 minutes is required to achieve saturation point for domain walls. As there are no operational safety concerns as breakdown of the device associated with longer poling durations, and the only drawback is time consumption, a duration of 10 minutes was selected for simplicity in time tracking and ensuring that the saturation point was reached.

To further investigate the effect of longer duration times, a similar experiment was conducted using poling durations of 10, 20, and 60 minutes on another device. The results of the electrical input impedance measurements are presented in Figure 16. No significant

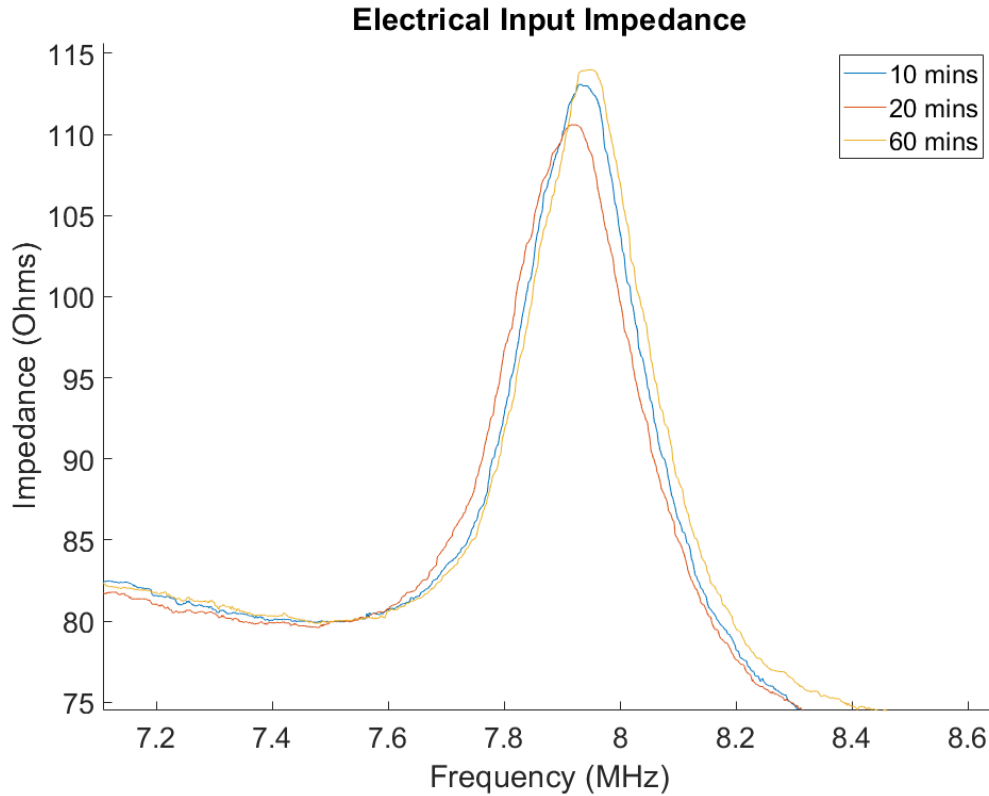


Figure 16 Comparison of electrical input impedance under varied poling times (10-60 minutes).

changes were observed in the impedance values beyond the 10-minute mark, up to the maximum poling duration of 60 minutes. Based on the results of both experiments, it can be concluded that there is no significant change in the impedance beyond the 10-minute mark and thus it is established as the minimum required duration for the poling process.

3.4 Hysteresis Loop Measurements

Piezoelectric materials have a unique crystal structure that is non-symmetrical, and within this sub-category of materials lies the class of ferroelectric materials. When an external electric field is applied to these materials, their crystal structure undergoes a microscopic orientation change, which results in the creation of a dipole structure as

previously explained. The formation of this dipole structure is responsible for the development of a remanent polarization, which is the characteristic of the material to exhibit dipole behavior without any external electric field. The creation of these dipoles is essential for the proper functioning of devices that utilize ferroelectric materials. To achieve this, it is important to accurately characterize the polarization of these materials through hysteresis loop measurements [18]. This section will focus on the setup and results of hysteresis loop measurements.

The macroscopic polarization of ferroelectric materials that remains after the poling field has been removed is referred to as remnant polarization. Unlike other types of piezoelectric materials, the orientation of the polarization in ferroelectric materials can be set and reversed by applying an external electric field to remove the domain walls. This process results in a hysteresis phenomenon where the necessary external field to move the domain walls depends on their current orientation. As a result, the required external electric field to remove the domain walls varies depending on their current orientation, as demonstrated in Figure 17.

When an external electric field is applied to ferroelectric materials, it removes domain walls in the direction of the field. The initial application of the electric field is demonstrated by the AB segment on the graph. Once the polarization reaches the saturation point B, it indicates that all domains are aligned with the orientation of the external field. This point is called saturation polarization or P_s .

As the external electric field is slowly decreased to zero, the B- P_r movement on the graph is observed, where some of the domain walls experience relaxation. However, a non-

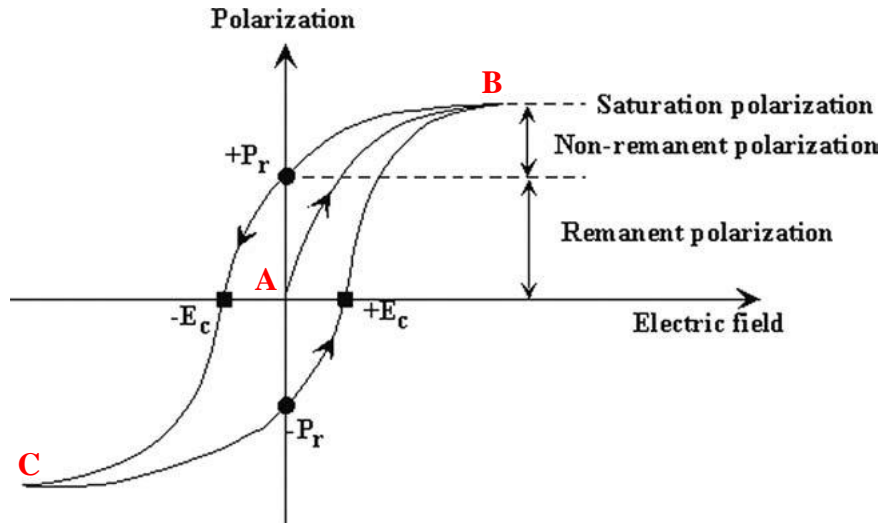


Figure 17 Hysteresis curve of ferroelectric material demonstrating P_r , E_c and P_s [62].

zero polarization of P_r is still observed due to the remaining domain walls, and this is known as remanent polarization. To switch all domain walls and achieve zero polarization, a reverse electric field must be applied. The electric field required to reach zero polarization is referred to as the coercive field, E_c .

Further increasing the electric field in the negative direction removes domain walls to other orientations, and negative saturation point C can be reached. This cycle can be completed by increasing the electric field in the positive direction. Symmetry is expected in an ideal hysteresis loop where the values of negative and positive remanent polarization and coercive field are the same. However, hysteresis loops can also be used to examine the non-ideal behaviour of materials.

The most commonly used method for measuring hysteresis involves a technique developed by Sawyer and Tower [63], which they demonstrated using Rochelle salt. The method is based on the dielectric properties of ferroelectric materials and utilizes a basic voltage divider logic. When a ferroelectric material is bounded by two electrodes, it forms

a capacitor (C_s) due to its dielectric nature. To measure hysteresis, another capacitor is added in series with C_s as a reference capacitor, C_{ref} , which has a much larger capacitance value than C_s . Because the two capacitors are connected in series, they have the same amount of charge across their plates. According to Equation 14, which applies to two capacitors with equal charge, the capacitance with the higher value will have a lower voltage across it.

$$Q = C * V \quad (14)$$

To eliminate the voltage across the reference capacitor (C_{ref}), which has a capacitance value that is several orders of magnitude higher than C_s , the signal generator's applied signal is equal to the voltage across the plates of the ferroelectric material. Dividing this voltage value (V_{input}) by the sample's thickness (t), as illustrated in Equation 15, allows for the determination of the applied electric field (E).

$$E = V_{input}/t \quad (15)$$

To determine the polarization, the voltage (V_{output}) across the reference capacitor is measured. Multiplying this voltage level by the capacitance value yields the charge (Q) across the reference capacitor, which is equal to the charge across C_s . Dividing the amount of charge across C_s by its active area (A) yields the polarization (P), as illustrated in Equation 16.

$$P = Q/A \quad (16)$$

For this experiment, a signal generator (PicoScope 5444D, Pico Technology, UK) is utilized in combination with a high-gain amplifier (Model 2205, TREK Equipment Corp., USA) to achieve the desired AC voltage levels. A multi-channel digital oscilloscope is used to measure both the input and output voltage levels. The capacitance value of C_s is measured as 42 pF, and C_{ref} is chosen to be much larger than that as 1 μ F to minimize the voltage drop across it. The experimental setup is depicted in Figure 18.

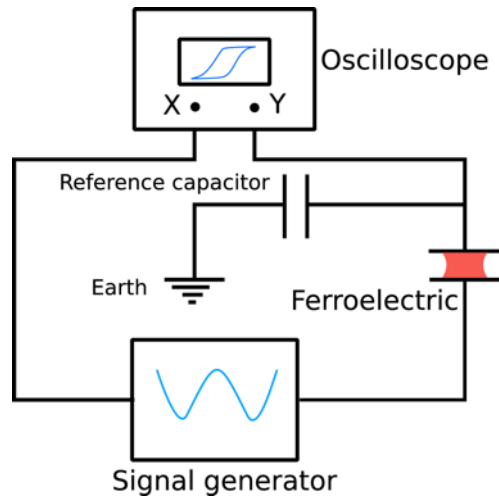


Figure 18 Sawyer Tower's electrical circuit schematic [64].

An input signal in the form of a triangle wave, with a V_{peak} of 350V (corresponding to 6.1 kV/mm), is applied at a frequency of 500 Hz. The voltage data captured during the experiment is stored and processed using the method described above. The results of the measurement are presented in Figure 19. The saturation polarization is found to be approximately 1.1 μ C/cm², while the coercive field is approximately 1.5 kV/mm. The remanent polarization is approximately 0.85 μ C/cm², and in literature typically reported values are in the range of 0.1 to 100 μ C/cm² [65].

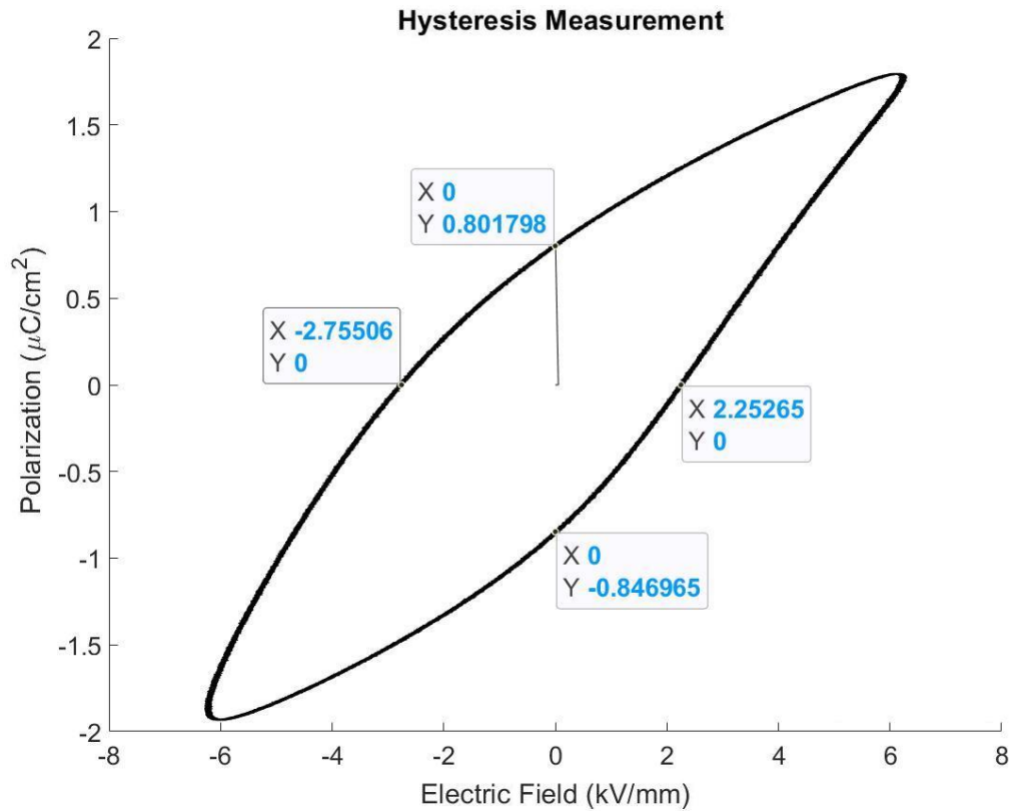


Figure 19 Hysteresis measurement of piezoelectric transducer with P_r and E_c points.

3.5 Piezoelectric Charge Constant Measurements

The charge constant, d , of piezoelectric materials is the electric charge generated on the electrodes when subjected to mechanical stress. This constant is typically measured in Coulombs per Newton (C/N) and is the most commonly used parameter for evaluating and comparing the performance of piezoelectric materials [66]. The notation for d includes two subscripts, which indicate the directions of the generated electric charge and the applied mechanical stress. For example, in the case of d_{31} , the first subscript of 3 denotes that the generated charges are in the direction of 3, while the second subscript of 1 denotes that the

applied stress is in the direction of 1. The polarization direction of the device always aligns with direction 3, with the other directions following it as illustrated in Figure 20.

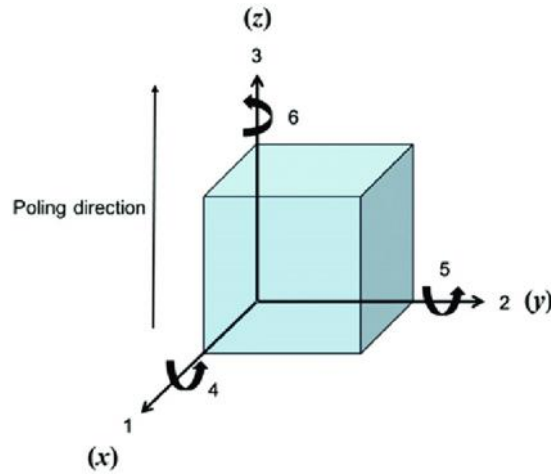


Figure 20 Direction index of performance constants for piezoelectric transducers [67].

In the literature there are three commonly used methods for measuring the piezoelectric charge constant [68-70]. The first two methods are direct measurement techniques known as the Berlincourt method and the laser interferometer method, while the third is an indirect method called the resonance-antiresonance method. This section provides a brief explanation of the working principles of these methods, including the required experimental setup, as well as the advantages of each method over the others.

3.5.1 Berlincourt Method

The Berlincourt method, which utilizes a quasi-static d_{33} meter, is a simple and highly accurate technique for measuring the piezoelectric charge constant. To perform the measurement, a small oscillating force is applied to the sample, and the resulting charge output is measured. This method is particularly effective for determining the charge constant in the direction of polarization. Commercial systems are available, or a basic

system can be constructed such as impact hammer as reported [70], as discussed in the following section. A diagram of a commercially available system is shown in Figure 21, with the bottom and top electrodes attached to d_{33} meter probes, allowing for measurement of the charge constant. However, this method has some limitations. Additional steps, such as establishing electrical connections on the side and using additional probes, are necessary to measure d_{31} , since the applied force and generated charge are in perpendicular directions. Additionally, it is not well-suited for thin film applications, where it is challenging to fabricate side electrodes for thin-film transducers.

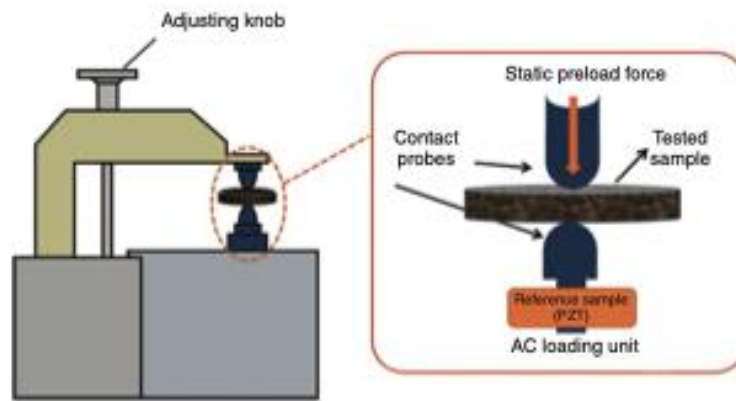


Figure 21 Berlincourt method: Schematic demonstration of components [71].

3.5.2 Laser Interferometry Method

The laser interferometry method for measuring the piezoelectric charge constant is based on the reverse piezoelectric effect. When an electric field is applied to the electrodes of a sample transducer, the transducer generates mechanical displacement in both the polarization direction d_{33} and the perpendicular direction d_{31} . Laser interferometry can capture both of these displacements. To obtain an accurate measurement, multiple sets of

measurements are taken to minimize external effects, such as surface roughness, and the average displacement per applied voltage is determined. Since there is no stress field on the transducer, the stress T can be set to zero in the constitutive piezoelectric equation. Furthermore, this equation can be simplified such that d_{33} is equal to strain S divided by electric field E , as shown in Equation 17. An experimental setup reported in the literature is shown in Figure 22.

$$d_{33} = S_3/E_3 \quad (17)$$

The main disadvantage of the laser interferometry method is its sensitivity to external effects such as vibration. However, it provides the advantage of measuring d_{31} for thin film applications without requiring additional steps.

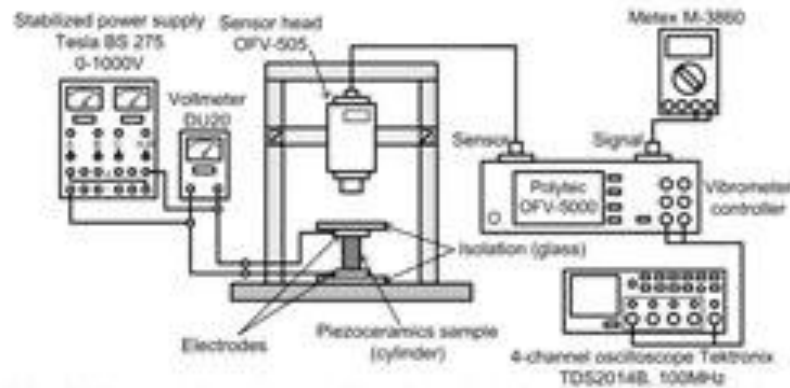


Figure 22 Laser interferometry measurement setup for piezoelectric charge constant measurement [66].

3.5.3 Resonance and Anti-resonance Method

The resonance and anti-resonance method differs from direct measurement methods in that it employs the circuit model equivalent of piezoelectric materials to determine resonance frequencies through impedance measurements, and then calculates

d_{33} using these frequency values. In the preceding chapter, the circuit model equivalent for piezoelectric materials was presented, which comprises two parts that are parallel to each other. One part contains only static capacitance, while the other part contains resistance, capacitance, and inductance in series. This model illustrates the dynamic characteristics of the material.

According to the literature [61], the derivation of d_{33} can be achieved by using Equation 18, which involves the resonance frequency f_r , anti-resonance frequency f_a , parallel resonance frequency f_p , free capacitance value of transducer C^T , active area of transducer a , thickness of transducer t and density of sample p . Once all of these values are inserted into the equation, the value of d_{33} can be determined without the need for any additional experiments. Although this method does not necessitate any additional specialized tools, its drawback is its heavy reliance on the precise measurement of resonance frequency and the accuracy of the equivalent circuit model.

$$d_{33} = k_{33}(\epsilon_{33}^T \cdot s_{33}^E)^{\frac{1}{2}} = \left(\epsilon_{33}^T \cdot s_{33}^D \cdot \frac{k_{33}^2}{1 - k_{33}^2} \right)^{\frac{1}{2}} \quad (18)$$

$$= \left(C^T \cdot \frac{t}{\frac{\pi \cdot d^2}{4}} \cdot \frac{1}{4 \cdot \rho \cdot f_p^2 \cdot t^2} \cdot \frac{\frac{\pi}{2} \cdot \frac{f_r}{f_a} \cdot \tan\left(\frac{\pi}{2} \cdot \frac{f_a - f_r}{f_a}\right)}{1 - \frac{\pi}{2} \cdot \frac{f_r}{f_a} \cdot \tan\left(\frac{\pi}{2} \cdot \frac{f_a - f_r}{f_a}\right)} \right)^{\frac{1}{2}}$$

3.5.4 Conducted Measurements

In the scope of this study, the commercially available transducer material, PiezoPaint™, was employed. The material's d_{33} coefficient is listed as 40 pC/N in the datasheet, which can be found in the Appendix A. To verify this value, two different

measurement setups were used, both of which utilized the quasi-static method. The first setup involved using a commercially available d_{33} meter (YE2730A, d_{33} meter) as depicted in Figure 23. To connect the bottom electrode of the transducer to the probe beneath the glass substrate, an aluminum foil with a crocodile clip was used. Using this method, the d_{33} value of the transducer was measured as 35 pC/N, which is consistent with the value reported in the datasheet.



Figure 23 Piezoelectric charge constant measurement setup with d_{33} meter.

As an alternative to using a d_{33} meter, a basic experimental setup was developed that can be used when such a meter is not available. This method requires the application of a constant, repeatable force to a surface using a prepared impact hammer mechanism, as shown in Figure 24.

The applied force is determined by measuring the impact of the rod on a weigh meter and multiplying that value by the force of gravity. After setting up the impact hammer, the transducer sample is placed beneath it, and its electrodes are connected to a digital oscilloscope to measure the voltage values generated under the applied force. By

multiplying the measured voltage value with the capacitance of the sample, the generated

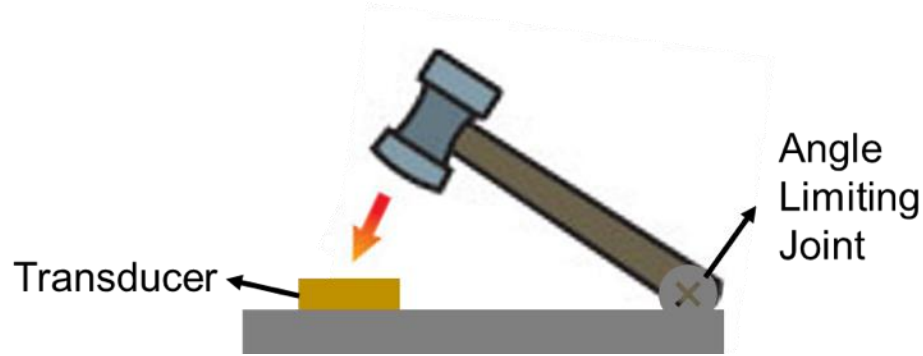


Figure 24 Prepared d_{33} measurement setup with impact hammer

charges can be calculated. Using Equation 1 the d_{33} value of the transducer can be determined, which in this case was 20 pC/N. While this method is applied as a preliminary method to obtain a sense of the material's d_{33} range, it requires improvement as the applied force depends on manual processing. Nevertheless, the simplicity of the setup provides an advantage in understanding the d_{33} range of the material.

3.6 XRD Measurements

X-ray diffraction (XRD) measurements are a commonly used method for developing piezoelectric materials to gain insights into their crystal structure, phase composition, crystallite size, strain, and defects [72]. In this study, an XRD measurement was conducted to gain a better understanding of the crystal structure of the material, and the results were found to overlap with the crystal structure of perovskite materials reported in the literature [73] as explained below.

Measurements are taken using the Panalytical Empyrean instrument from Malvern Panalytical. Careful selection of divergence slit, and mask sizes is crucial to ensure irradiation of the entire area without over-irradiation. For this study, the following settings

were chosen: 1/8 divergence slit, 2 mm mask, 0.02 soller slits, and 1/2 anti-scatter slit. The instrument is operated at 45 kV and 40 mA, and the resulting measurements are recorded. The data is plotted using MATLAB as demonstrated in Figure 25. Comparison of the XRD measurement results with literature [73] shows that the crystal structure is perovskite.

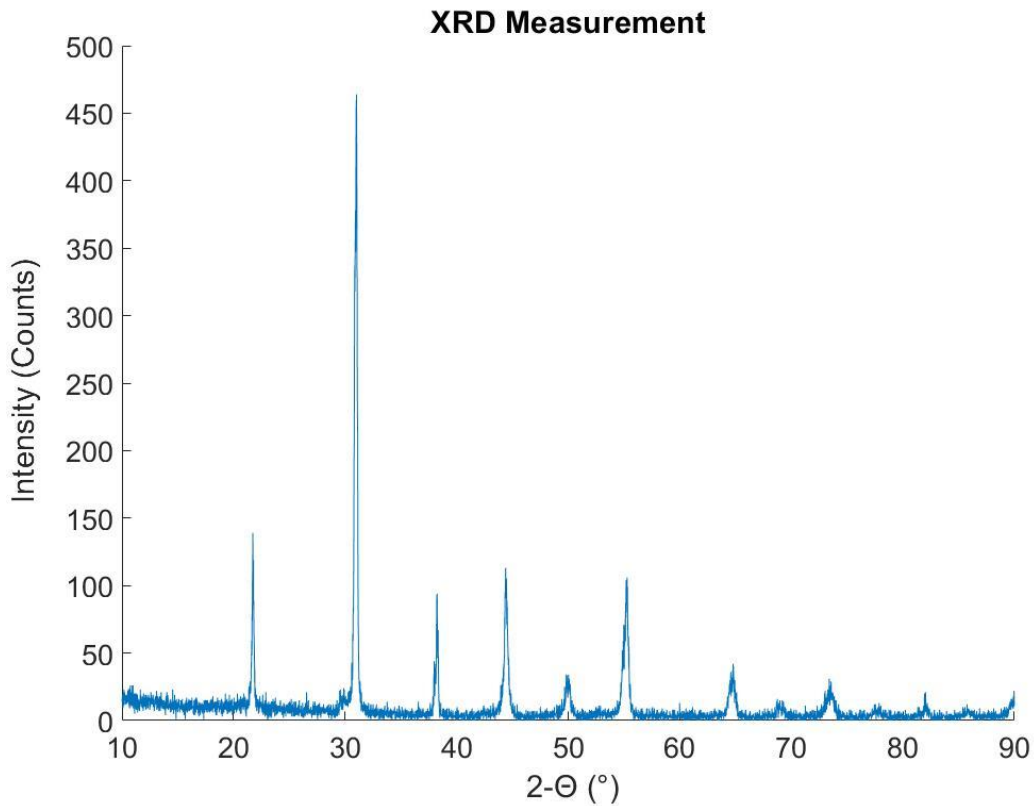


Figure 25 XRD measurement result of transducer between 10-90 $^{\circ}$.

3.7 Acoustic Measurements

3.7.1 Hydrophone

To assess the acoustic performance of transducers, hydrophone measurements are employed. The measurement setup consists of a hydrophone (HGL-0200, Onda Corp., USA) connected to a pre-amplifier (AG-2010, Onda Corp., USA), a pulser-receiver module (Panametrics, 5072PR), and a digital oscilloscope (PicoScope 5444D, Pico Technology,

UK). In these experiments, the transducers are located at a distance of approximately 1-5 mm from the hydrophone and are driven by the pulser-receiver module while submerged in FC-70. Both the transducers and hydrophone are connected to the oscilloscope using 50 Ohm coaxial cables, as measurement setup illustrated in Figure 26. The data collected by the digital oscilloscope is subsequently processed in MATLAB by performing a fast Fourier transform (FFT) on the captured data to determine the frequency response of the transducers.

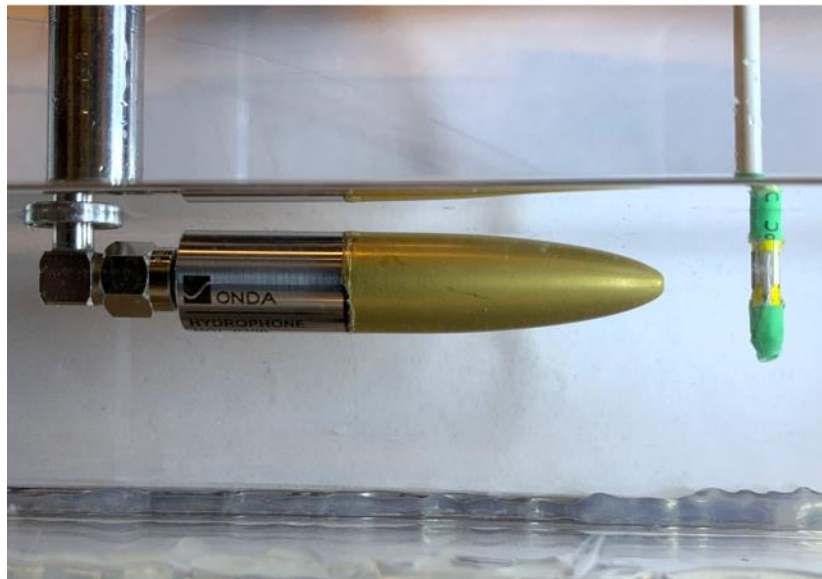


Figure 26 Acoustic measurement setup using a hydrophone.

The primary objective of these measurements is to characterize the ultrasonic actuation capabilities of the transducers. During the experimentation, several observations were made. Firstly, the correlation between the poling voltage and frequency response was established. As previously mentioned in the poling electric field section, it was anticipated that there would be a connection between the device's acoustic performance and the poling electric field. The following results, Figure 27, illustrate the comparison of the frequency

response of the transducer around its resonant frequency after being poled with various electric fields.

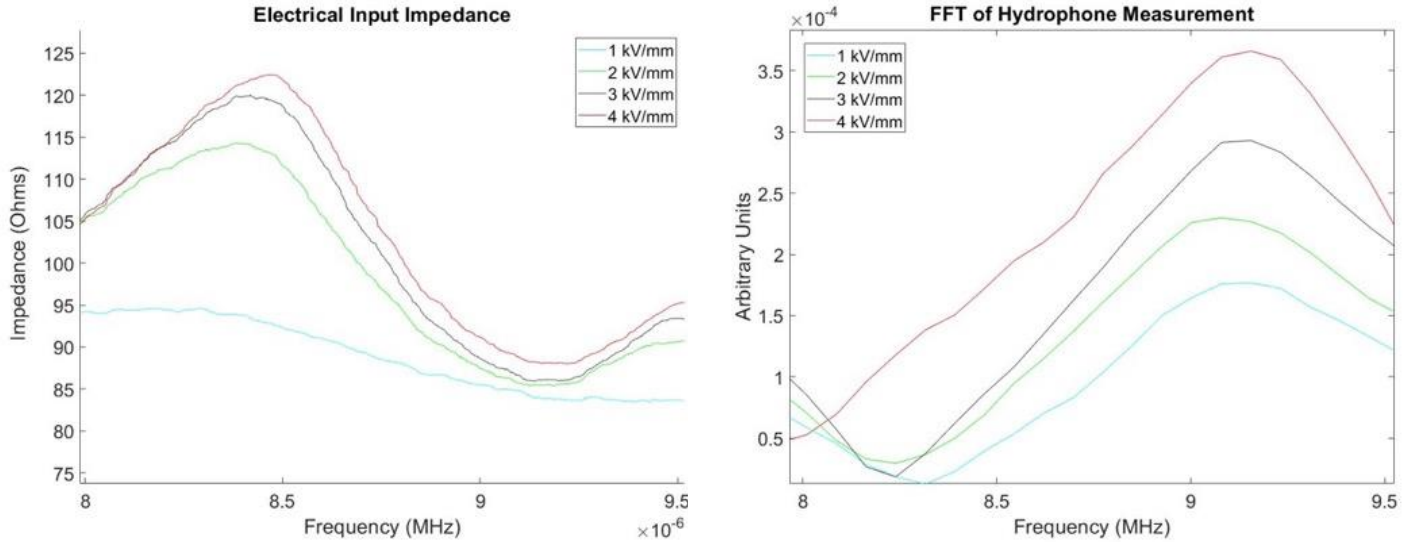


Figure 27 Electrical input impedance and hydrophone measurement comparison under different applied voltages for same transducer.

The second observation pertains to the substrate ringing effect observed between different substrate materials. In this study, two distinct substrate materials were utilized, namely polyimide and glass. The frequency response of the transducer on the glass substrate indicated a ringing effect due to the higher quality factor of glass. The glass substrate reflects the incoming acoustic waves back and forth, which results in a visible ringing effect, as shown Figure 28. Conversely, polyimide has a smaller quality factor and therefore reflects acoustic waves to a lesser extent than its glass counterpart. As a result, no ringing effect was observed for the devices fabricated on polyimide substrates, as depicted in Figure 28.

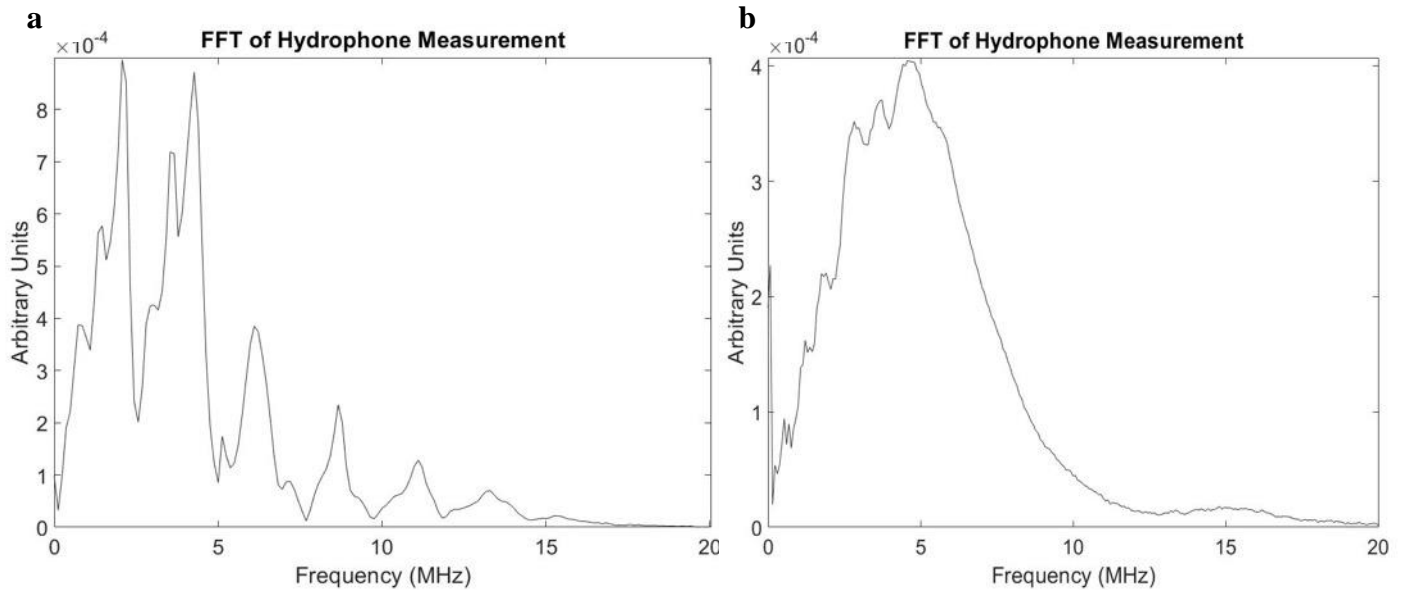


Figure 28 Comparison of hydrophone measurement results between two devices a) on glass substrate and b) on polyimide substrate.

3.7.2 Pulse-Echo

Piezoelectric transducers are commonly used for both sensing and actuating in ultrasound imaging applications such as imaging or ranging. Pulse-echo measurements are often employed to characterize both of these abilities, as a single element can be used to generate the pulse and receive the echo from a reflector. The measurement setup for pulse-echo measurements is similar to that for hydrophone measurements, except that a steel reflector is used instead of a hydrophone. The measurement setup for pulse-echo measurements is shown in Figure 29.

Pulse-echo measurements rely on the time delay between transmitted and received signals as well as the velocity of sound in the medium to calculate the distance between the transducer and the reflection point. The strength of the reflected sound waves is affected by the mismatch between the acoustic impedance of the two adjacent mediums. Acoustic



Figure 29 Measurement setup for pulse-echo measurement with steel reflector.

impedance is defined in the literature as the resistance of a medium to longitudinal wave motion. In ultrasound applications, minimizing reflection is crucial and requires matching the acoustic impedance of the two mediums where sound waves propagate. This is why ultrasound gel is applied before imaging in clinical applications.

A transducer having an active area of 4 mm^2 and a thickness of $60 \text{ }\mu\text{m}$ is positioned at a distance of 1 mm from a steel reflector for pulse-echo measurement. Using a receive gain of 30 dB , measurements are taken, and the captured data is plotted in MATLAB, as shown in Figure 30. Based on these results, the transducer is suitable for imaging and ranging applications that require successful echo signal reception. Additional analysis of the transducer's acoustic performance through pulse-echo measurement will be explored in the application chapter.

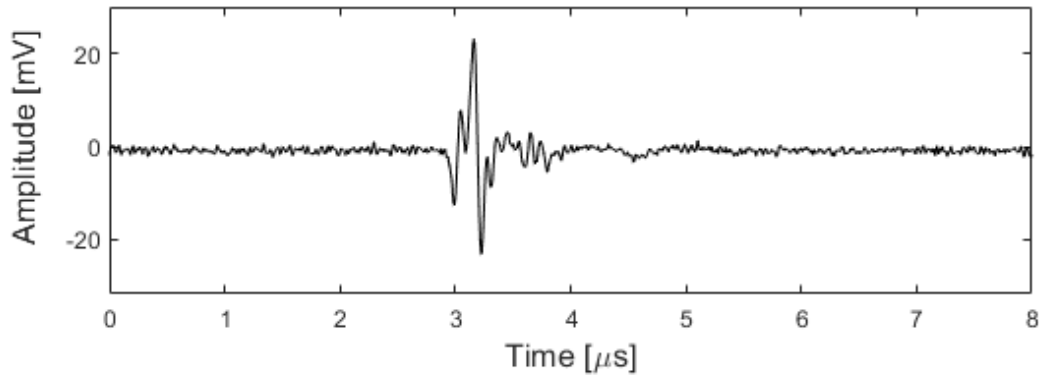


Figure 30 Acoustic echo measurement result from a steel reflector.

3.8 Transducer Simulations by KLM Model

Simulations offer the advantage of analyzing the impact of various parameters, such as active area, element thickness, or backing layers, on transducer performance, in addition to measurements. To achieve this, it is crucial to simulate transducer responses effectively and compare them with actual measurements. The previous chapters discussed various piezoelectric circuit equivalent models, while this section focuses on the KLM mode simulation method, which is a widely used approach in the literature [74] for simulating ultrasonic transducers based on piezoelectric elements.

The MATLAB software was used to create a simulation tool by Gokhan Percin. Figure 31 illustrates the simulation mode, where all performance parameters for each layer must be entered into the tool. The back media and front media represent the medium where measurements are taken. In this study, most of the electrical impedance measurements were taken in the air and thus, it was entered as both the back and front layers for those measurements. Additionally, acoustic measurements, such as hydrophone and pulse-echo,

were taken in FC-70. To simulate these measurements, both the back and front layers were entered with FC-70 acoustic parameters.

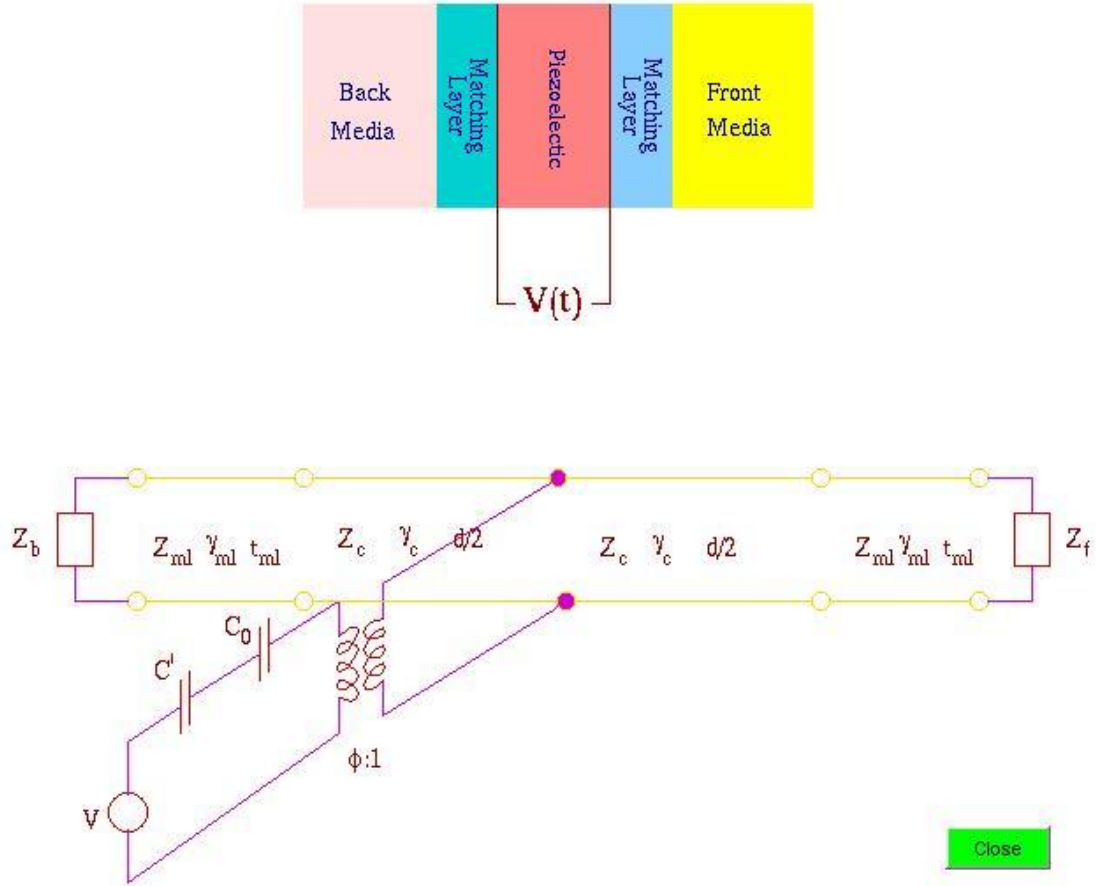


Figure 31 Schematic illustration of circuit model employed in KLM-based simulation tool.

The matching layer between the back media and piezoelectric layer generally consists of silver ink as the bottom electrode, polyimide thin film, and a glass substrate. Although silver ink is always used as the bottom electrode, one of the backing layers, depending on the application, is selected between glass or polyimide thin film or both, and entered accordingly. For the matching layer near the front media, silver ink is used as the top electrode and is entered as one of the matching layers. Additionally, to observe the potential effect of the outer cover layer, which will be examined in the application chapter,

a polyimide thin film is also included in some simulations. After obtaining the necessary measurements, the active area and thickness of the transducer elements, the piezoelectric parameters of PiezoPaint™ are entered as the transducer layer. All the essential simulation parameters for each layer are provided in the Appendix D.

This section presents the first two simulation results, which are compared and validated against actual measurement results on both glass and polyimide thin film substrates. Following the demonstration of model validity and analysis of results, a new set of simulations is conducted to examine the impact of the medium in which measurements take place, the effect of the outer cover layer, and the effect of transducer thickness. The measurement inputs, results, and analysis are presented below in sequence.

Transducer on Glass Substrate Simulation

In this measurement, air is selected as the back and front media. For the back matching layer, a glass substrate with a thickness of 1 mm and silver ink with a thickness of 10 μm are entered. The piezo layer has an active area of 4 mm^2 and a thickness of 60 μm . The front matching layer is composed of 10 μm silver ink. As previously mentioned, the required characteristic parameters for each layer are provided in the Appendix D.

The results depicted in Figure 32 indicate a strong alignment between the measurement and simulation results. Additionally, based on these findings, it can be concluded that this model is suitable for simulation purposes within the scope of this study, as it produces results that closely match actual measurements.

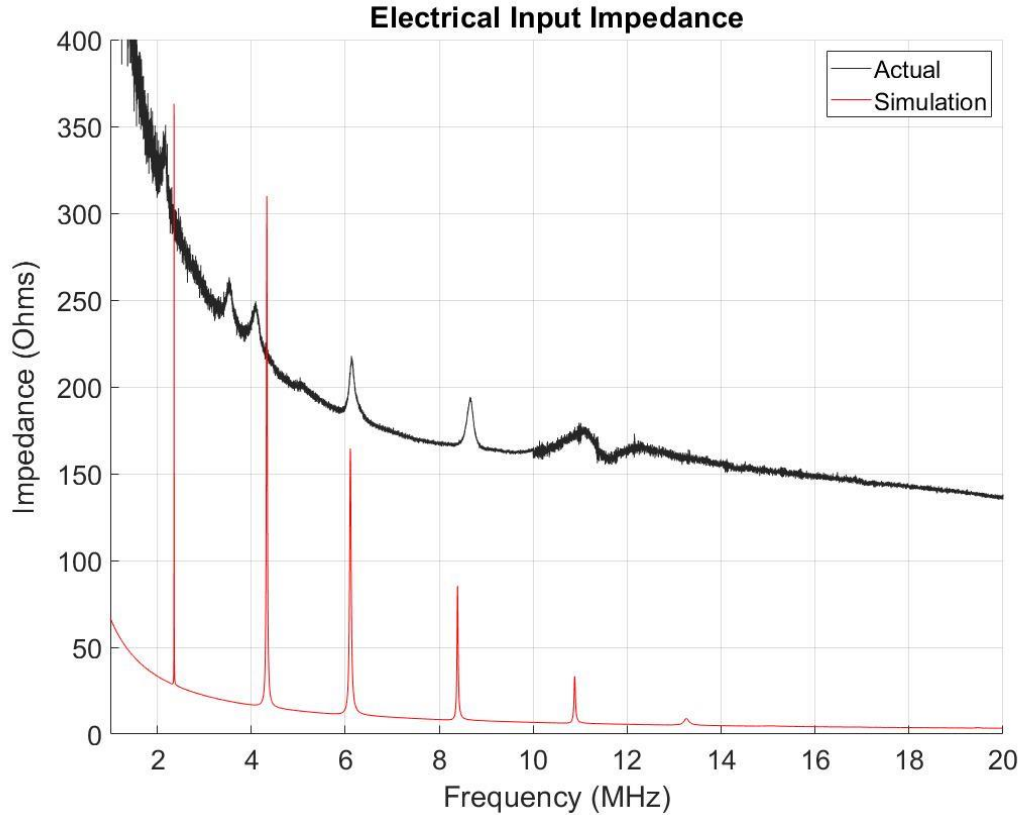


Figure 32 On-glass device: actual vs. simulated electrical input impedance measurement comparison.

Upon examining the measurement results, it was observed that substrate ringing had occurred. This phenomenon can be attributed to several factors, including the material properties of the substrate, as well as the substrate's thickness and shape. In this case, the glass substrate's high acoustic impedance caused it to reflect the majority of incoming sound waves, resulting in consistent intervals of 2-2.4 MHz between each peak. This regularity supports the notion of substrate ringing. By taking into account the thickness of the glass substrate (1 mm) and the acoustic velocity of sound waves in glass between 4000-5000 m/s, it was possible to calculate the required time between each peak as 2.2 MHz, which corresponds with the observed results.

Transducer on Polyimide Substrate Simulation

To further validate the simulation tool and investigate the substrate ringing effect, the same simulation was conducted on a similar device with a polyimide substrate instead of glass. The simulation input included a substrate thickness of 50 μm , an active area of $2 \times 2 \text{ mm}^2$, and a transducer thickness of 70 μm . The resulting measurement and simulation data are presented in Figure 33.

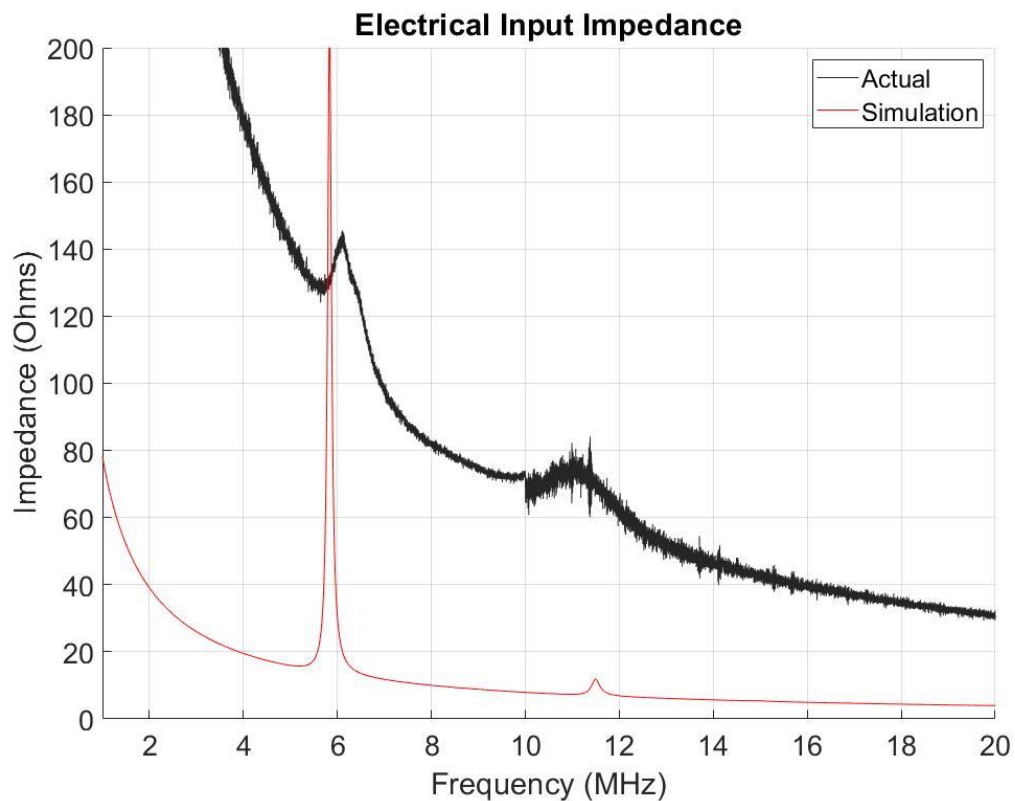


Figure 33 On-polyimide device: comparison between actual and simulated electrical input impedance measurement.

As expected, the simulation and measurement results are closely matched with negligible differences. Unlike the glass substrate, the polyimide substrate did not exhibit

any ringing effect. This is because the acoustic impedance value of polyimide is significantly lower than that of glass, making it less reflective to incoming sound waves.

Outer Layer Implementation Simulation

In the upcoming application chapter, it will be investigated whether these devices can be utilized in a sleeve structure that can be implemented in catheters of various diameters. In order to achieve this configuration, an outer layer must be applied onto the transducer surface. To evaluate the effect of this layer, the previously analyzed device parameters using a polyimide substrate were employed to create a simulation model, which was used to simulate polyimide thin films with varying thicknesses. The simulation results are presented in Figure 34.

As anticipated, utilizing a polyimide thin film with a thickness of 12.5 μm as the outer layer did not significantly alter the device's acoustic performance. However, selecting a thicker layer, beyond 50 μm , will cause reflections that could negatively impact the transducer performance, as illustrated in the Figure 34.

In conclusion, the KLM model simulation tool produced results that are in close agreement with the actual measurement data, which is a significant achievement. This capability allows for the determination and optimization of various parameters to meet specific application requirements and enable the fabrication of transducers accordingly. Furthermore, the study examined the substrate ringing effect on glass substrate and investigated the impact of applying an outer layer on device performance through simulations, revealing the limitations of this process.

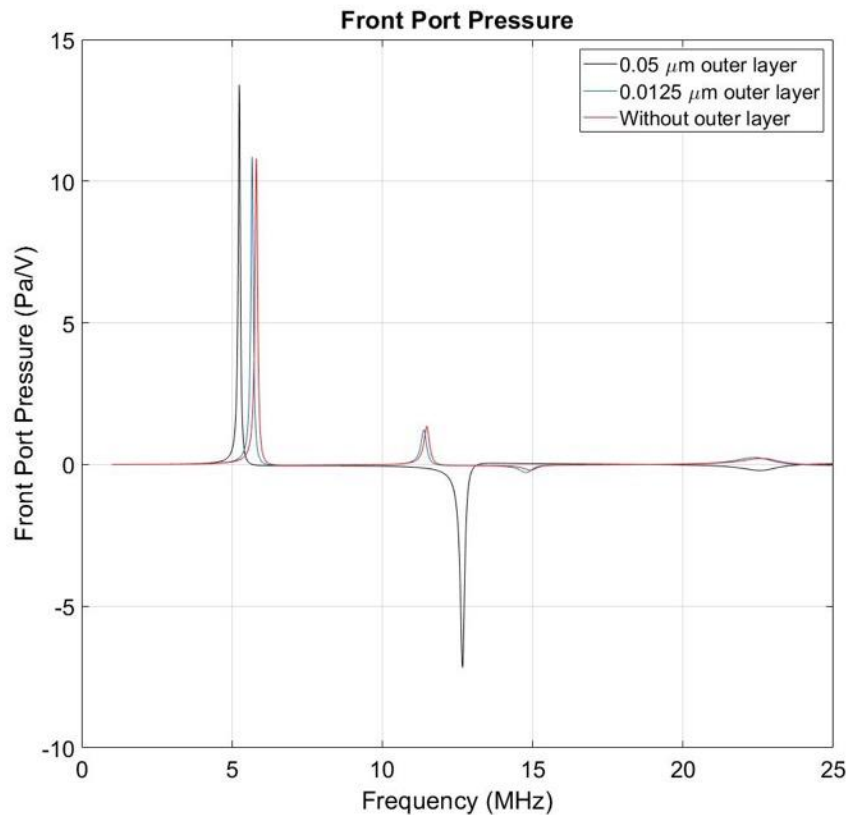


Figure 34 Simulation results of the effect of different thickness outer layer implementation.

3.9 Surface Roughness Measurements

The fabrication section of this study describes the use of stencil and screen printing methods for the piezo-layer fabrication process. These manual methods involve squeegeeing with a tool and do not require any specialized equipment. While the literature includes reports on both manual [75] and automated processes that use specialized tools [76], this study focuses on the manual methods. Due to the manual nature of the process, it is crucial to compare the effects of different factors, such as the angle of attack, the squeegee material used, and the squeegeeing speed, to achieve an optimal surface profile.

In this chapter, the impact of various process steps and printing methods on the surface roughness of the fabricated devices is examined.

For the measurement of surface roughness, a VK-X3000 3D (Keyence Corp., USA) surface profilometer was used. This device is capable of non-contact measurement of surface profile, roughness, and thickness with a resolution of sub-micron levels. The obtained data is then analyzed using dedicated software for surface profile analysis. The devices that will be used for profile measurements have a surface area of $4 \times 4 \text{ mm}^2$ and are manufactured on glass substrates with stencil printing fabrication method.

Several comparison parameters are selected to compare the surface profiles, namely the Arithmetical Mean Height (S_a), which represents the average difference of each point on the surface to the arithmetical mean of the surface; Maximum Height Difference (S_z), which shows the difference between the maximum and minimum peak points; Root Mean Square (S_q), which is the standard deviation of height points; Arithmetic Mean Peak Curvature (S_{pc}), which demonstrates the sharpness of peak points; and Skewness (S_{sk}), which demonstrates the bias of roughness towards the below or above of the mean plane.

Once the comparison parameters are determined, the next step is to select the fabrication steps that are assumed to have a significant impact on the fabrication process. For this experiment, the following steps have been chosen for comparison: printing directionality, printing speed, squeegee material, angle of attack, and substrate material. The effects of each parameter will be described below, and the overall measurement results will be compared and analyzed afterwards.

Standard Fabrication Method

The figure presented below, Figure 35, shows the surface profile measurement results of the standard fabrication method. The 3D image and top view heat map both indicate that there is an incline profile towards the left of the device. This is caused by the directionality of the screen printing process, which occurs in the direction of the white arrow depicted in the figures. In the subsequent section, this effect will be further examined in detail. In addition to directionality, the top view heat map also reveals the formation of valley structures. These formations can be attributed to the surface of the squeegee material, which will be examined in more detail as one of the next measurements.

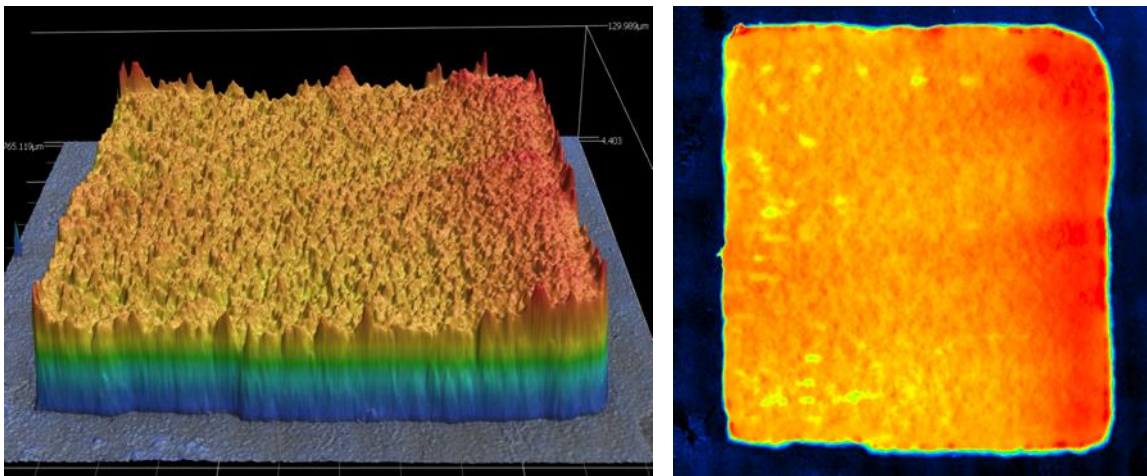


Figure 35 Standard fabrication method: Surface roughness measurement.

Printing Direction

To investigate the effect of printing directionality on the inclined surface profile, two different devices were fabricated with different printing directions. The measurement results, along with their corresponding printing directions, are presented in Figure 36. As anticipated, both devices exhibited an inclined profile in the direction of the printing. When

utilizing the stencil printing method, it is crucial to take this effect into account and position the active area further away from the edges in order to minimize its impact on device performance. Additionally, as shown in Figure 36, a valley formation occurred in the middle, which can be attributed to the surface of the squeegee material. This will be further examined in the subsequent analysis.

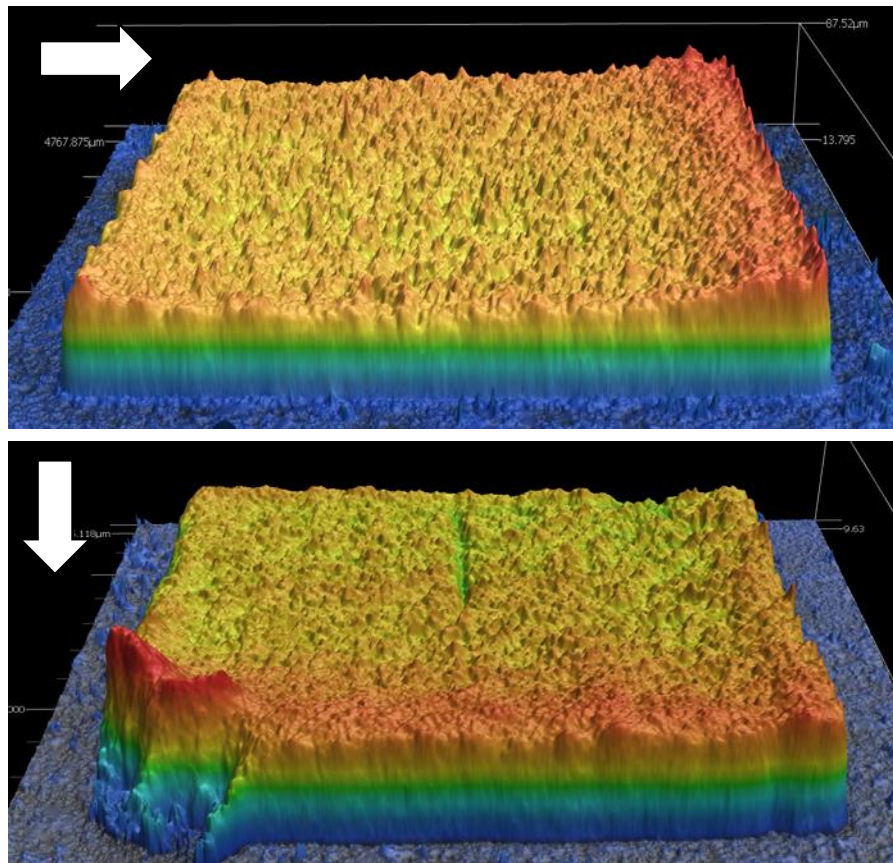


Figure 36 Surface roughness analysis: printing direction effect.

Printing Speed

This experiment involved printing two elements with different squeegee speeds, where one element was moved extremely slowly and the other extremely fast compared to the usual printing method. The measurement results are depicted in Figure 37. As shown

in the top view heat maps, moving the squeegee too fast does not allow for even distribution of the PiezoPaint™ on the surface, while moving the squeegee too slowly causes some valley formations due to the potential non-continuous motion of the squeegee. Based on these results, it can be concluded that the squeegee moving speed should be similar to the normal motion of a human arm for regular movements.

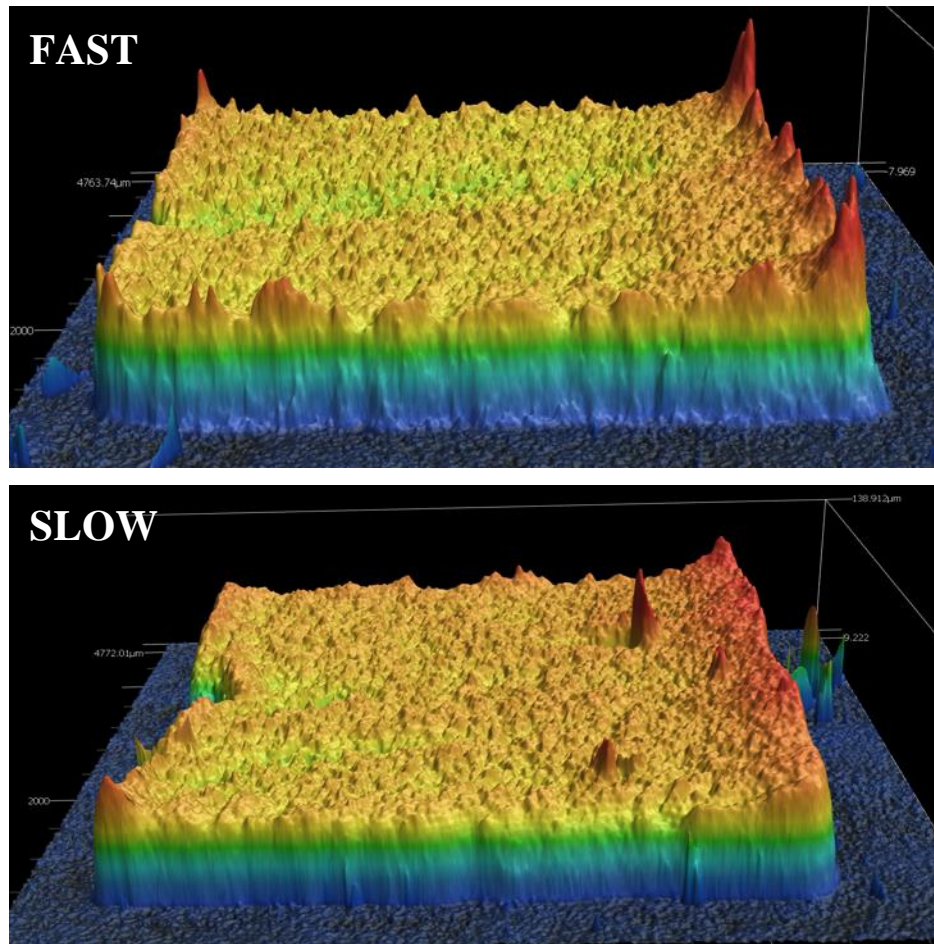


Figure 37 Surface roughness analysis: printing speed effect

Angle of Attack

This experiment involved comparing two measurements with different angles of attack, where one element was fabricated perpendicular (90°) and the other element was

fabricated at a horizontal angle (5°) compared to the stencil mask. The perpendicular method resulted in slightly better surface roughness, but the thickness control was not satisfactory. On the other hand, the horizontal fabrication method provided better control over the thickness, but it resulted in very poor surface roughness. The measurement results demonstrated in the Figure 38. Based on these findings, it can be concluded that the angle of attack causes a trade-off between the surface roughness and the thickness of the device. 30° angle of attack is found optimum for piezo-layer printing step.

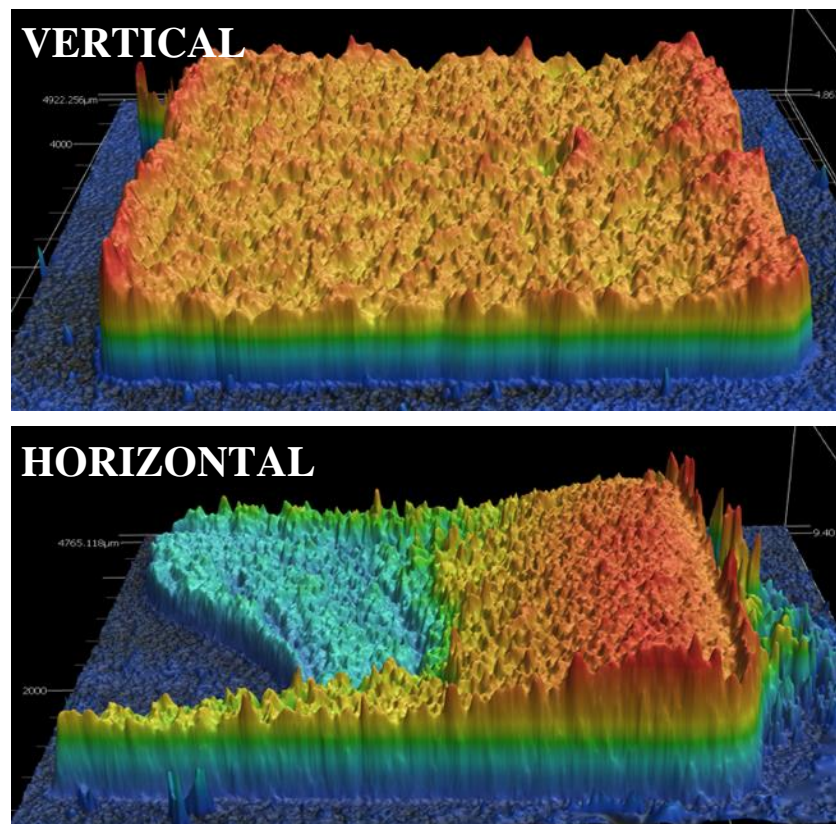


Figure 38 Surface roughness analysis: angle of attack effect

Substrate Material

The aim of this experiment was to investigate the impact of substrate material on surface roughness. The measurement results are presented in Figure 39. It was observed

that, due to the higher friction compared to glass substrate, the piezo adheres better to the substrate, which can help minimize the directionality effect. However, considering the flexibility and process-related factors, changing the substrate material is not used to optimize the surface roughness. Instead, other process steps need to be considered for achieving the desired surface roughness.

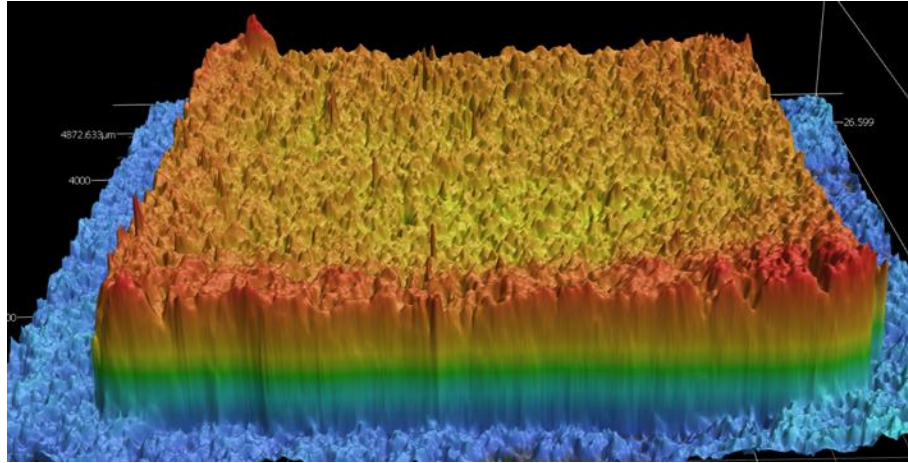


Figure 39 Surface roughness analysis: substrate material effect.

Squeegee Material

As mentioned in the previous analysis, a direct correlation between squeegee material and surface roughness was observed. To further investigate this relationship, different elements were produced using both plastic and metal squeegee materials. The results of both printing methods are shown in Table 3, where four elements were fabricated with plastic squeegee and five elements were fabricated with metal squeegee.

Table 3 shows the average results of all measurements. The comparison of the averages reveals that using a metal squeegee in the fabrication process leads to thinner devices with better surface roughness, as opposed to using a plastic squeegee. Therefore,

it is recommended to utilize a metal squeegee for achieving the desired surface roughness in the fabrication process.

Table 3 - Repetitive transducer fabrication results with plastic and metal squeegee and their results comparison.

Squeegee Type	Thickness (μm)	Sa (μm)	Sz (μm)	Sq (-)	Sp _c (μm)	Ssk -
Plastic	78.5	3.2	34.5	4.0	99.4	0.2
Plastic	48.8	3.0	53.2	3.8	101.9	0.1
Plastic	72.3	3.9	46.8	5.0	139.9	-0.3
Plastic	62.6	5.7	70.2	7.5	148.2	0.2
Metal	58.7	2.3	29.8	2.9	99.2	0.1
Metal	62.4	2.8	37.9	3.7	90.3	-0.5
Metal	56.8	2.1	25.4	2.7	87.1	-0.2
Metal	51.7	1.7	31.9	2.3	80.0	1.5
Metal	60.3	2.6	68.2	4.0	90.6	-2.2
Plastic Average	65.6	3.9	51.2	5.1	122.3	0.1
Metal Average	58.0	2.3	38.7	3.1	89.4	-0.2

Measurement Results Comparison

Table 4 presents a comparison of all measurement results, and the effect of each method is explained separately in the corresponding measurement section. In summary, based on the results shown in the table, it can be concluded that the combination of left-to-right printing directionality, average printing speed parallel to the motion of a normal human arm, a metal squeegee, and a 45-degree angle of attack yields the best results in terms of achieving a balance between device thickness and surface roughness.

Table 4 Comparison of different transducer fabrication methods and their effects on surface roughness.

Printing Method (details above)	Thickness (μm)	Sa (μm)	Sz (μm)	Sq (-)	Spc (μm)	Ssk -
Standard	72.9	3.9	36.6	4.9	94.1	0.5
Standard	78.5	3.2	34.5	4.0	99.4	0.2
Standard	64.4	4.2	75.0	5.4	110.6	-0.6
Left Right Dragging	48.8	3.0	53.2	3.8	101.9	0.1
Top Bottom Dragging	61.3	3.7	42.2	4.8	100.9	0.0
Faster Dragging	59.0	3.7	35.1	4.5	95.0	-0.4
Slower Dragging	67.9	3.7	53.1	4.9	99.0	-0.5
Metal Squeegee	58.7	2.3	29.8	2.9	99.2	0.1
Vertical Angle	53.6	4.0	82.1	6.7	77.9	-3.5
Horizontal Angle	76.6	27.0	118.1	30.3	117.6	0.2
Paper Substrate	53.4	3.3	57.1	4.2	67.4	-0.2
Average	63.2	5.6	56.1	6.9	96.6	-0.4

Comparison between Screen and Stencil Printing

Our recent work [36] has revealed that the surface roughness of stencil printed elements is comparatively lower than that of screen printed elements due to the mesh of screens. Stencils do not cause peak formations, which is the main reason behind the difference in surface roughness. A comparison of white-light profilometry measurement results between stencil and screen printing is depicted in Figure 40. Based on this comparison, we can conclude that stencil printing offers better surface roughness than screen printing, and the thickness of the layer can be more easily controlled using the stencil printing method.

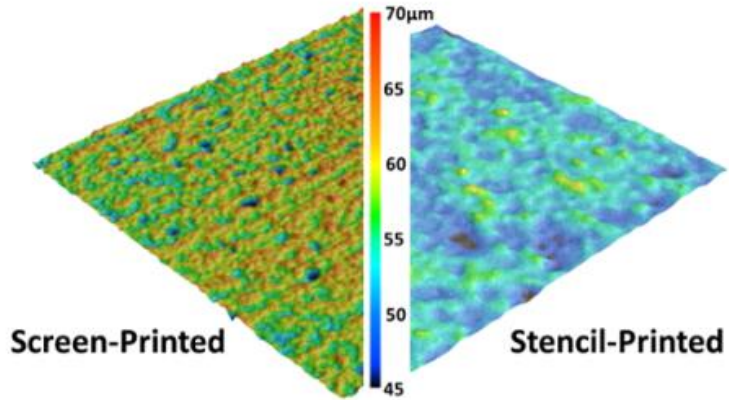


Figure 40 Surface roughness measurement comparison of screen and stencil printed surfaces.

3.10 Feature Dimension Limit Measurements

To assess the viability of the stencil printing method for various applications of different dimensions, an examination of feature sizes is conducted. This involves characterizing the minimum feature size that is required for producing array formations on limited surface areas with small element sizes. Furthermore, the previous chapter demonstrated the relationship between center frequency and device thickness. Producing thinner devices is necessary to achieve operation at higher frequencies. This section aims to characterize both the element dimensions and thickness features.

Element Dimensions

To begin with, 25 μm polyimide films are used to prepare characterization stencils through the utilization of a laser cutter, as described in the mask preparation section. These stencils feature varying dimensions, ranging from $50 \times 50 \mu\text{m}^2$ and $50 \times 1000 \mu\text{m}^2$ to $500 \times 500 \mu\text{m}^2$ and $500 \times 1000 \mu\text{m}^2$, with different pitches ranging from 50 μm to 1.5 mm as shown in the Figure 41. The characterization masks are illustrated in Figure 42.

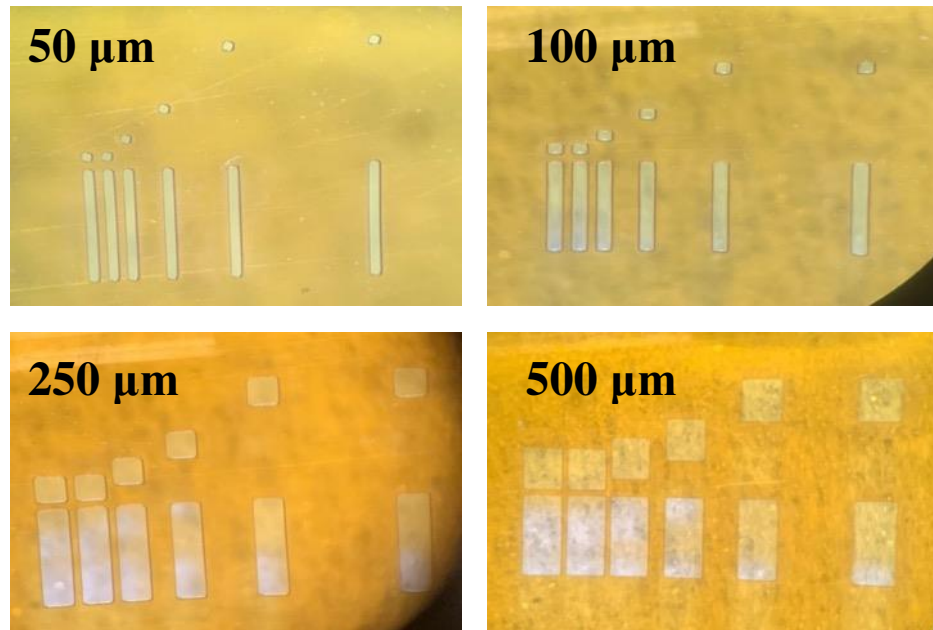


Figure 41 Microscopic images of prepared characterization stencils.

The fabrication of elements on glass substrates, without bottom electrodes, involves several process steps outlined in the device fabrication section. Under microscope images of the resulting fabricated devices are shown in Figure 42.

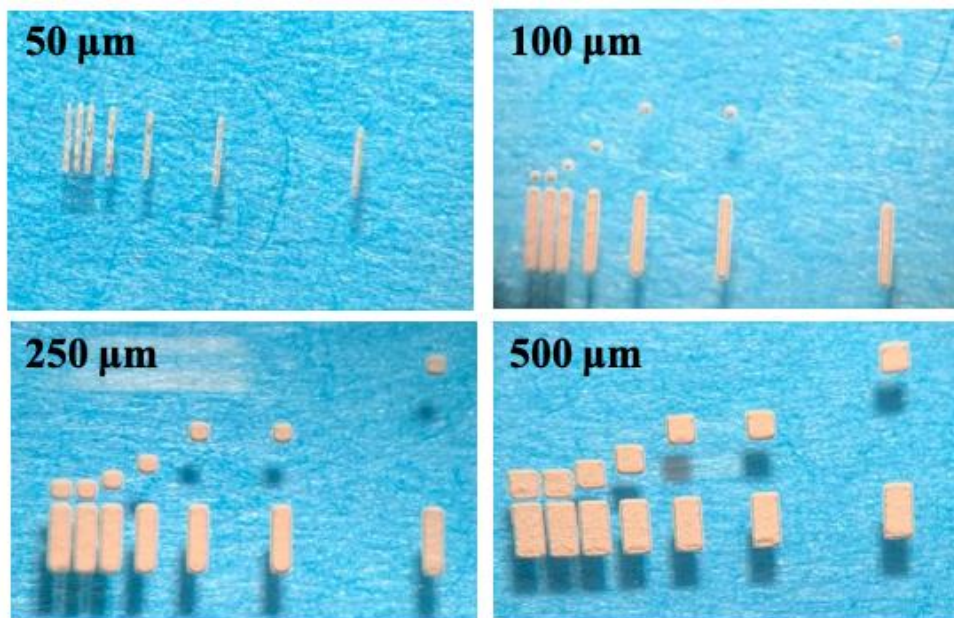


Figure 42 Microscopic images of prepared characterization elements.

In order to further analyze the outcomes, a 3D surface profilometer was employed to measure the results, which are presented in Figure 43. The measurements reveal that stencil printing can be used to create devices as small as 100 μm in width and 1 mm in length, while maintaining acceptable surface roughness values. However, the stencil printing method is not capable of fabricating 50 μm wide and 1 mm long devices, as their profile appears to be composed of randomly distributed piezo drops rather than a consistent element. Furthermore, when the length-to-width ratio (aspect ratio) is 1, elements with dimensions of 100x100 μm^2 cannot be produced using the stencil printing method. In conclusion, this study demonstrates that the stencil printing method can be utilized to fabricate elements as small as 100 μm in width, making it a valuable technique for creating arrays in small diameter catheter applications.

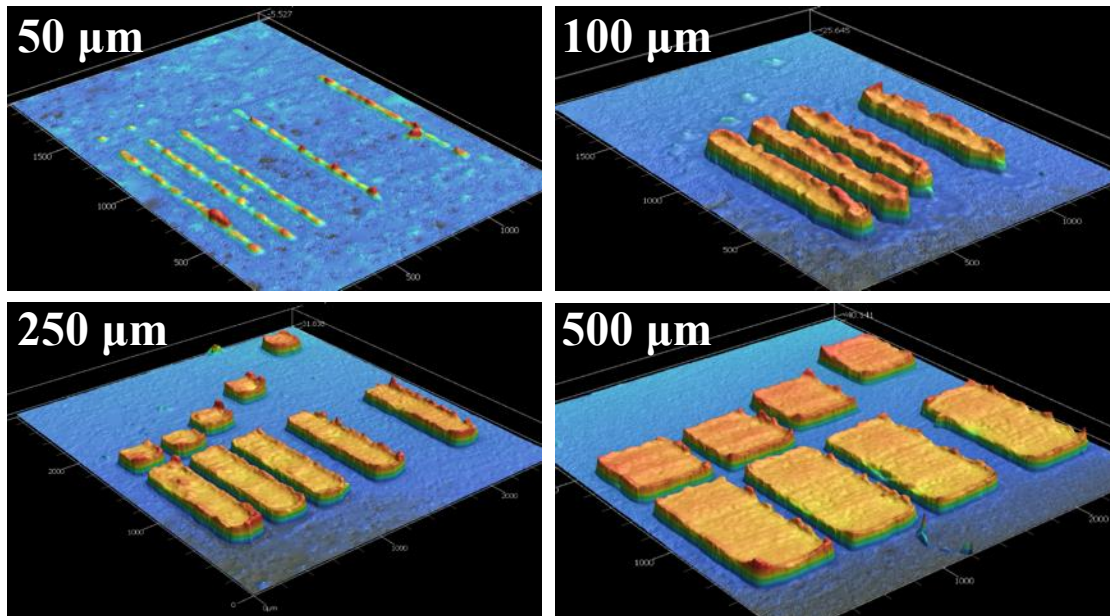


Figure 43 Surface roughness measurements of characterization elements.

Thickness

To fabricate transducer elements with varying thickness levels, the thickness of the polyimide thin films used in this study is adjusted. The thickness of the transducer element is an important application parameter, as it directly affects the center frequency of the acoustic response and determines its suitability for different applications. Specifically, three polyimide thin films with thickness levels of 12.5, 25, and 50 μm is utilized. The resulting devices have thicknesses in the range of 15-30 μm when using a 12.5 μm stencil, 27-45 μm when using a 25 μm stencil, and 52-70 μm when using a 50 μm stencil.

While utilizing thinner polyimide stencils is capable of fabricating thinner devices, the yield rate for device fabrication sharply decreases when using 12.5 μm polyimide stencils. This is primarily due to the fact that stencil printing with 12.5 μm polyimides results in small gaps on the surface, which can cause short circuits between the top and bottom electrodes, resulting in unsuccessful device fabrication. The surface defect on transducer fabrication with 12.5 μm is depicted in Figure 44, along with a comparison to a transducer fabricated using a 25 μm polyimide film. To conclude, down to 15 μm thick

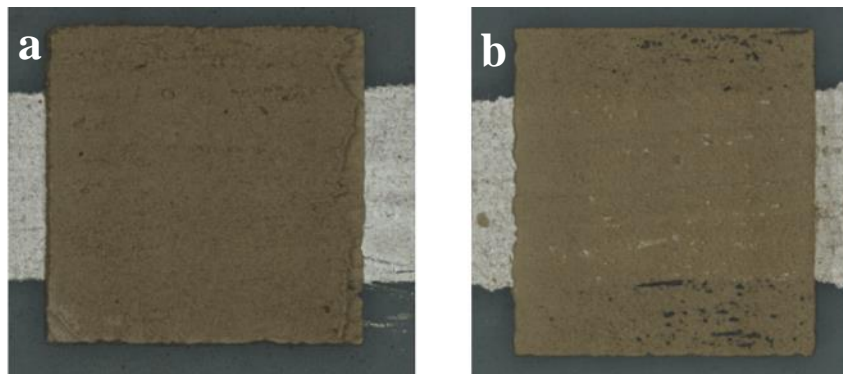


Figure 44 Microscopic surface roughness images a) without any surface defect and b) with surface defect

devices can be fabricated by stencil printing method however yield rate decreases sharply which leads to more fabrication cycle to fabricate functional device.

3.11 Flexibility Measurements

Flexibility is a crucial characteristic in the context of this study since one of the targeted applications is catheter-based ranging, which requires the transducer to be wrapped around catheters. To investigate the flexibility limits of the transducers, transducers with surface area of $4 \times 4 \text{ mm}^2$ and $2 \times 2 \text{ mm}^2$ are fabricated. After fabricating these transducers, they started to be wrapped around catheter comparable rod with different diameters starting from thickest and moving towards the thinner diameters until their surface damaged.

Transducer devices with a surface area of $4 \times 4 \text{ mm}^2$ were successfully wrapped around catheter-like rods with a diameter of 3.9 mm. Additionally, transducer devices with a surface area of $2 \times 2 \text{ mm}^2$ were wrapped around a catheter-like rod with a diameter of 2.4 mm. Figure 45 demonstrates wrapped devices with no surface damages.

During these measurements, it was observed that the orientation of the bottom electrode plays a crucial role in the device's flexibility. When the bottom electrode is perpendicular to the rod, the devices with $4 \times 4 \text{ mm}^2$ surface area can only withstand a diameter of 4.8 mm. However, when the bottom electrode is parallel to the rod orientation, the devices can survive down to 3.9 mm in diameter, resulting in an approximately 20% improvement in flexibility. Similarly, for devices with a surface area of $2 \times 2 \text{ mm}^2$, the improvement in flexibility due to orientation change is from 3.2 mm to 2.4 mm, which is

roughly a 25% improvement. For clarification purposes, Figure 46 demonstrates both perpendicular and parallel orientations.

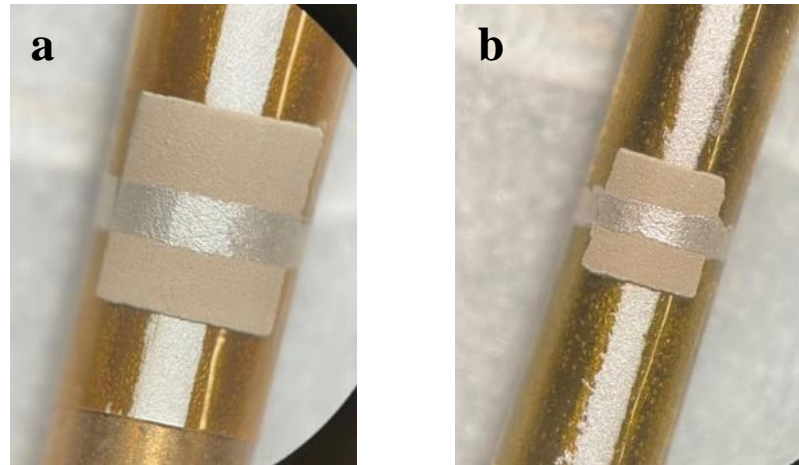


Figure 45 Transducer Wrapping on Rods with Diameters of a) $4 \times 4 \text{ mm}^2$ transducer on 3.9 mm and b) $2 \times 2 \text{ mm}^2$ transducer on 2.4 mm

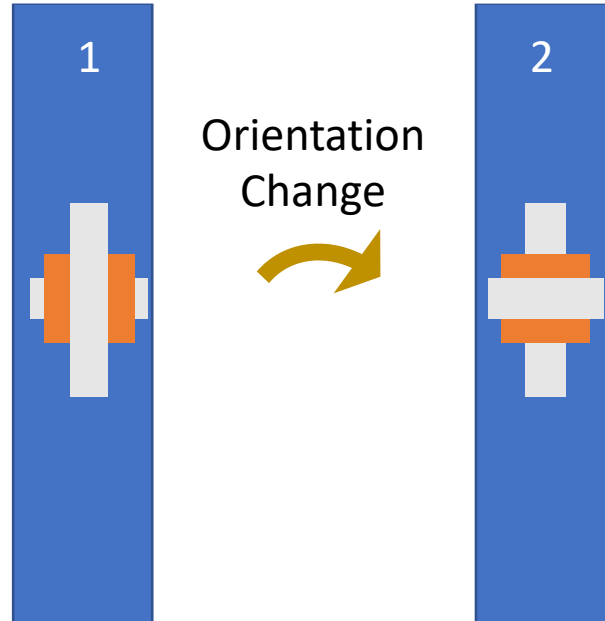


Figure 46 Illustration of 1) perpendicular and 2) parallel wrapping orientations

CHAPTER 4. ULTRASOUND APPLICATIONS OF PIEZOELECTRIC TRANSDUCERS

This chapter presents the experimental investigation of the functionality of transducers for intravascular and intracardiac ranging applications through pulse-echo measurements. The aim of this study is to evaluate the performance of both single element and multiple element transducer formations. To achieve this objective, two experimental setups were designed and implemented, which mimic the potential application cases of these transducers. The first experiment involves the use of human tissue compatible ultrasound gel to examine performance of single element transducer. The second experiment utilizes multiple elements on catheter with phantom material to examine acoustic performance of flexible array formations. The experimental details and results of each experiment are presented in the subsequent sections of this chapter.

4.1 Single Element Phantom Study

The characterization chapter involves pulse-echo measurements to evaluate the acoustic responses of transducers, using stainless steel rods as the reflector material. The acoustic impedance of the reflective material is a critical factor in pulse-echo measurements, as it determines the echo signals. The acoustic impedance of stainless-steel rods is 46 MRayl, which is significantly higher than that of soft tissue at 1.6 MRayl. As previously noted, all measurements were conducted in FC-70 tanks, which have an acoustic impedance of 1.33 MRayl. Due to the relatively high impedance mismatch between stainless steel rods and FC-70, the majority of incoming sound waves are reflected by the

stainless-steel rods, in contrast to soft tissue. To assess the ultrasonic capabilities of transducers for intravascular and intracardiac ranging applications, human tissue mimicking gel is used as the reflector material. Experiment setup is demonstrated in Figure 47.

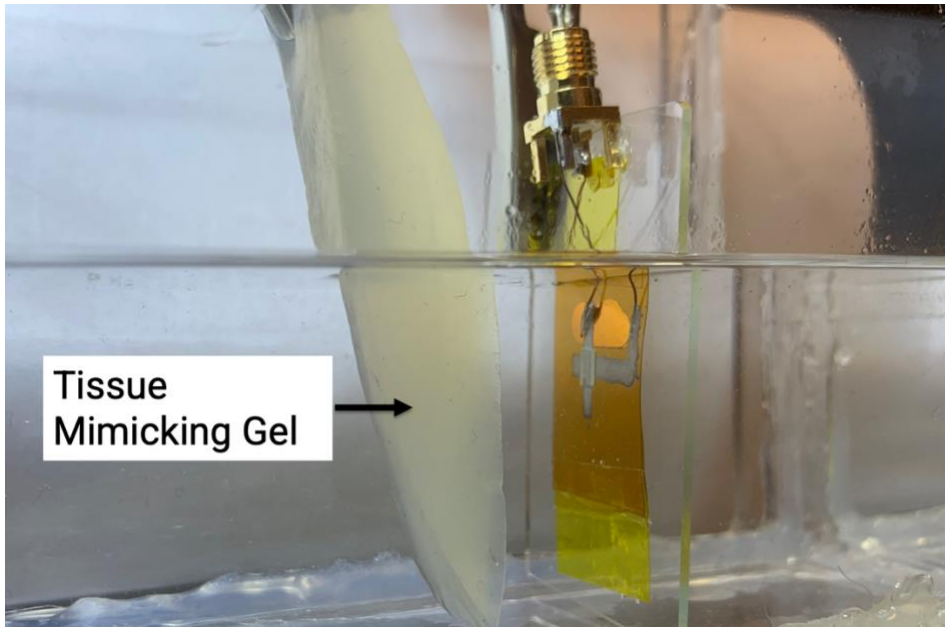


Figure 47 Setup for single element pulse-echo measurement

For this experiment, a single element transducer on polyimide thin film with an active area of 4 mm^2 and thickness level of $60 \mu\text{m}$ was utilized. This device is fabricated and poled as explained in the Chapter 2. The transducer and human tissue were placed in an FC70 tank and separated by a distance of 1.5 mm. The initial echo signal was detected as shown in the Figure 48. To normalize this graph, the actual measurement is subtracted by the reference signal obtained in the absence of any reflective material.

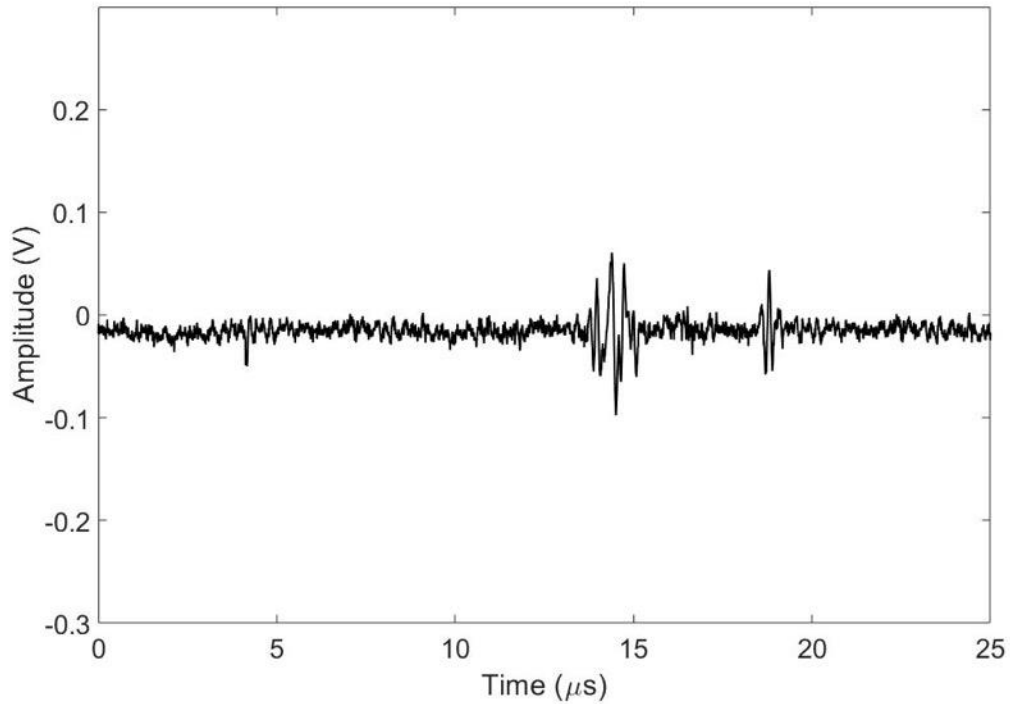


Figure 48 Single element human tissue mimicking gel pulse-echo measurement result.

To calculate the distance between the transducer and human tissue the following formula used:

$$d = (v * t) / 2 \quad (19)$$

Here, 'd' represents the distance between the transducer and human tissue. The acoustic velocity of the FC-70, denoted by 'v', has a value of 687 m/s. The measured time for initial echo signal is indicated by the variable 't', it is measured as 4.4 μs. Since the echo signal is a reflection from the target boundary, the acoustic wave travels twice the distance 'd', which is why it is multiplied by 2. Since 'v' and 't' values are known, distance can be calculated as below.

$$d = (687 * 4.4) / 2 \quad (20)$$

$$d = 1.51 \text{ mm} \quad (21)$$

The frequency response of this transducer is measured by hydrophone measurement as shown in the Figure 49. The results demonstrate that this device has working frequency range of 5-10 MHz with broad bandwidth. The subsequent phase of the experiment will evaluate the feasibility of enhancing the number of elements and mounting these transducers on a catheter to achieve clinically functional devices.

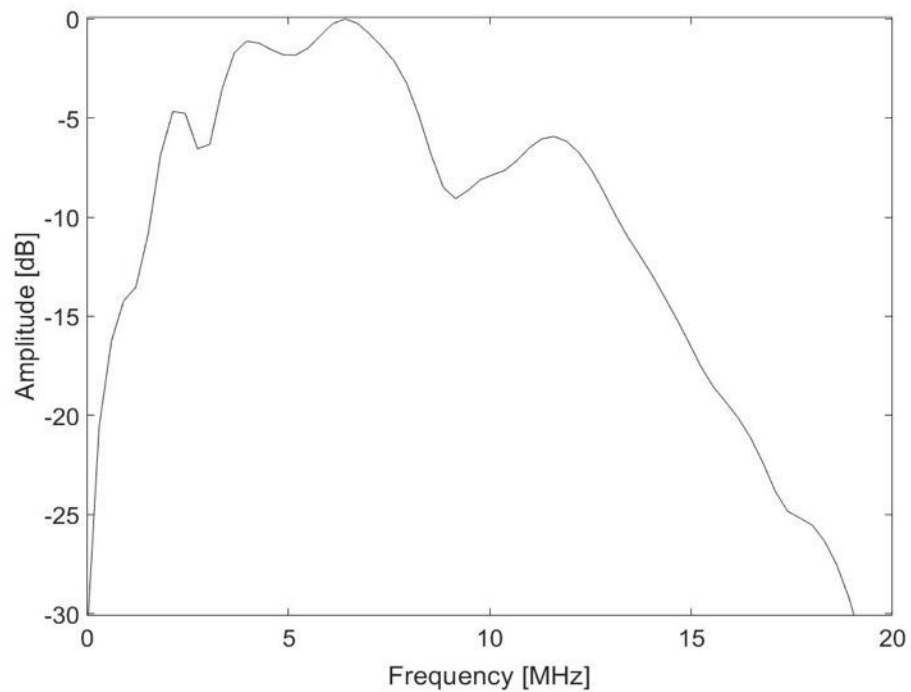


Figure 49 Frequency response measurement of single element transducer.

4.2 Multiple Elements Phantom Study

To conduct the experiment, a multiple element transducer was fabricated on polyimide tape using the stencil printing method, as described in the Fabrication chapter. The transducers were then poled and wrapped around 9 Fr (3 mm) catheters, and electrical interconnects were wired to a PCB with SMA connectors. The final formation of the transducers on catheter is illustrated in Figure 50. Each element in array formation has an active area of $3 \times 0.5 \text{ mm}^2$ and a thickness of $50 \text{ }\mu\text{m}$. One should take note that the side openings of the catheter have been sealed with epoxy. This measure is necessary to prevent the filling of the catheter with FC-70, which could lead to communication between the backing transducers.

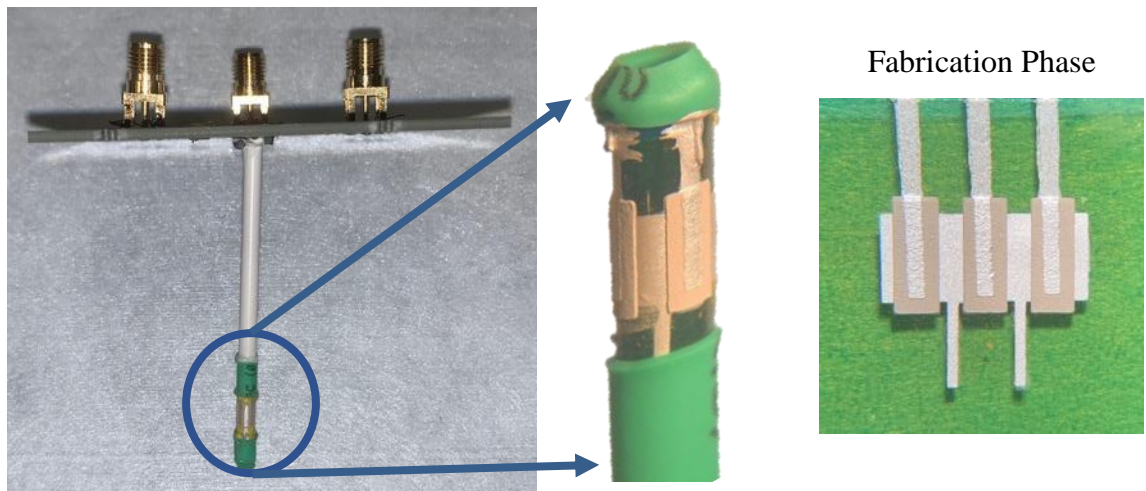


Figure 50 Multiple element transducer formation wrapped around catheter.

To perform the experiment, a custom phantom was created using ultrasonic gel (Aquaflex, Parker Lab. Inc., USA) with an acoustic impedance of 1.6 MRayl , which is similar to that of soft tissue. A channel was formed within the gel to accommodate the catheter, and the transducer element consisted of three different targets. The first target (Target 1) was located 7.5 mm away from Element 1, which was positioned at the gel-

FC70 boundary. The second target (Target 2) was located 3 mm away from Element 2 and made of polypropylene (PP) material, chosen for its acoustic impedance that closely matched that of calcified regions (2.4 MRayl). Finally, Element 3 was located 5 mm away from Target 3, which was also positioned at the gel-FC70 boundary. Pulse-echo measurements were taken from each element sequentially with a 30 dB receive gain to acoustically measure the distances to each target. Figure 51 demonstrates gel phantom with targets and corresponding transducer elements.

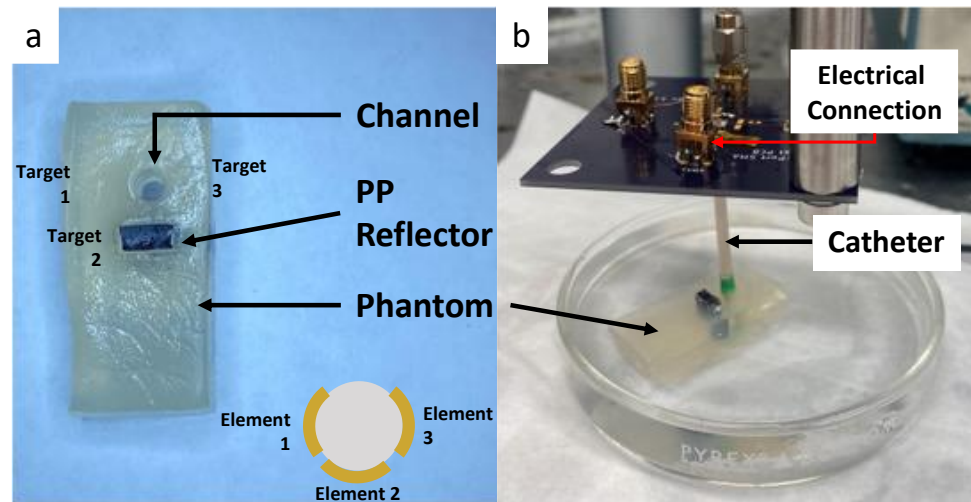


Figure 51 a) Photo of the acoustic gel phantom with a PP target and b) Pulse-echo measurement setup.

Figure 52 shows the results of pulse-echo measurements obtained inside the phantom. Echoes were observed from both the gel-FC70 boundaries and gel-PP boundaries. The initial echo signals were measured at 11.3 us for target 1, 4.2 us for target 2, and 7.3 us for target 3. Equation 19 is used to calculate distances between transducer elements and target boundaries.

The distances to each target were calculated as 8.08 mm, 3 mm, and 5.22 mm, respectively. The differences between acoustic measurements and caliper measurements can be attributed to flexible nature of the gel phantom.

Following the successful completion of the initial experiment, two additional measurements were conducted to investigate the impact of wrapping and outer layer implementation on the formation of a flexible transducer arrays.

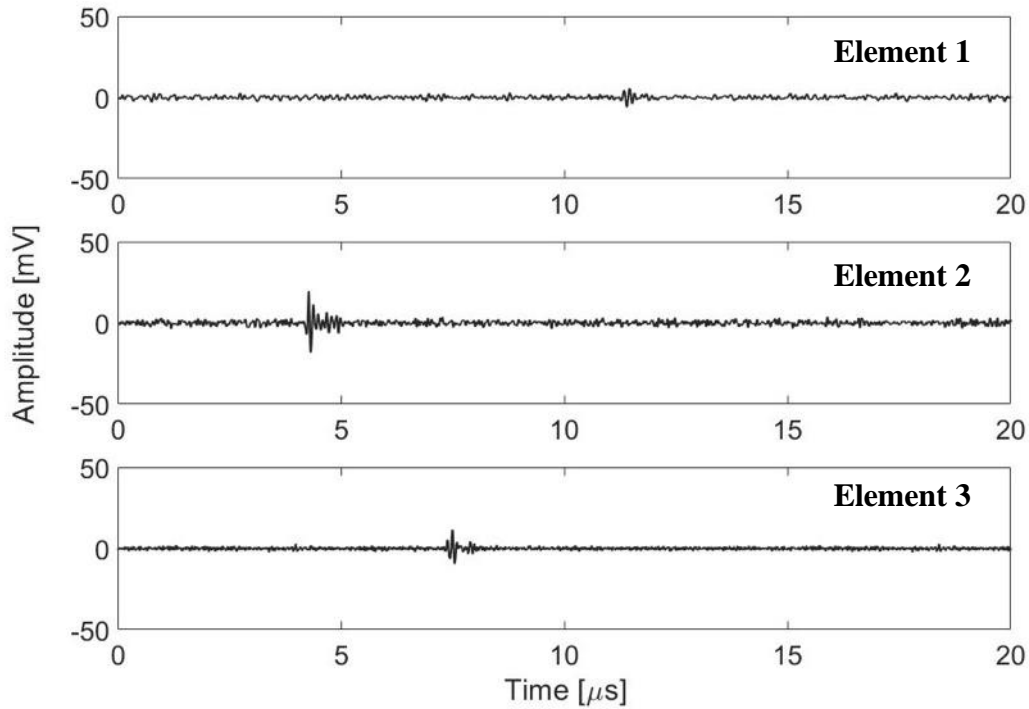


Figure 52 Echo signal measurement from different targets.

4.2.1 Wrapping Effect

The transducers utilized in this study were fabricated on tape and subsequently wrapped around catheters. To assess the impact of wrapping on the transducers' frequency response, hydrophone measurements were conducted both pre- and post-wrapping. The

hydrophone was situated 1.5 mm away from the transducer in both instances to capture acoustic signals. Frequency domain analysis, as illustrated in Figure 53, indicated that there was no significant alteration in the transducers' frequency response following their application to the catheters. A broadband acoustic response in the range of 5-10 MHz was observed, with a peak frequency of approximately 8 MHz.

Despite the extreme bending radius of 1.5 mm, the resonant frequency shifted from 7.7 MHz to 8.4 MHz during wrapping, resulting in an 8% frequency shift. The cause of this shift may be attributed to the possible contraction of the transducer thickness during wrapping, but further research is required to confirm this. The minimal impact of bending on the transducers' frequency response indicates that catheters and guidewires can be maneuvered more effectively in narrowed and tortuous arteries.

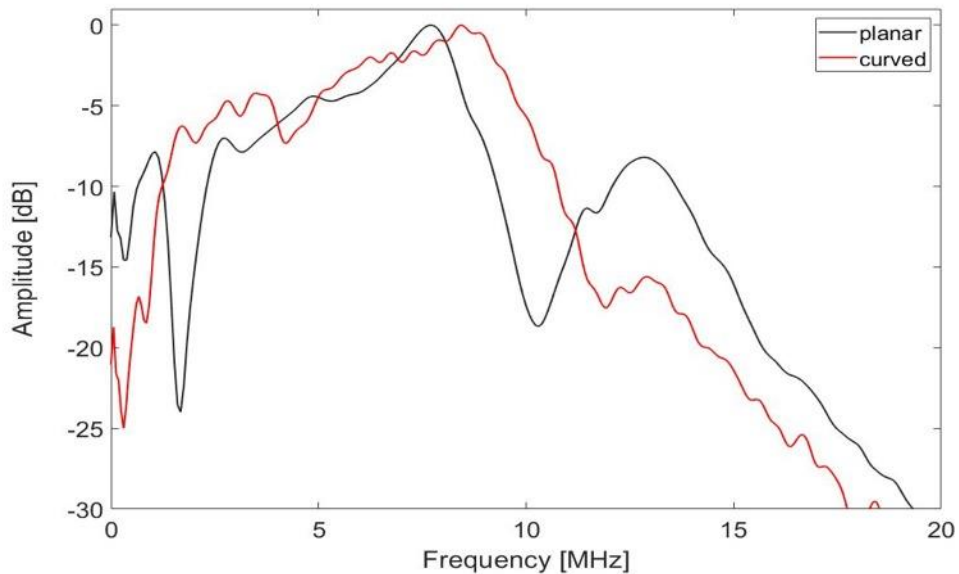


Figure 53 Hydrophone measurement of the transducer before wrapping (planar) and after wrapping (curved).

4.2.2 Outer Layer Implementation Effect

To achieve clinically functional devices, transducer array and electrical interconnects can be packed in a way to achieve a sleeve like structure for microcatheters that requires minimal modification for integration to different devices. This sleeve like structure requires outer layer implementation and to examine effect of this, device performance compared before and after covering transducer array with 12.5 μm polyimide thin film.

Pulse-echo measurements results that compare the performance of transducers before and after covering the array with a thin polyimide film, are presented in Figure 54. Observed echoes signal amplitudes are 44 mV and 42 mV before and after the implementation respectively. This result demonstrated no significant attenuation in the performance of transducers.

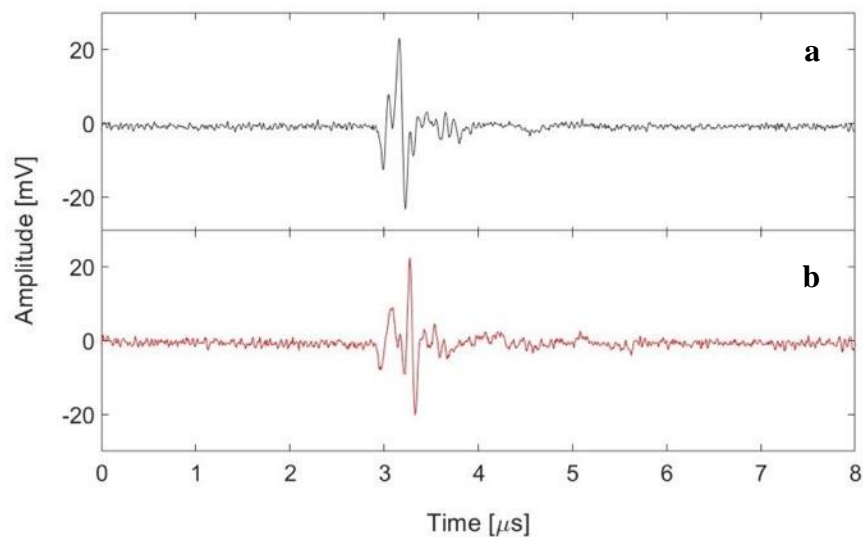


Figure 54 Echo measurement of element a) before and b) after implementation of outer layer.

In conclusion, the results of our experiments have shown that our ultrasonic transducers have the potential to be integrated into various existing catheters simply by wrapping them

with a polyimide film containing the transducers and electrical interconnect. The transducers are capable of accurately measuring distance using echoes from blood, soft tissue, and calcification boundaries, and can be applied in a variety of applications such as lumen sizing, calcified region sizing, and calcified region location detection, within the frequency range of 5-10 MHz. Overall, this study presents a promising, flexible, and low-cost approach for advancing high-performance ultrasonic transducers and transducer arrays, which has significant potential for clinical translation. Furthermore, these devices can be adapted for various applications [32, 77-82] that require conformal surface coating, flexibility and device performance tunability such as center frequency to enhance their performance.

CHAPTER 5. CONCLUSION AND FUTURE WORK

5.1 Conclusion

The purpose of this study was to fabricate and analyze flexible piezoelectric transducers and transducer arrays suitable for high frequency catheter-based applications. The fabrication process for composite piezoelectric transducers on a flexible substrate at a low process temperature using stencil printing is demonstrated step by step. It is demonstrated that performance parameters for single or multiple element transducers, such as center frequency, can be adjusted by modifying certain process variables like stencil thickness or substrate type. Since these transducers are fabricated using stencil printing, which does not require any dedicated expensive tools and can be done at low temperatures, they can be easily implemented on most catheters without any potential damage to the catheter surface. All specific research objectives related to fabrication were successfully achieved and further recommendations will be presented.

This study aims to examine the characterization of transducers through various feasibility measurements. The optimization of the poling process for PiezoPaint™ is demonstrated, which has not been previously reported in the literature. The optimization method and results are discussed by explaining the impact of each process parameter on device performance and the limitations of these parameters. The demonstration of ferroelectricity is achieved through hysteresis loop measurements, and the results are compared to the existing literature. To measure the charge constant, a novel experimental setup is developed and explained. The setup is compared with commercially available d_{33} meter measurement results and it is concluded that it can be used in case of having a

preliminary constant range. The crystal structure is examined through XRD measurements, and it is shown that the material has a perovskite crystal structure. The effect of performance parameters is examined using a KLM-based simulation tool. The completed demonstration of simulation results matching the actual measurement results has led to the conclusion that any specific requirement of an application can be achieved through simulation, and the fabrication process can be fine-tuned based on the application parameters. This approach is preferred over trying to adjust fabrication parameters to meet the application specifications.

Surface roughness was measured and compared changing process methods, such as printing speed, mask type, angle of attach, and printing orientation. The impact of manual processes on stencil printing was minimized by establishing a clear process flow based on surface roughness comparison results. The limitations of stencil printing were identified, including the minimum feature size and corresponding aspect ratios, which are crucial for fabricating transducer arrays on small diameter catheters where the printable surface area is limited. In addition, the flexibility of the transducers was demonstrated through wrapping experiments, which revealed a dependence on the appropriate wrapping method on catheter thickness.

Finally, the acoustic capabilities of these transducers were assessed through various ultrasound experiments. Initially, a pulse-echo measurement was conducted using a human tissue-mimicking gel and a single-element transducer. The results of this experiment demonstrated the suitability of these transducers for ranging applications. To further investigate the acoustic performance of multiple elements and their flexibility, a multiple-element transducer array was wrapped around a catheter and each element was targeted at

a different boundary simultaneously. The results showed that these transducers could be bent with a tight radius in the millimeter range without a significant change in their acoustic response, making them mechanically feasible. Furthermore, pulse-echo measurements results in a tissue-mimicking phantom demonstrated their potential applications in intravascular ultrasound devices for ranging purposes.

All the specific research objectives mentioned in Chapter 1 have been successfully accomplished and their feasibility has been demonstrated through various tests and analyses. It can be concluded that these devices are suitable for diverse medical sensing applications, such as ranging and lumen sizing in the 5-10 MHz range, with wide broadband acoustic response, flexibility, and ease of integration.

5.2 Recommendations for Future Work

To automate the stencil printing process, tools such as the DEK-248 Stencil Printer and K-bars can be employed, which when coupled with the KLM model, can enhance the alignment between device performance and application specifications. To further study the poling process and piezoelectric performance parameters, the impact of manual steps on surface roughness should be minimized. Investigating transducer fabrication on non-planar surfaces can exploit the liquid state of piezocomposites and enable tighter bend radius. Dip coating is another alternative fabrication method that can be used to create transducers on thinner catheters that are not feasible with stencil printing. The center frequency of the introduced transducer can be improved by developing thinner devices. To make the ultrasound devices more clinically practical, more elements are required, necessitating smaller element sizes. The integration of an integrated circuit can help reduce parasitic

effects and increase the SNR. Packaging methods can also be further examined, as evidenced by the preliminary sleeve-like structure that combines the transducer array and electrical interconnections.

In conclusion, the improvements on fabrication methods with the utilization of automated systems, such as smaller element sizes and better surface roughness, and novel packing methods, such as sleeve-like structures, can significantly enhance the feasibility of clinically practical devices in the range of 10-20 MHz for ultrasound applications. These devices can find potential applications in intravascular imaging and intracardiac applications, including metrology of cardiac valves and lumen sizing.

APPENDIX A

The datasheet of PiezoPaint™.



DATA SHEET

PiezoPaint™

A flexible piezoelectric material for soft substrates

PiezoPaint™ material is developed primarily with the aim of compatibility with flexible substrates such as textiles, plastics and paper. Itself a highly flexible material, PiezoPaint™ can be applied via common commercial deposition techniques including pad-, screen-, and stencil printing as it cures at low temperatures (< 100 °C).

Potential applications:

- Printed circuit boards
- Smart textiles
- Therapeutic ultrasound
- Underwater acoustics

Material properties

Electrical	Symbol	Unit	PiezoPaint™
Relative dielectric permittivity at 1 kHz	K_{33}		80
Dielectric dissipation factor at 1 kHz	$\tan\delta$	10^{-2}	3.5
Electromechanical			
Coupling factor, thickness	k_t	%	8.2
Piezoelectric charge coefficient ¹⁾	d_{33}	pC/N	40
Piezoelectric charge coefficient ^{1,2)}	d_{31}	pC/N	15
Frequency constant, thickness	N_t	Hz m	1410
Mechanical			
Acoustic impedance	Z_a	MRayl	13.9
Density	ρ	g/cm ³	5.0

1) Semi-clamped, in the case of films printed onto substrate.

2) Estimated value, under evaluation

CTS | Ferroperm is a company completely dedicated to the production of high quality piezoelectric ceramics for our main strategic markets: Vibration sensors, flow-meters, medical diagnostics, underwater acoustics and NDT. We have more than 50 years of experience in production of advanced piezoelectric ceramics, and employ today more than 50 motivated people in management, production, development and research. We have extensive experience in development and improvement of products, which can fulfil customers' individual needs.

APPENDIX B

The datasheet of utilized silver-ink, AG-510.



TECHNICAL DATA SHEET

AG-510 SILVER CONDUCTIVE INK

AG-510 is designed for screen printing in:

- flex circuit
- membrane switch
- touch screens
- other printed electronic applications

DESCRIPTION

- Silver filled, electrically conductive, screen printable ink or coating
- Can be printed on ITO
- Can be thinned with solvent for spraying or dipping for EMI/RFI shielding applications
- Extremely tough, scuff resistant, crease resistant and has excellent adhesion to polyester, polyimide and most other substrates.
- Designed to give a good balance between long open time on screens and short drying time in subsequent drying processes.
- Compatible with our UV curable dielectrics, all of our conductive epoxy adhesives and our UV curable component encapsulants and conformal coatings.
- Formulation of AG-510 balances longer open time with quicker drying
- AG-510 can be blended with C-100 carbon resistive ink to give intermediate resistivity ranges.

TYPICAL PROPERTIES

Appearance	Thixotropic silver colored ink
Viscosity	
SC4-14 spindle @ shear 20, 25°C	3,400 – 4,200 cps
Thixotropic Ratio	1.8-2.2
Drying Time	90 seconds to 4 minutes at 130°C (depending upon air flow and oven heat profile)
Total % NV Solids	68% +/- 2%
Hegman Gauge	<10.0 μ
Surface Resistivity	< .015 Ω/square /mil when fully dried
Shelf Life	6 months in unopened container

AG-510 SILVER CONDUCTIVE INK

Guidelines are intended to provide a starting point for evaluation. Applied Ink Solutions recognizes that each customer's manufacturing process is unique, and we are available to provide technical assistance to resolve your processing issues. Call us to discuss your application in more detail.

The properties are accurate to the best of our knowledge and Applied Ink Solutions makes no guarantees for customer specifications established in applications where this product is used. Customer assumes responsibility for determining fitness of use in their particular application.

Application Guidelines

AG-510 will settle when it is stored in sealed containers over a period of time. It is essential to mix the material thoroughly before use to re-disperse any settled silver particles and to return the ink to a more desirable viscosity.

Screening

A monofilament polyester (157 to 230 mesh) or a stainless steel (165 to 325 mesh) screen is recommended, with emulsion thickness between .001" and .004". A polyurethane squeegee with a Shore 'A' durometer between 60 and 70 is recommended.

Thinning & Cleanup

Use Solvent 20 for thinning. Use Solvent 10 or a suitable screen cleaner for cleanup. If faster drying time is required, contact Applied Ink Solutions for solvent recommendations. If solvent based inks are left on screens for any length of time, the ink will gradually thicken as solvent evaporates. If ink is to be left on an inactive press for any length of time, solvent evaporation can be minimized by pooling the ink into a small area instead of leaving it spread out over a large area. Pooling the ink reduces the surface area, thus slowing the drying process. Always check the viscosity of ink that has been recovered from a screen and add small amounts of solvent while mixing thoroughly to restore viscosity. Solvent can be added to reclaim thickened ink as long as the ink has not dried and hardened completely.

Drying

It is essential that all residual solvent be removed from this ink once it is applied. Incomplete drying will cause the ink to appear dry on the surface while trapping solvent underneath the surface. Over time, this trapped solvent will migrate out of the ink, and can cause adhesion problems with any material, such as dielectrics, applied over the ink.

Completeness of Drying

Evaluate the point-to-point resistance along one of the screened conductive paths after one pass through the drying oven or one cycle in a batch-drying oven. Run the substrate through another drying cycle. Measure the point-to-point resistance again along the same path and compare it to the original reading. If the resistance decreases by less than 10%, then the ink is essentially dry after the first drying cycle or pass through the oven. If the resistance decreases by more than 10%, then more drying time is required to completely remove the solvent.

Health & Safety

Products manufactured by Applied Ink Solutions, are intended for use in an industrial environment by trained personnel. Please follow proper health/safety processes regarding storage, handling and processing of the products.

2/1/2017 Rev. 2

APPENDIX C

The Master excel spreadsheet is demonstrated below. All the data is kept in the excel in including the electrical input impedance measurements for each element. After starting to acoustic measurements, this method is no further utilized due to larger data storage requirements.

A	B	C	D	E	F	G	H	J	L	M	N
Date	Device No	Piezo Dry Time	Piezo Dry Temp - C	Poling Temp - C	Applied Voltage (AV)	AV Time (mins)	Results	Status	Experiments	SMA	Data
2/18/22	1	25 mins	140	140	200V	25	Bad	Measured	-	-	1
2/18/22	2	25 mins	140	140	250V	25	Good	Measured	-	-	1
2/18/22	3	25 mins	140	140	200V	25	Good	Measured	Aging	1	1
2/18/22	4	25 mins	140	140	300V	25	Good	Measured	Heating, Repoling	-	1
2/18/22	5	25 mins	140	140	280V	25	Good	Measured	Heating, Repoling	-	1
2/18/22	6	25 mins	140	140	200V	25	Good	Measured	Aging	1	1
2/22/22	7	-	-	140	-	-	Bad	Short	-	-	-
2/22/22	8	25 mins	140	140	-	-	Bad	Short	-	-	-
2/22/22	9	25 mins	140	140	300V	25	Bad	Measured	-	-	1
2/22/22	10	25 mins	140	140	200V	20	Not Bad	Measured	-	-	1
2/24/22	11	25 mins	140	140	200V	10	Good	Measured	Voltage,Time	-	1
2/25/22	12	40 mins	140	140	200V	20	Bad, not	Measured	-	-	1
2/25/22	13	40 mins	140	140	200V	10	Bad, not	Measured	-	-	1
3/1/22	14	30 mins	140	140	250V	25	Bad, repol	Measured	-	-	1
3/1/22	15	30 mins	140	140	500V	10	Bad	Measured	-	-	1
3/1/22	16	15 mins	140	140	400V	20	Bad but j	Measured	-	-	1
3/1/22	17	25 mins	140	140	470V	2	Not Bad	Measured	-	-	1
3/3/22	18	40 mins	140	140	200V	15	Bad	Measured	-	-	1
3/4/22	19	40 mins	140	180	250V	25	Bad	Measured	-	-	1
3/4/22	20	80 mins	140	140	350V	10	Bad	Measured	-	-	1
3/4/22	21	10 mins	180	180	300V	20	Good	Measured	-	1	1
3/4/22	23	40 mins	180	140	200V	10	Good	Measured	-	1	1
3/8/22	24	120 mins	140	140	250V	10	Good	Measured	-	1	1
3/8/22	25	120 mins	140	140	250V	10	Not Bad	Measured	-	-	1
3/15/22	26	10 mins	90	90	250V	10	Good	Measured	Voltage	-	1
3/15/22	27	10 mins	90	-	-	-	-	Needs to Be Poled	-	1	-
3/29/22	28	25 mins	140	140	300V	10	Good	Measured	Poling Time	-	1
4/12/22	29	10 mins	140	-	-	-	-	Needs to Be Poled	-	1	-
4/13/22	30	10 mins	140	140	300V	10	Good	Measured	Poling Time	-	1
4/13/22	32	12 mins	140	140	300V	2	Good	Measured	Poling Time, Voltage	-	1
4/19/22	35	35 mins	140	-	-	-	-	Needs to Be Poled	-	-	-
4/19/22	36	35 mins	140	140	300V	1	Good	Measured	Poling Time	-	1
9/29/22	37	35 mins	140	-	-	-	-	Needs to Be Poled	-	-	-

APPENDIX D

KLM simulation tool material characteristic parameters can be found below for PiezoPaint™, silver-ink, glass and polyimide substrates.

PiezoPaint™

Density (kg/m ³):	5000
Velocity (m/sec):	1410
Quality factor:	65
measured at (MHz):	5
with frequency dependence:	-1
Piezoelectric coupling constant (clamped):	0.082
Relative dielectric constant:	100
Dielectric loss tangent:	0.025

Silver-Ink

Density (kg/m ³):	10600
Velocity (m/sec):	3600
Quality factor:	100000000
measured at (MHz):	1
with frequency dependence:	0
Thickness(mm):	0.1

Glass Slide

Density (kg/m ³):	2650
Velocity (m/sec):	5750
Quality factor:	1000000
measured at (MHz):	5
with frequency dependence:	-1
Thickness(mm):	1

Polyimide Film

Density (kg/m ³):	1454
Velocity (m/sec):	2175
Quality factor:	1270
measured at (MHz):	1
with frequency dependence:	-1
Thickness(mm):	0.05

REFERENCES

- [1] I. Donald, J. Macvicar, and T. G. Brown, "Investigation of Abdominal Masses by Pulsed Ultrasound," (in English), *Lancet*, vol. 1, no. Jun7, pp. 1188-1194, 1958. [Online]. Available: <Go to ISI>://WOS:A1958WB50000002.
- [2] P. N. T. Wells, "Ultrasound imaging," (in English), *Phys Med Biol*, vol. 51, no. 13, pp. R83-R98, Jul 7 2006, doi: 10.1088/0031-9155/51/13/R06.
- [3] H. Hu *et al.*, "A wearable cardiac ultrasound imager," *Nature*, vol. 613, no. 7945, pp. 667-675, 2023/01/01 2023, doi: 10.1038/s41586-022-05498-z.
- [4] C. Wang *et al.*, "Bioadhesive ultrasound for long-term continuous imaging of diverse organs," (in eng), *Science*, vol. 377, no. 6605, pp. 517-523, Jul 29 2022, doi: 10.1126/science.abo2542.
- [5] B. Wang *et al.*, "Three-Dimensional Intravascular Ultrasound Imaging Using a Miniature Helical Ultrasonic Motor," *IEEE Transactions on Ultrasonics, Ferroelectrics, and Frequency Control*, vol. 69, no. 2, pp. 681-690, 2022, doi: 10.1109/TUFFC.2021.3132607.
- [6] M. Habib, I. Lantgios, and K. Hornbostel, "A review of ceramic, polymer and composite piezoelectric materials," *Journal of Physics D: Applied Physics*, vol. 55, no. 42, p. 423002, 2022/08/19 2022, doi: 10.1088/1361-6463/ac8687.
- [7] K. K. Sappati and S. Bhadra, "Piezoelectric Polymer and Paper Substrates: A Review," *Sensors*, vol. 18, no. 11, p. 3605, 2018. [Online]. Available: <https://www.mdpi.com/1424-8220/18/11/3605>.
- [8] V. Cauda, G. Canavese, and S. Stassi, "Nanostructured piezoelectric polymers," *Journal of Applied Polymer Science*, vol. 132, no. 13, 2015, doi: <https://doi.org/10.1002/app.41667>.
- [9] M. Smith and S. Kar-Narayan, "Piezoelectric polymers: theory, challenges and opportunities," *International Materials Reviews*, vol. 67, no. 1, pp. 65-88, 2022/01/02 2022, doi: 10.1080/09506608.2021.1915935.
- [10] A. Jain, P. K. J., A. K. Sharma, A. Jain, and R. P.N, "Dielectric and piezoelectric properties of PVDF/PZT composites: A review," *Polymer Engineering & Science*, vol. 55, no. 7, pp. 1589-1616, 2015, doi: <https://doi.org/10.1002/pen.24088>.
- [11] G. Fleury, D. Melo de Lima, K. Hynynen, R. Berriet, O. Le Baron, and B. Huguenin, *New piezocomposite transducers for therapeutic ultrasound* (Biomedical Optics). SPIE, 2003.

- [12] W. P. Mason, "Piezoelectricity, its history and applications," *The Journal of the Acoustical Society of America*, vol. 70, no. 6, pp. 1561-1566, 1981, doi: 10.1121/1.387221.
- [13] K. Uchino, "Introduction to Piezoelectric Actuators and Transducers," p. 41, 06/17 2003.
- [14] G. H. Haertling, "Ferroelectric Ceramics: History and Technology," *Journal of the American Ceramic Society*, vol. 82, no. 4, pp. 797-818, 1999, doi: <https://doi.org/10.1111/j.1151-2916.1999.tb01840.x>.
- [15] S. Park, C.-H. Kim, W.-J. Lee, S. Sung, and M.-H. Yoon, "Sol-gel metal oxide dielectrics for all-solution-processed electronics," *Materials Science and Engineering: R: Reports*, vol. 114, pp. 1-22, 2017/04/01/ 2017, doi: <https://doi.org/10.1016/j.mser.2017.01.003>.
- [16] M. Mizuno, "Piezoelectric Effects and Materials," in *Encyclopedia of Thermal Stresses*, R. B. Hetnarski Ed. Dordrecht: Springer Netherlands, 2014, pp. 3728-3735.
- [17] R. Mbarki, N. Baccam, K. Dayal, and P. Sharma, "Piezoelectricity above the Curie temperature? Combining flexoelectricity and functional grading to enable high-temperature electromechanical coupling," *Applied Physics Letters*, vol. 104, no. 12, p. 122904, 2014, doi: 10.1063/1.4869478.
- [18] M. Stewart, M. Cain, and D. Hall, "Ferroelectric hysteresis measurement and analysis," United Kingdom, 1368-6550, 1999. [Online]. Available: http://inis.iaea.org/search/search.aspx?orig_q=RN:31016506
- [19] D. Isarakorn *et al.*, "Epitaxial piezoelectric MEMS on silicon," *Journal of Micromechanics and Microengineering*, vol. 20, 04/07 2010, doi: 10.1088/0960-1317/20/5/055008.
- [20] M. Castillo, P. Acevedo, and E. Moreno, "KLM model for lossy piezoelectric transducers," *Ultrasonics*, vol. 41, no. 8, pp. 671-679, 2003/11/01/ 2003, doi: [https://doi.org/10.1016/S0041-624X\(03\)00101-X](https://doi.org/10.1016/S0041-624X(03)00101-X).
- [21] W. P. Mason, *Electromechanical transducers and wave filters*. van Nostrand, 1942.
- [22] R. Krimholtz, D. A. Leedom, and G. L. Matthaei, "New equivalent circuits for elementary piezoelectric transducers," *Electronics Letters*, vol. 6, no. 13, pp. 398-399. [Online]. Available: https://digital-library.theiet.org/content/journals/10.1049/el_19700280
- [23] M. Redwood, "Experiments with the Electrical Analog of a Piezoelectric Transducer," *The Journal of the Acoustical Society of America*, vol. 36, no. 10, pp. 1872-1880, 1964/10/01 1964, doi: 10.1121/1.1919285.

- [24] R. Lerch, "Finite element analysis of piezoelectric transducers," in *IEEE 1988 Ultrasonics Symposium Proceedings.*, 2-5 Oct. 1988 1988, pp. 643-654 vol.2, doi: 10.1109/ULTSYM.1988.49457.
- [25] S. Sherrit, S. Leary, and Y. Bar-Cohen, "Comparison of the Mason and KLM Equivalent Circuits for Piezoelectric Resonators in the Thickness Mode," *Proceedings of the IEEE Ultrasonics Symposium*, vol. 2, 07/01 2000.
- [26] C. G. Oakley, "Calculation of ultrasonic transducer signal-to-noise ratios using the KLM model," *IEEE Transactions on Ultrasonics, Ferroelectrics, and Frequency Control*, vol. 44, no. 5, pp. 1018-1026, 1997, doi: 10.1109/58.655627.
- [27] K. S. Van Dyke, "The piezo-electric resonator and its equivalent network," *Proceedings of the Institute of Radio Engineers*, vol. 16, no. 6, pp. 742-764, 1928.
- [28] S. Singh and A. Goyal, "The origin of echocardiography: a tribute to Inge Edler," (in eng), *Tex Heart Inst J*, vol. 34, no. 4, pp. 431-8, 2007.
- [29] Y. Zhang and A. Demosthenous, "Integrated Circuits for Medical Ultrasound Applications: Imaging and Beyond," *IEEE Transactions on Biomedical Circuits and Systems*, vol. 15, no. 5, pp. 838-858, 2021, doi: 10.1109/TBCAS.2021.3120886.
- [30] J. Hong *et al.*, "A Dual-Mode Imaging Catheter for Intravascular Ultrasound Application," *IEEE Transactions on Medical Imaging*, vol. 38, no. 3, pp. 657-663, 2019, doi: 10.1109/TMI.2018.2869942.
- [31] D. Wildes *et al.*, "4-D ICE: A 2-D Array Transducer With Integrated ASIC in a 10-Fr Catheter for Real-Time 3-D Intracardiac Echocardiography," *IEEE Transactions on Ultrasonics, Ferroelectrics, and Frequency Control*, vol. 63, no. 12, pp. 2159-2173, 2016, doi: 10.1109/TUFFC.2016.2615602.
- [32] C. Tekes *et al.*, "Real-time imaging system using a 12-MHz forward-looking catheter with single chip CMUT-on-CMOS array," in *2015 IEEE International Ultrasonics Symposium (IUS)*, 21-24 Oct. 2015 2015, pp. 1-4, doi: 10.1109/ULTSYM.2015.0521.
- [33] "PiezoPaint™ printed ceramics." CTS Ferroperm Piezoceramics. <https://www.ferropermpiezoceramics.com/product/piezopaint/> (accessed March 10th, 2023).
- [34] L. M. Bierregaard *et al.*, "Cost-effective screen printed linear arrays for medical imaging fabricated using PZT thick films," in *2015 IEEE International Ultrasonics Symposium (IUS)*, 21-24 Oct. 2015 2015, pp. 1-4, doi: 10.1109/ULTSYM.2015.0277.
- [35] A. Almusallam, K. Yang, D. Zhu, R. Torah, J. Tudor, and S. Beeby, "Development of a low temperature PZT/polymer paste for screen printed flexible electronics

- applications," in *SENSORS, 2014 IEEE*, 2-5 Nov. 2014 2014, pp. 2183-2186, doi: 10.1109/ICSENS.2014.6985472.
- [36] L. W. Bradley, Y. S. Yaras, B. Karahasanoglu, B. Atasoy, and F. L. Degertekin, "Application of Low Temperature Processed 0-3 Composite Piezoelectric Thick Films in Flexible, Non-planar, High Frequency Ultrasonic Devices," *Ieee Sens J*, pp. 1-1, 2023, doi: 10.1109/JSEN.2023.3251030.
- [37] T. Kaneko, K. Iwata, and M. Kobayashi, "Sol-gel composite film fabrication by paint stencil printing," in *2014 IEEE International Ultrasonics Symposium*, 3-6 Sept. 2014 2014, pp. 975-978, doi: 10.1109/ULTSYM.2014.0239.
- [38] C. Fei *et al.*, "Fabrication and Characterization of High-Sensitivity Ultrasonic Transducers With Functionally Graded Design," *Ieee Sens J*, vol. 19, no. 16, pp. 6650-6654, 2019, doi: 10.1109/JSEN.2019.2905625.
- [39] R. C. Luo and T. Chih Shan, "Thin film PZT pressure/temperature sensory arrays for on-line monitoring of injection molding," in *IECON'01. 27th Annual Conference of the IEEE Industrial Electronics Society (Cat. No.37243)*, 29 Nov.-2 Dec. 2001 2001, vol. 1, pp. 375-380 vol.1, doi: 10.1109/IECON.2001.976511.
- [40] Y. Ohara, M. Miyayama, K. Koumoto, and H. Yanagida, "Partially stabilized zirconia-polymer composites fabricated with an ultrasonic cutter," *Journal of materials science letters*, vol. 12, pp. 1279-1282, 1993.
- [41] U. Laurentiu, C. Romeo, S. Cristina, M. Aradoaei, P. Olga, and M. Baibarac, "Flexible Piezo-Electric Composites for 3D-Printed Harvesters," in *2020 International Conference and Exposition on Electrical And Power Engineering (EPE)*, 22-23 Oct. 2020 2020, pp. 470-473, doi: 10.1109/EPE50722.2020.9305569.
- [42] R. Mansour, O. A. Omoniyi, A. Reid, L. Liang, R. O'Leary, and J. F. C. Windmill, "A Novel 3D-Printed (0-3) Piezocomposite Material for Sensing Applications," in *2020 IEEE International Conference on Flexible and Printable Sensors and Systems (FLEPS)*, 16-19 Aug. 2020 2020, pp. 1-4, doi: 10.1109/FLEPS49123.2020.9239541.
- [43] D. B. Kim, S. W. Kim, Y. E. Kim, H. J. Choi, and Y. S. Cho, "Room-temperature processed Ag/Pb(Zn_{1/3}Nb_{2/3})O₃-Pb(Zr_{0.5}Ti_{0.5})O₃-based composites for printable piezoelectric energy harvesters," *Composites Science and Technology*, vol. 218, p. 109151, 2022/02/08/ 2022, doi: <https://doi.org/10.1016/j.compscitech.2021.109151>.
- [44] O. A. Omoniyi, R. Mansour, A. Reid, L. Liang, R. O. Leary, and J. F. C. Windmill, "3D-printing of a piezocomposite material with high filler content for transducer applications," in *2020 IEEE International Ultrasonics Symposium (IUS)*, 7-11 Sept. 2020 2020, pp. 1-3, doi: 10.1109/IUS46767.2020.9251684.

- [45] S. Mishra, L. Unnikrishnan, S. K. Nayak, and S. Mohanty, "Advances in Piezoelectric Polymer Composites for Energy Harvesting Applications: A Systematic Review," *Macromolecular Materials and Engineering*, vol. 304, no. 1, p. 1800463, 2019, doi: <https://doi.org/10.1002/mame.201800463>.
- [46] N. Ibrahim, J. O. Akindoyo, and M. Mariatti, "Recent development in silver-based ink for flexible electronics," *Journal of Science: Advanced Materials and Devices*, vol. 7, no. 1, p. 100395, 2022/03/01/ 2022, doi: <https://doi.org/10.1016/j.jsamd.2021.09.002>.
- [47] D. Tobjörk and R. Österbacka, "Paper Electronics," *Advanced Materials*, vol. 23, no. 17, pp. 1935-1961, 2011, doi: <https://doi.org/10.1002/adma.201004692>.
- [48] S. Khan, L. Lorenzelli, and R. S. Dahiya, "Technologies for Printing Sensors and Electronics Over Large Flexible Substrates: A Review," (in English), *Ieee Sens J*, vol. 15, no. 6, pp. 3164-3185, Jun 2015, doi: 10.1109/Jsen.2014.2375203.
- [49] E. Horvath, A. Torok, P. Ficzer, I. Zádor, and P. Rácz, "Optimisation of Computer-aided Screen Printing Design," *Acta Polytechnica Hungarica*, vol. 11, pp. 29-44, 01/01 2014.
- [50] M. Jung, S. Jeon, and J. Bae, "Scalable and facile synthesis of stretchable thermoelectric fabric for wearable self-powered temperature sensors," *RSC Advances*, vol. 8, pp. 39992-39999, 11/30 2018, doi: 10.1039/C8RA06664G.
- [51] K. Solin, M. Beaumont, M. Borghei, H. Orelma, P. Mertens, and O. Rojas, *Immobilized cellulose nanospheres in lateral flow immunoassay enable rapid nucleocapsid antigen-based diagnosis of SARS-CoV-2 from salivary samples*. 2021.
- [52] A. Bashir, T. I. Awan, A. Tehseen, M. B. Tahir, and M. Ijaz, "Chapter 3 - Interfaces and surfaces," in *Chemistry of Nanomaterials*, T. I. Awan, A. Bashir, and A. Tehseen Eds.: Elsevier, 2020, pp. 51-87.
- [53] S. Pramanik, B. Pinguan-Murphy, and N. A. Abu Osman, "Developments of Immobilized Surface Modified Piezoelectric Crystal Biosensors for Advanced Applications," *Materials and Design*, vol. 40, pp. 304-313, 11/30 2012.
- [54] C. Yang and C. P. Fritzen, "Piezoelectric paint: characterization for further applications," *Smart Materials and Structures*, vol. 21, no. 4, p. 045017, 2012/03/28 2012, doi: 10.1088/0964-1726/21/4/045017.
- [55] S. Egusa and N. Iwasawa, "Application of Piezoelectric Paints to Damage Detection in Structural Materials," *Journal of Reinforced Plastics and Composites*, vol. 15, no. 8, pp. 806-817, 1996/08/01 1996, doi: 10.1177/073168449601500804.

- [56] E. Fatuzzo and W. J. Merz, "Switching Mechanism in Triglycine Sulfate and Other Ferroelectrics," *Physical Review*, vol. 116, no. 1, pp. 61-68, 10/01/ 1959, doi: 10.1103/PhysRev.116.61.
- [57] L.-H. Kang, "Vibration and impact monitoring of a composite-wing model using piezoelectric paint," *Advanced Composite Materials*, vol. 23, no. 1, pp. 73-84, 2014/01/02 2014, doi: 10.1080/09243046.2013.862390.
- [58] X. Li and Y. Zhang, "Analytical study of piezoelectric paint sensor for acoustic emission-based fracture monitoring," *Fatigue & Fracture of Engineering Materials & Structures*, <https://doi.org/10.1111/j.1460-2695.2008.01249.x> vol. 31, no. 8, pp. 684-694, 2008/08/01 2008, doi: <https://doi.org/10.1111/j.1460-2695.2008.01249.x>.
- [59] L. W. Schmerr, A. Lopez-Sanchez, and R. Huang, "Complete ultrasonic transducer characterization and its use for models and measurements," (in eng), *Ultrasonics*, vol. 44 Suppl 1, pp. e753-7, Dec 22 2006, doi: 10.1016/j.ultras.2006.05.088.
- [60] P. Davari, N. Ghasemi, and F. Zare, *Power converters design and analysis for high power piezoelectric ultrasonic transducers*. 2014.
- [61] J. F. Li, *Lead-Free Piezoelectric Materials*. Wiley, 2021.
- [62] N. Izyumskaya, Y. Alivov, S.-J. Cho, H. Morkoç, H. Lee, and Y. S. Kang, "Processing, Structure, Properties, and Applications of PZT Thin Films," *Critical Reviews in Solid State and Materials Sciences - CRIT REV SOLID STATE MAT SCI*, vol. 32, pp. 111-202, 07/01 2007, doi: 10.1080/10408430701707347.
- [63] C. B. Sawyer and C. H. Tower, "Rochelle Salt as a Dielectric," *Physical Review*, vol. 35, no. 3, pp. 269-273, 02/01/ 1930, doi: 10.1103/PhysRev.35.269.
- [64] D. Kireev, "COMBINING GRAPHENE AND ORGANIC FERROELECTRIC FOR POSSIBLE MEMORY DEVICES Thesis for the Degree of Erasmus Mundus Master of Nanoscience and Nanotechnology Chalmers University of Technology & KULeuven," 2013.
- [65] D. Damjanovic, "Hysteresis in Piezoelectric and Ferroelectric Materials," vol. 3, 2006, pp. 337-465.
- [66] J. Fialka, "Determination of the piezoelectric charge constant D33 measured by the laser interferometer and frequency method," (in English), *Annals of DAAAM & Proceedings*, Report p. 1253+, 2010 Annual
- // 2010. [Online]. Available: <https://link.gale.com/apps/doc/A246014192/AONE?u=gainstoftech&sid=googleScholar&xid=e1d95d4a>.

- [67] s. J. Priya *et al.*, "A Review on Piezoelectric Energy Harvesting: Materials, Methods, and Circuits," *Energy Harvesting and Systems*, vol. 4, 02/01 2017, doi: 10.1515/ehs-2016-0028.
- [68] M. Stewart, W. Battrick, and M. Cain, "Measuring Piezoelectric d33 coefficients using the Direct Method," *NPL Good Practice Guide*, pp. 1-34, 08/01 2001.
- [69] L. He, F. Xiujuan, T. Koukoulas, N. Feng, and Z. Bo, *Comparison between methods for the measurement of the D33 constant of piezoelectric materials*. 2018.
- [70] Q. Guo, G. Z. Cao, and I. Y. Shen, "Measurements of Piezoelectric Coefficient d33 of Lead Zirconate Titanate Thin Films Using a Mini Force Hammer," *Journal of Vibration and Acoustics*, vol. 135, no. 1, 2013, doi: 10.1115/1.4006881.
- [71] M. Cain, *Characterisation of Ferroelectric Bulk Materials and Thin Films*. 2014.
- [72] W. Jiang *et al.*, "In Situ Synchrotron XRD Characterization of Piezoelectric Al_{1-x}Sc_xN Thin Films for MEMS Applications," *Materials*, vol. 16, no. 5, p. 1781, 2023. [Online]. Available: <https://www.mdpi.com/1996-1944/16/5/1781>.
- [73] A. Khorsand Zak, A. M. W.H, and M. Darroudi, "Synthesis and characterization of sot-gel derived single-phase PZT nanoparticles in aqueous polyol solution," *Journal of Optoelectronics and Advanced Materials*, vol. 12, pp. 1714-1719, 08/01 2010.
- [74] G. Kim, M.-K. Seo, N. Choi, K. S. Baek, and K.-B. Kim, "Application of KLM Model for an Ultrasonic Through-Transmission Method," *International Journal of Precision Engineering and Manufacturing*, vol. 20, no. 3, pp. 383-393, 2019/03/01 2019, doi: 10.1007/s12541-019-00050-y.
- [75] I. Payo and J. M. Hale, "Sensitivity analysis of piezoelectric paint sensors made up of PZT ceramic powder and water-based acrylic polymer," *Sensors and Actuators A: Physical*, vol. 168, no. 1, pp. 77-89, 2011/07/01/ 2011, doi: <https://doi.org/10.1016/j.sna.2011.04.008>.
- [76] B. Charlot, D. Coudouel, P. Combette, and A. Giani, "Pyroelectric PZT sensors screen printed on glass," in *2013 Symposium on Design, Test, Integration and Packaging of MEMS/MOEMS (DTIP)*, 16-18 April 2013 2013, pp. 1-5.
- [77] Y. S. Yaras *et al.*, "Real-time device tracking under MRI using an acousto-optic active marker," *Magnetic Resonance in Medicine*, vol. 85, no. 5, pp. 2904-2914, 2021, doi: <https://doi.org/10.1002/mrm.28625>.
- [78] Y. S. Yaras, D. K. Yildirim, O. Kocaturk, and F. L. Degertekin, "Sensitivity and phase response of FBG based acousto-optic sensors for real-time MRI applications," *OSA Continuum*, vol. 3, no. 3, pp. 447-458, 2020/03/15 2020, doi: 10.1364/OSAC.385969.

- [79] Y. S. Yaras, O. Kocaturk, and F. L. Degertekin, "FBG Based Electric Field Sensor for MRI Safety," in *Optical Sensors and Sensing Congress*, Washington, DC, 2020/06/22 2020: Optica Publishing Group, in OSA Technical Digest, p. STu4D.7, doi: 10.1364/SENSORS.2020.STu4D.7. [Online]. Available: <https://opg.optica.org/abstract.cfm?URI=Sensors-2020-STu4D.7>
- [80] Y. S. Yaras and F. L. Degertekin, "Acousto-optic Modulator Based Magnetic Field Sensor Using π -Phase Shifted Fiber Bragg Grating," in *Optical Fiber Sensors Conference 2020 Special Edition*, Washington, DC, G. W. A. D. M. Cranch and P. Dragic, Eds., 2020/06/08 2020: Optica Publishing Group, in OSA Technical Digest, p. W4.34, doi: 10.1364/OFS.2020.W4.34. [Online]. Available: <https://opg.optica.org/abstract.cfm?URI=OFS-2020-W4.34>
- [81] Y. Yaras *et al.*, "Acousto-Optic Catheter Tracking Sensor for Interventional MRI Procedures," *IEEE Transactions on Biomedical Engineering*, vol. PP, pp. 1-1, 09/05 2018, doi: 10.1109/TBME.2018.2868830.
- [82] L. W. Bradley, Y. S. Yaras, and F. L. Degertekin, "Acousto-Optic Electric Field Sensor Based on Thick-Film Piezoelectric Transducer Coated Fiber Bragg Grating," in *27th International Conference on Optical Fiber Sensors*, Alexandria, Virginia, 2022/08/29 2022: Optica Publishing Group, in Technical Digest Series, p. F1.2, doi: 10.1364/OFS.2022.F1.2. [Online]. Available: <https://opg.optica.org/abstract.cfm?URI=OFS-2022-F1.2>